


Summer 2014

Numerical Study of Poration and Ionic Conduction in Nanopores Caused by High-Intensity, Nanosecond Pulses in Cell

Hao Qiu
Old Dominion University

Follow this and additional works at: https://digitalcommons.odu.edu/ece_etds

 Part of the [Biomedical Engineering and Bioengineering Commons](#), and the [Electrical and Computer Engineering Commons](#)

Recommended Citation

Qiu, Hao. "Numerical Study of Poration and Ionic Conduction in Nanopores Caused by High-Intensity, Nanosecond Pulses in Cell" (2014). Doctor of Philosophy (PhD), dissertation, Electrical/Computer Engineering, Old Dominion University, DOI: 10.25777/y7jm-my45
https://digitalcommons.odu.edu/ece_etds/115

This Dissertation is brought to you for free and open access by the Electrical & Computer Engineering at ODU Digital Commons. It has been accepted for inclusion in Electrical & Computer Engineering Theses & Dissertations by an authorized administrator of ODU Digital Commons. For more information, please contact digitalcommons@odu.edu.

**NUMERICAL STUDY OF PORATION AND IONIC CONDUCTION IN
NANOPORES CAUSED BY HIGH-INTENSITY, NANOSECOND PULSES IN
CELL**

by

Hao Qiu
B.S. Northwest University, China

A Dissertation Submitted to the Faculty of
Old Dominion University in Partial Fulfillment of the
Requirements for the Degree of

DOCTOR OF PHILOSOPHY

ELECTRICAL AND COMPUTER ENGINEERING

OLD DOMINION UNIVERSITY

August 2014

Approved by:

Ravindra P. Joshi (Director)

Linda L. Vahala (Member)

Frederic D. McKenzie (Member)

Shu Xiao (Member)

ABSTRACT

NUMERICAL STUDY OF PORATION AND IONIC CONDUCTION IN NANOPORES CAUSED BY HIGH-INTENSITY, NANOSECOND PULSES IN CELL

Hao Qiu
Old Dominion University, 2014
Director: Dr. Ravindra P. Joshi

This dissertation focuses on the dynamics and bioeffects of electroporation of biological cell and ionic conduction in nanopores under high-intensity, nanosecond pulses. The electroporation model utilized the current continuity equation and the asymptotic Smoluchowski equation to explore the transmembrane potential and pore density of the plasma and intracellular membranes; the ionic conduction model employed the Poisson-Nernst-Planck equations and the Navier-Stokes equations to analyze the ionic current and ion concentration profile.

Nanosecond electric pulses of high-intensity amplitude can initiate electroporation of intracellular organelles. The pulse parameters and cell electrical properties, that can selectively electroporate liposomes but keep the plasma and nuclear membranes intact, have been evaluated and optimized. This opens up the possibility of loading cell liposomes with potent drugs for subsequent release as part of a procedure for electrochemotherapy.

The traditional spherical model ignores the geometric influence; therefore, the more realistic irregular shape of intracellular organelles is considered to explore the geometric impact on dynamics of electroporation. The results obtained here show that in the shorter pulse range, geometric dependence is very pronounced, and so short pulses could be very effective in highly irregularly shaped cells.

In addition, nanopore transport is analyzed using a numerical method that couples the Nernst-Planck equations for ionic concentrations, the Poisson equation for the electric potential and Navier-Stokes equations for the fluid flow. Roles of the applied bias, the geometric asymmetry in the nanopore, as well as the charge distribution lining the membrane are comprehensively examined. The results show non-linear I - V characteristics that are in reasonable agreement with data, and suggest a bias-dependent expansion of an asymmetric pore, possibly arising from the enhanced flux of incident ions on the membrane walls.

ACKNOWLEDGEMENTS

I would like to express my great gratitude to my advisor, Prof. Ravindra P. Joshi, for his valuable academic guidance and encouragement throughout my entire PhD study.

I also want to cordially thank my committee members, Prof. Linda L. Vahala, Prof. Rick Mckenzie, and Prof. Shu Xiao for reviewing my dissertation and providing helpful comments and suggestions. I would also like to acknowledge ECE Department of Old Dominion University for their support.

I would like to thank my supportive parents and sister for their continuous encouragement.

Finally, I would also like to thank all my dear friends at Old Dominion University all these years.

TABLE OF CONTENTS

	Page
LIST OF TABLES	viii
LIST OF FIGURES	ix
1. INTRODUCTION	1
1.1 Overview	1
1.2 Objective and Scope of this Research.....	3
2. LITERATURE REVIEW AND BACKGROUND	6
2.1 Overview of Electroporation.....	6
2.1.1 Case for Ultrashort Pulse Application	7
2.1.2 Electrical Effects on Subcellular Structures	10
2.1.3 Biomedical Applications	13
2.2 Modeling Scheme--Distributed Electrical Model	14
3. MODELING AND SIMULATION DETAILS	18
3.1 Electroporation Model	18
3.2 PNP-NS Model	27
3.2.1 PNP-NS Equations	27
3.2.2 Dimensionless Form of PNP-NS Model	29
3.2.3 Simulation Analysis Method	30
4. SIMULATION RESULTS AND DISCUSSION	35
4.1 Simulation Results of Electroporation Model.....	35
4.1.1 Model Verification	35
4.1.2 Simulation Results.....	39
4.2 Simulation Results of PNP-NS Model.....	69
4.2.1 Model Verification	69
4.2.2 Simulation Results.....	74
5. CONCLUSIONS AND FUTURE RESEARCH	86
5.1 Research Summary	86
5.2 Future Work	88
REFERENCES	90
APPENDICES	95
APPENDIX I	95
APPENDIX II.....	97

APPENDIX III.....99
APPENDIX IV.....102

LIST OF TABLES

Table	Page
1. Parameters used in the electroporation model.	23
2. Parameters used in the transport simulations.....	31
3. Boundary conditions used in the simulations	33
4. Parameters used in the PNP model verification.....	70
5. Parameters used in the PNP-NS model verification.	73
6. Various values of the radii R_l and R_r chosen for I - V simulations.	77
7. Values of left pore radius adjusted as a function of the magnitude of applied bias. ...	83

LIST OF FIGURES

Figure	Page
1. Pore development.....	7
2. Charge distribution in cell membranes	9
3. Caspase activation in intact HL-60 cells by ultrashort, high-intensity pulse.....	12
4. Schematic of one quarter of distributed model of a cell.	15
5. The 2D axisymmetric model used.	22
6. Schematic of a nanopore.	34
7. TMP comparison between numerical and analytical methods (stationary)	37
8. TMP comparison between numerical and analytical methods (time-dependent).	38
9. Time course of transmembrane potential on plasma membrane.	41
10. Time course of pore density on plasma membrane at different TMP values.	44
11. TMP and pore density number of membranes in cell.	48
12. Amplitudes required to electroporate plasma membrane and liposome membranes with two different radii.	53
13. Optimized TMPs and pore density number of membranes in cell.....	55
14. Two assumed rectangular pulses and corresponding Fourier spectra.....	57
15. Simulation results obtained showing the TMP distribution over plasma membrane, OMM and IMM.	61
16. Geometry of the IMM and OMM chosen.	62
17. Simulation results obtained showing the pore density number over plasma membrane, OMM and IMM.	64
18. Predictions of the IMM pore density distribution with 150ns rise time.	65
19. Predictions of pore density profile of plasma membrane, OMM and IMM for the 60ns pulse.	68
20. Distribution of electric potential and ionic concentration.....	72
21. Electroosmotic flow velocity in a cylindrical nanotube.	74
22. Distribution of dimensionless concentration of cation and anion near the tip of the conical nanopore.	76
23. Simulation results showing the current-voltage characteristics for different aspect ratios R through a 5 nm uncharged nanopore.	82

24. Simulation results showing the current-voltage characteristics for different surface charge densities	84
25. Results for the I - V response for a nonuniform pore surface charge distribution lining the pore walls.	84
26. Voltage dependent values of the left pore radius R_l extracted from comparisons with experimental data.	85
27. Hypothetical sketch of a conical nanopore.	85
28. Reuse License for Figure 1	102
29. Reuse License for Figure 3	103
30. Reuse License for Figure 4	104

CHAPTER 1

INTRODUCTION

1.1 Overview

The study of bioelectric mechanisms inherent in cells for potential benefits in the field of medicine, therapy, and diagnostics have been of interest over the past few decades. Particularly, the effect of intense pulsed electric fields on biological cells and tissues has been the hot topic of research since the late 1950's, with the first report of electric-field assisted reversible breakdown of cell membranes by R. Staempfli [1].

The bio-effects of electrical pulsing to cells can be beneficial, as with controlled medical therapy but can also be detrimental, as with uncontrolled electric shock. Hence, it is important to understand and unravel the dynamics of electrical pulsing and get a good perspective of the physics mechanisms. Looking into these aspects by means of suitable electric models, therefore, is the driving interest to this work.

Electroporation involves rapid structural rearrangement of the membrane [1-3], leading to the rapid increase of electrical conductivity [4]. It is hypothesized that the increased membrane electrical conductivity is associated with the formation of pores in the lipid bilayer. In "classical" electroporation, rectangular pulses of *micro- or millisecond duration* with rise times in the order of microseconds are typically used. Since the charging time of a cell is typically much shorter than these classical pulse durations (for a cell with radius of $\sim 10 \mu\text{m}$, the charging time in a physiological medium is roughly 100 ns), the electroporation pulses primarily affect the plasma membrane while the cell interior practically remains shielded from the external electric field.

However, if the cells are exposed to pulses with durations in the nanosecond range (and amplitudes over tens of kV/cm), the electric fields can also affect membranes of the interior cell organelles [5, 6]. The relatively recent development of electrical pulses with intense electric fields (~ 100 kV/cm) and ultrashort durations (~ 10 nanoseconds) opens up the possibility of creating nanopores in biological membranes efficiently. The opening of such channels enables the transport of ions and water-soluble species. Electroporation can, therefore, be used to initiate molecular fluxes for the purposes of introducing genetic material into cells, along with numerous other applications [7-11]. Ion transport is also of significant interest, since cell membranes strive to maintain the ionic electrochemical gradient, which is important for a variety of activities, such as the transport of nutrients and generation of electrical signals.

High-intensity, nanosecond pulse electroporation has been a very recent development in the field of bioelectrics. Besides membrane electroporation [12-15], the high-intensity, short-duration electrical pulses have been shown to promote electrically-triggered intracellular calcium release [16-18], the destruction of micro-organisms [12, 19, 20], killing of tumor cells [12, 21], bring about DNA damage [22], and possibly aid in wound healing [23]. Typical pore diameters upon electroporation have been predicted to be on the order of 1.6 nm with about a 0.6 nm statistical spread [13, 14, 24-28], and are roughly verified by tracking transport of fluorescent dyes through cell membranes [12].

Moreover, there are several advantages of using ultra-short electric pulses including: (i) the capability of penetration into intracellular organelles membranes; (ii) the possibility of pore manipulation by adjustment of pulse amplitude and pulse duration; (iii) negligible thermal heating and low energy input.

1.2 Objective and Scope of this Research

Electroporation would occur on both the plasma membrane and membranes of intracellular organelles when high-intensity, ultrashort electric pulses are applied. The transmembrane potential and pore density number are coupled and calculated as a time-dependent process on macroscopic level by means of the Smoluchowski equation. The actual numerical implementation is based on using COMSOL 4.3b (a commercial software) under the specified pulsed electric field parameters in order for analysis of bio-effects of electroporation.

The Smoluchowski equation expresses the distribution of pores as a function of their radius and time. The formation of pores leads to a rapid increase in permeability of cell membrane structures; hence, the ionic current increases due to the creation of an aqueous pathway within the membrane. This, in turn, results in decreases in the transmembrane potential (which is the driving force behind electroporation) and subsequently reduces the rate and number of pore formation. Ultimately the pores reseal, if the electroporation is not irreversible. Different membrane structures have different charging times. So the adjustment of pulsed electric field parameters (e.g., the amplitude, pulse duration, and pulse number) could be used to selectively electroporate and electromanipulate intracellular organelles. Therefore, a model that includes the Smoluchowski equation could be used to probe electroporation of membrane structures (not only for plasma membranes, but also for intracellular organelles), invoked by a pulsed electric field. The bio-effects, including drug release, mitochondrial effects, etc. caused by high-intensity, nanocond electric field could thus be analyzed and predicted quantitatively.

The goal is to gauge and investigate through numerical simulations if changes in the electrical pulse parameters can provide a method for selective and controlled poration of cells and liposomes. If possible, this technique could be used for drug release from embedded liposomes, or the selective release of intra-cellular calcium, or the deliberate damage to cellular mitochondria for destruction of malignant cells.

Since ultrashort, high-intensity electric pulses open pores in biological cell membranes, studies of ion transport in synthetic nanopores provide an easier and more controlled alternative for probing the actual physiological processes in living organisms [29]. An interesting observation of transport through such synthetic nanopores has been ion current rectification (ICR), which yields an asymmetric diode-like current-voltage (I-V) behavior [30-35]. It is generally accepted that such an ion current rectification occurs in charged pores with broken symmetry. The opening of membrane nanopores and the subsequent transport of ions has been observed and studied through patch-clamp experiments [36-38]. Interestingly, the ionic transport has shown asymmetric characteristics, similar to those observed in synthetic membranes. Hence, quite intuitively one expects similar transport physics and inherent mechanisms such as asymmetric pore shapes and membrane charge distributions to be at work in biological nanopores as well. Shape asymmetry in bio-membrane pores has already been predicted based on energy minimization arguments [39].

Chapter 2 of this thesis provides a literature review of relevant research and reported contributions in the field of electroporation and ion conduction in nanopore. Chapter 3 gives a detailed description of such simulation models as the self-consistent model for pore density number and transmembrane potential and also the continuum model of ion

transport in nanopore. Details of the various simulation results obtained and related discussions are dealt with in Chapter 4. Finally, a summary and conclusions are given in Chapter 5, as well as comments on possible future research work.

CHAPTER 2

LITERATURE REVIEW AND BACKGROUND

2.1 Overview of Electroporation

When a cell is exposed to a sufficiently high electric field, its membrane becomes permeable to molecules and ions that otherwise cannot pass through it. This permeabilization is manifested as a rapid increase in membrane conductivity by 5-6 orders of magnitude [40]. This process, which is an important effect on biological cells due to electric fields, subsequently termed electroporation, can be reversible (in which treated cells survive); or can be irreversible for large electric fields and/or pulse duration, leading to cell death by membrane rupture. When the electric field is not too strong and/or the exposure is not very long, the pores reseal (within seconds to minutes) after exposure and the cells can restore their normal activity.

Once electroporation occurs, pores are created in the lipid bilayer of cell membrane, which provides aqueous pathways through which biologically active substances could be introduced into cells, either through diffusion (such as small molecules) or through electrophoretically driven processes (e.g. DNA transfer). Although the details of pore formation and subsequent development are still not fully understood, theory, simulation and experiments validate the qualitative properties of pore formation, enlargement and resealing. Figure 1 shows the development of pore formation, the transition from a hydrophobic pore to a hydrophilic one due to membrane rearrangement, and pore expansion. Also, it is generally accepted that one of the essential factors for the occurrence of electroporation is the induced transmembrane voltage. This voltage superimposes onto the resting membrane potential, and is responsible for producing

differences between the electric properties of membrane and the external medium. Electroporation would occur only if the induced transmembrane voltage is large enough to reach a threshold value, which has been reported to lie in the range of 200-1000 mV, depending on the cell type [41].

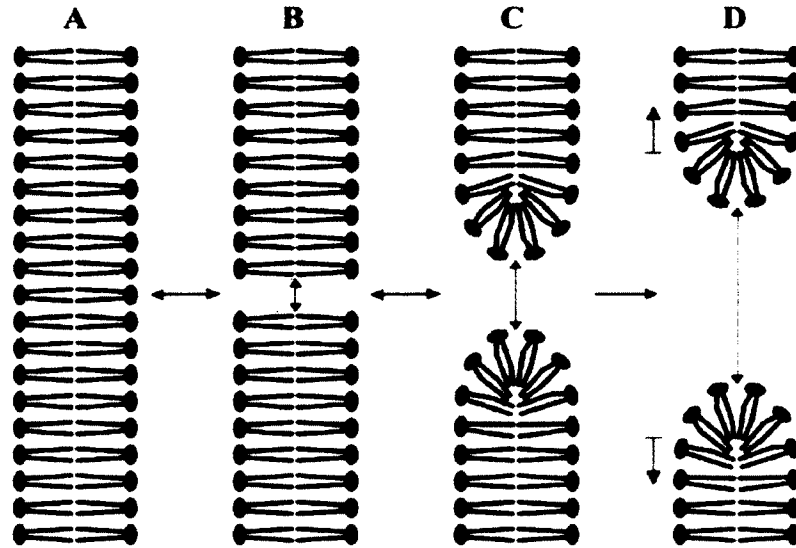


Figure 1. Pore development. (A) Bilayer without pores, (B) Bilayer with a hydrophobic pore, (C) reversible transition into a metastable hydrophilic pore, (D) irreversible transition into an unstable self-expanding hydrophilic pores.[42]

Copyright, © 2012, IEEE

2.1.1 Case for Ultrashort Pulse Application

More recently, the pulse duration range has been extended to the nanosecond regime. Such ultrashort pulsing has been used to electromanipulate the interior components of cells. The pulses on nanosecond scale can permeabilize intracellular granules [43], the nuclear membrane [44], the inner mitochondrial membrane [45], and also stimulate the release of calcium from endoplasmic reticulum [16, 46, 47]. Ultrashort pulses need to have an ultrashort rise time and fall time, which has been achieved through pulse-power technology nowadays. Figure 2 shows the charge distribution for the membrane structure

of cells. As is shown in Figure 2b, if a DC electric field or an electric pulse with a long duration as compared to the charging time of outer membrane is applied to the cell, only the outer membrane will be charged. Under this condition, the plasma membrane acts as an ideally insulating capacitive membrane. This results in almost no electric field being exerted on the subcellular component and complete shielding of the cell interior. However, when the rise time and duration of a pulsed electric field is short enough, then electric field build-up on the subcellular membrane is expected within the charging time of the plasma membrane. Based on this theory, if the electric field is of high-amplitude with ultrashort duration, the effects of such short pulses have been shown to reach into the cell's interior [43] and drive bio-effects. Thus, ultrashort pulsed electric fields could produce pronounced effects on intracellular organelles such as the endoplasmic reticulum (which are stores of calcium) or the mitochondria (which functions as the power plant in cells).

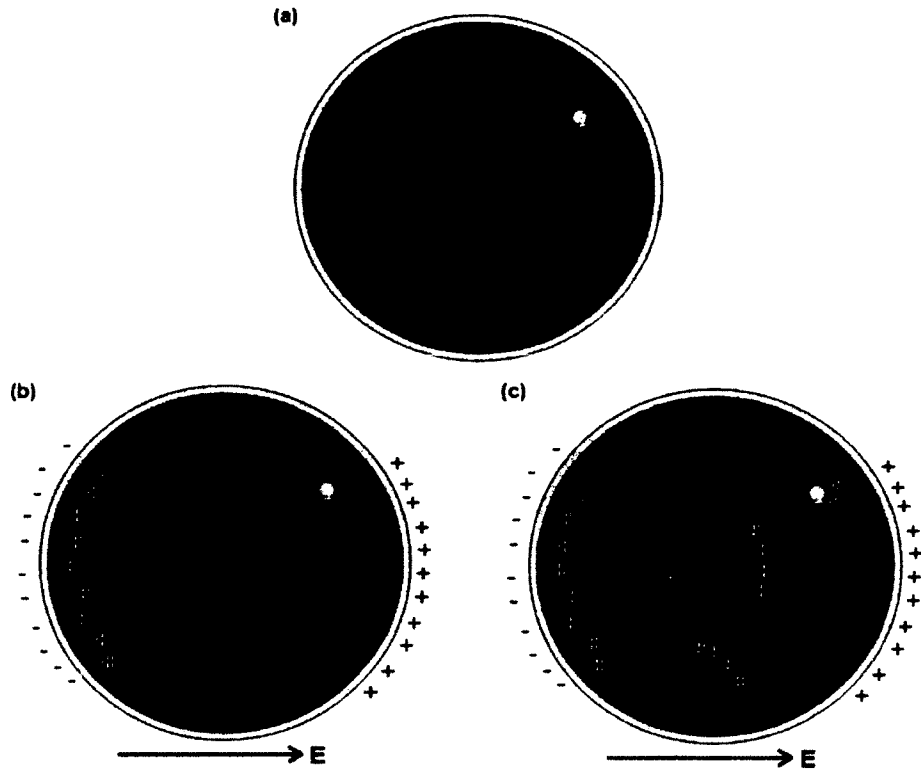


Figure 2. Charge distribution in cell membranes. (a). Structure of a biological cell (including some organelles, e.g. mitochondria, liposome) (b). Charge distribution for a slowly rising (compared to membrane charging time constant or dielectric relaxation time) electric field (c). Charge distribution for a rapid rising (compared to membrane charging time constant or dielectric relaxation time) electric field.

Electric field pulses exceeding 1MV/m with nanoseconds to hundreds of nanoseconds durations have been shown to permeabilize intracellular organelles [48] and release Ca^{2+} from the endoplasmic reticulum (ER) [49]. Moreover, the biological effects depends on the electric field amplitude, pulse duration and pulse number. The bioelectric effects could be evaluated using the similarity or scaling law [50] for multiple pulsing scenarios. Similarly, pulses with a different set of electrical parameters have been shown to damage the cell nucleus [51], as observed through Comet assays which are indicative of DNA damage within cell nuclei. So in theory, it appears possible to alter the electrical

parameters and judiciously choose the setting to selectively affect the plasma membrane, the ER, the mitochondria, or the cell nucleus individually, or in sub-groups.

2.1.2 Electrical Effects on Subcellular Structures

High-intensity, nanosecond pulses could get access to subcellular structures mainly due to displacement currents or (to a much smaller and indirect extent) conduction currents flowing through pores that could cause long-term ionic imbalances. Also, experiments have confirmed that it is possible to selectively change the function or survival of cells with sufficiently high electric field of short duration within the range of several nanoseconds. Various parameter combinations of pulse amplitude, duration and pulse numbers have been applied to cells with different electrical and physiological parameters in order to affect intracellular structures, with the observed results being in line with expectation.

Observations of pulsed electric field effects on the endoplasmic reticulum (ER) and the mitochondria are broadly under study due to their essential functions of these organelles in cells. ER is an intracellular store of calcium, and the mitochondrion is the cellular power plant responsible for ATP production and maintaining a transmembrane proton gradient to drive a variety of tasks [52]. Calcium is known as a second messenger molecule that regulates a series of responses in cell signaling, including enzyme activation, gene transcription, neurotransmitter release, secretion, muscle contraction, and apoptosis. Calcium release from mitochondria is considered as an initiation to apoptosis [53]. Thus control and regulation of calcium, or lack thereof, strongly affect cell survival.

Apoptosis can be observed when the amplitude of pulsed electric field exceeds a critical value; during this process several signaling pathways are activated to initiate cell death. The ability of the short, high-intensity pulses to bring about intracellular damage and apoptotic behavior is not fully understood. Evidences that apoptosis is controlled and regulated by mitochondria in cell have been reported [54-58]. This suggests that mitochondria could possibly become the focus of the study of cell death and irreversibility caused by the application of ultrashort electric pulses.

Also, the potential to induce apoptosis in cells and tumors exposed to a nanosecond pulsed electric field suggests the possibility of cancer therapy by pulsed electric field with nanosecond durations. Experiments show that apoptosis can be observed under a pulsed electric field with higher than 200 kV/cm of 10 ns pulses, or a lower amplitude for longer pulses or pulse trains [59].

In experiments, caspase activation is usually employed as an apoptosis marker. In Figure 3 [17], cells were exposed to a pulsed electric field of 40 kV/cm with 60 ns or 300 ns in the presence of ethidium homodimer-1, which determines the integrity of the plasma membrane. In one experiment, a cell permeable fluorescent irreversible inhibitor of active caspases FITC-VAD-FMK was incubated with the cells for 20 minutes after the pulses. The cells were then analyzed by flow cytometry and use of the Cell Quest software for data processing. The level of fluorescence is a direct indicator of levels of the electrical effects on plasma membrane integrity and degree of electroporation. Figure 3 shows that effects on plasma membrane integrity were less for shorter pulses and the response of caspase activation was more robust for longer pulses at the given electric field [17].

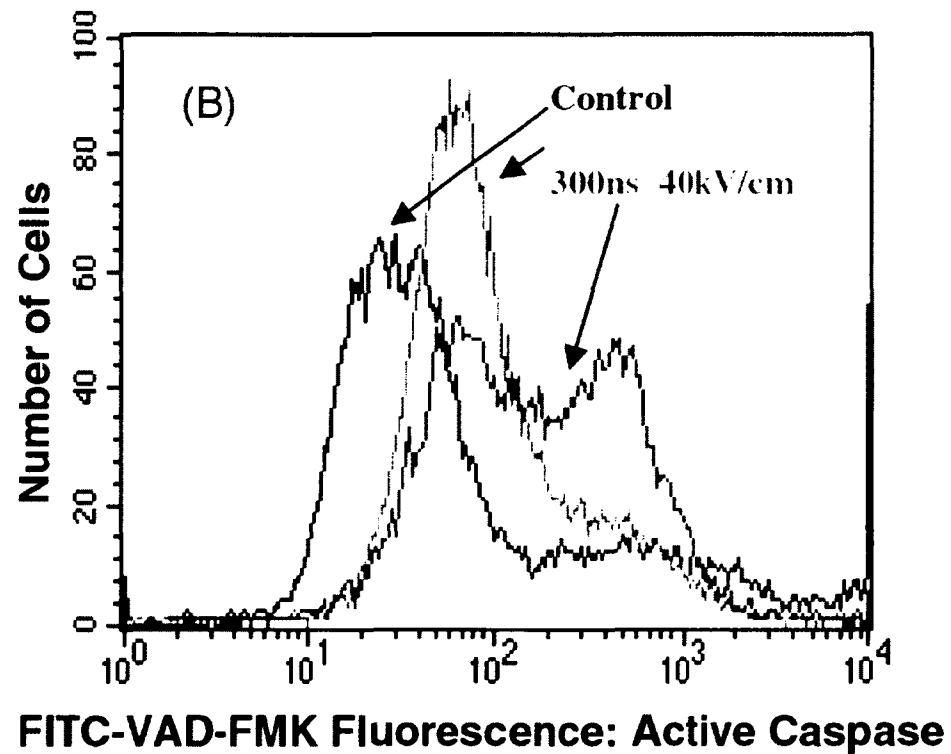
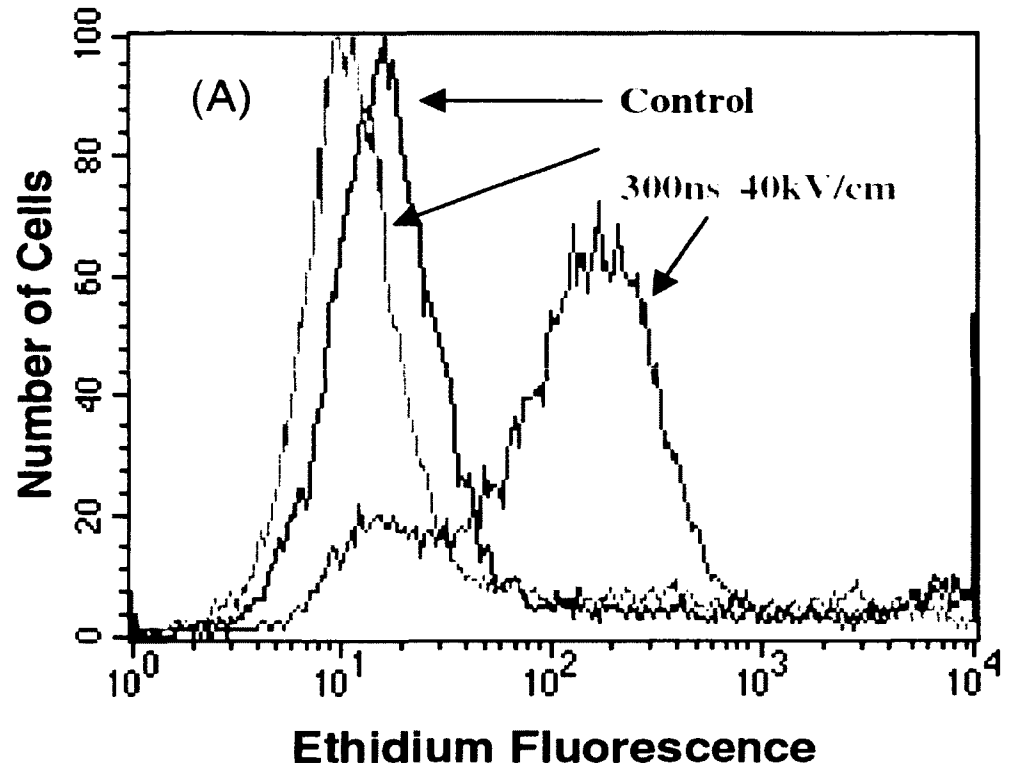


Figure 3. Caspase activation in intact HL-60 cells by ultrashort, high-intensity pulse. [17]
© IOP Publishing. Reproduced with permission. All rights reserved.

It was hypothesized by Weaver et al. [60] that high-amplitude, nanosecond pulses may induce high transmembrane potential at mitochondrial sites, which leads to apoptosis owing to the opening of the mitochondrial permeability transition pore complex (MPTP).

However, all of these interesting biological effects depend critically on the intensity of transmembrane potentials (TMPs) induced on organelle membranes due to the electric pulse drivers. Hence, it becomes important and critical to predict these TMPs and electric fields at the site of various organelles in response to a chosen set of voltage pulsing parameters. For realistic predictions and calculations, all of this has to be worked out for the actual cell or organelle shapes.

2.1.3 Biomedical Applications

Nanosecond pulses with high amplitude have been used in a wide range of biomedical applications, including wound healing, cancer treatment, electrochemotherapy, drug delivery, and nerve stimulation.

As mentioned before, nanosecond pulses could get access into intracellular structures. For a given set of electrical parameters, different organelle membranes may likely behave differently. Some structures may be irreversibly electroporated and then cause death or dysfunction, while other may have the ability to reverse to normal condition after the pulse. Ideally, in the treatment of cancer cells, cancer cells would shrink and then disappear after several treatments, while normal cells should survive during the whole treatment.

Drug release could be achieved by electroporating cells that might have been loaded with drugs. Liposome is composed of lipid molecules which form a spherical membrane,

and could be used to encapsulate and deliver drugs or genes into cells. By deliberately adjusting the size and dielectric properties of liposomes, they could be selectively electroporated once inside the cell without disrupting the plasma membrane or other intracellular structures. Similarly, ER and mitochondria could selectively be electroporated in order to release calcium or for other biomedical purposes. Furthermore, ultrafast pulses applied to cells could avoid Joule heating in such short duration. Thus, there is a slew of selective treatment and organelle response behavior (especially for irregular shapes) that has not been studied. The possibilities for tailoring electric pulses and targeting specific organelles or liposomes have not been probed. Here, as part of a dissertation research, analyses of these aspects are being proposed for a detailed study.

2.2 Modeling Scheme—Distributed Electrical Model

A distributed electrical model is introduced for evaluation of transmembrane potential, which includes dynamic conductivities of cell membranes and substructures. The cell is broken up into finite segments which are represented as a series of parallel Resistor-Capacitor combinations to calculate the current flow and charging effects through a time-domain nodal analysis. In consideration of simplicity, azimuthal symmetry is assumed based on a spherical coordinate system. A quarter of the entire computation region including the cell, its substructure and its surrounding suspension medium is discretized along the r and θ directions as shown in Figure 4 [61].

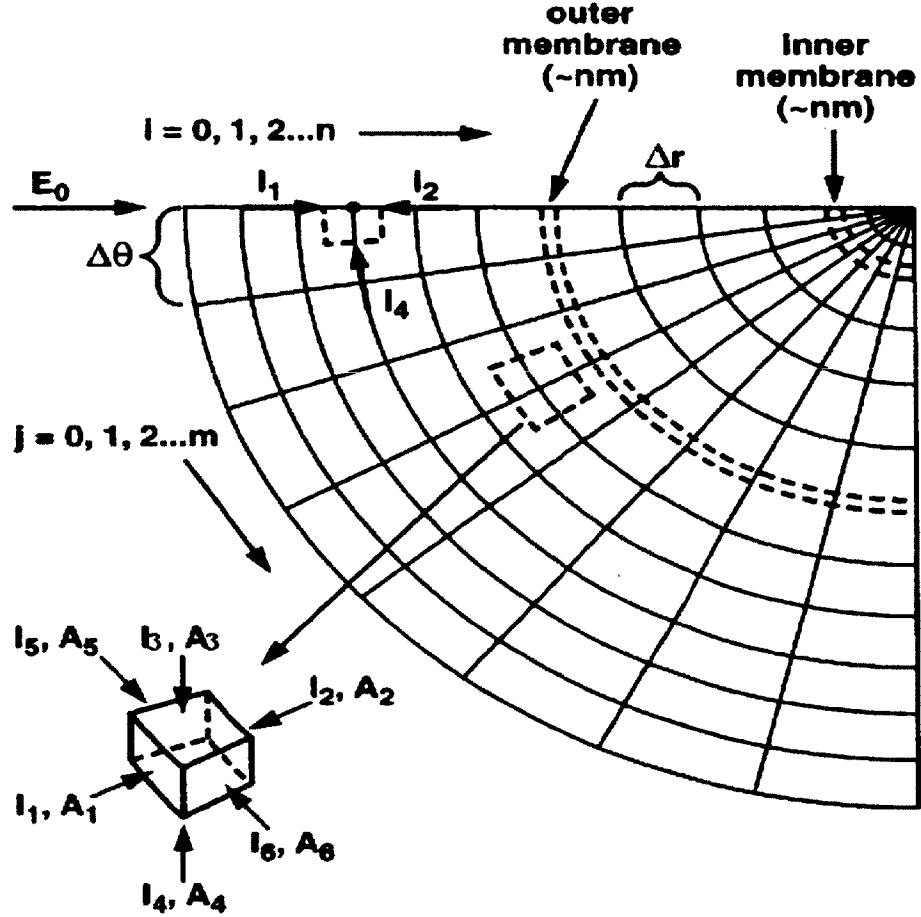


Figure 4. Schematic of one quarter of distributed model of a cell. The dotted box shows a typical element with current flows. [61] Copyright, © 2004, IEEE

The following current continuity equation should be satisfied for such analysis:

$$\nabla \cdot \left(J + \frac{\partial D}{\partial t} \right) = 0 \quad , \quad (2.1)$$

where J is the current density and D the electric displacement vector. Specifically, for each element, the current continuity equation can be rewritten in the following form:

$$\sum_{k=1}^6 \left(\sigma E + \varepsilon \frac{\partial E}{\partial t} \right) \times A_k = \sum_{k=1}^6 I_k = 0 \quad , \quad (2.2)$$

In each element, I_5 and I_6 are currents along the \emptyset direction. In consideration of equipotential due to geometric symmetry, $I_5 = I_6 = 0$. Therefore, the discretized equation in space and time holds:

$$\begin{aligned}
& \sigma_1 \frac{V_{i-1,j}^t - V_{i,j}^t}{\Delta r} A_1 + \sigma_2 \frac{V_{i+1,j}^t - V_{i,j}^t}{\Delta r} A_2 + \sigma_3 \frac{V_{i,j-1}^t - V_{i,j}^t}{r\Delta\theta} A_3 \\
& + \sigma_4 \frac{V_{i,j+1}^t - V_{i,j}^t}{r\Delta\theta} A_4 + \frac{\varepsilon_1}{\Delta t} \left[\frac{V_{i-1,j}^{t+1} - V_{i,j}^{t+1}}{\Delta r} - \frac{V_{i-1,j}^t - V_{i,j}^t}{\Delta r} \right] A_1 \\
& + \frac{\varepsilon_2}{\Delta t} \left[\frac{V_{i+1,j}^{t+1} - V_{i,j}^{t+1}}{\Delta r} - \frac{V_{i+1,j}^t - V_{i,j}^t}{\Delta r} \right] A_2 \\
& + \frac{\varepsilon_3}{\Delta t} \left[\frac{V_{i,j-1}^{t+1} - V_{i,j}^{t+1}}{r\Delta\theta} - \frac{V_{i,j-1}^t - V_{i,j}^t}{r\Delta\theta} \right] A_3 \\
& + \frac{\varepsilon_4}{\Delta t} \left[\frac{V_{i,j+1}^{t+1} - V_{i,j}^{t+1}}{r\Delta\theta} - \frac{V_{i,j+1}^t - V_{i,j}^t}{r\Delta\theta} \right] A_4 = 0, \tag{2.3}
\end{aligned}$$

where $V_{i,j}^t$ is the electric potential at node (i, j) at time t with $i = 0, 1, \dots, n$ and $j = 0, 1, \dots, m$. The radial distance between nodes (i, j) and (n, m) is r . The areas A_1 through A_4 are shown in Figure 4. Also, ε_1 through ε_4 , and σ_1 through σ_4 are the permittivities and conductivities, respectively, at faces 1 through 4. Thus, if a node were to be within the suspension medium, then all the σ values would be the same. However, for nodes on a membrane, σ_1 would be different from σ_2 .

After applying specific boundary condition, for $j = 0$ and $0 < i < n$, equation (2.3) becomes:

$$\begin{aligned}
& \sigma_1 \frac{V_{i-1,j}^t - V_{i,j}^t}{\Delta r} \left(\frac{r + \Delta r}{2} \right)^2 \left(\cos\theta - \cos\left(\frac{\theta + \Delta\theta}{2}\right) \right) \\
& + \sigma_2 \frac{V_{i+1,j}^t - V_{i,j}^t}{\Delta r} \left(\frac{r - \Delta r}{2} \right)^2 \left(\cos\theta - \cos\left(\frac{\theta + \Delta\theta}{2}\right) \right) \\
& + \sigma_4 \frac{V_{i,j+1}^t - V_{i,j}^t}{r\Delta\theta} r \nabla r \sin\left(\frac{\theta + \Delta\theta}{2}\right) \\
& + \frac{\varepsilon_1}{\Delta t} \left[\frac{V_{i-1,j}^{t+1} - V_{i,j}^{t+1}}{\Delta r} - \frac{V_{i-1,j}^t - V_{i,j}^t}{\Delta r} \right] \left(\frac{r + \Delta r}{2} \right)^2 \left(-1 - \cos\left(\frac{\theta + \Delta\theta}{2}\right) \right) \\
& + \frac{\varepsilon_2}{\Delta t} \left[\frac{V_{i+1,j}^{t+1} - V_{i,j}^{t+1}}{\Delta r} - \frac{V_{i+1,j}^t - V_{i,j}^t}{\Delta r} \right] \left(\frac{r - \Delta r}{2} \right)^2 \left(-1 - \cos\left(\frac{\theta + \Delta\theta}{2}\right) \right) \\
& + \frac{\varepsilon_4}{\Delta t} \left[\frac{V_{i,j+1}^{t+1} - V_{i,j}^{t+1}}{r\Delta\theta} - \frac{V_{i,j+1}^t - V_{i,j}^t}{r\Delta\theta} \right] r \Delta r \sin\left(\frac{\theta + \Delta\theta}{2}\right) \\
& = 0. \quad (2.4)
\end{aligned}$$

In equation (2.4), $\theta = \pi + j * \Delta\theta$, $\Delta\theta = (\pi/2)/m$. Considering the electric field applied in Figure 4, potential at node with $i = n$ is zero, i.e. $V_{n,j} = 0$. For nodes with index $i = 0$, their potential is calculated as $V_{0,j} = -E_0 R \cos\theta$, where E_0 is the applied electric field, R is the radius of computation region. For nodes with $j = 0$, their potentials are equal, i.e. $V_{i,m} = V_{n,j} = 0$.

Applying all the boundary conditions, N unknown node potentials can be obtained by N equations at each time step. Numerically, this can be done through a matrix solution of the form $Ax = B$ (where A is a coefficient matrix).

CHAPTER 3

MODELING AND SIMULATION DETAILS

3.1 Electroporation Model

Electroporation can be reversible, leading to pore resealing after a transient period of high conductivity, or irreversible, in which case the membrane ruptures without any resealing. The Smoluchowski equation, a partial differential equation (PDE), can be used to predict pore generation, growth, destruction and size evolution, which is helpful to understand the dynamic process. The driving force for changes in the pore distribution is the applied membrane voltage, though diffusive flow in the radial space also changes the pore sizes. As is generally assumed, pore formation is a two-step process: first, non-conducting pores are generated; then, the pores can either develop into conducting pores or be destroyed. This Smoluchowski equation shown below, governs the distribution of pores as a function of their radius and time:

$$\frac{\partial n}{\partial t} + D \frac{\partial \left(-\frac{\partial \varphi}{\partial r} \frac{n}{k_B T} - \frac{\partial n}{\partial r} \right)}{\partial r} = S(r), \quad (3.1)$$

where r is pore radius, $n(r, t)$ denotes the pore density distribution function, D is the diffusion constant of pores, $\varphi(r)$ is pore energy, k_B is Boltzmann constant, T is absolute temperature, and $S(r)$ is the source term that represents the creation and the destruction of pores, which can be written as given below[62]:

$$S(r) = v_c h \frac{\varphi_r}{k_B T} e^{\varphi/k_B T} - v_d n H(r_* - r). \quad (3.2)$$

where v_c is the attempt rate density, h is the membrane thickness, r_* is the minimum radius (0.5 nm) for the creation of conducting pores, and conducting pores only survive if

their radii remains larger than r_* ; destruction of a conducting pore occurs when it drifts or diffuses into a radius with value below r_* . φ is the pore energy when $r < r_*$. v_d is the frequency of lipid fluctuations, and $H(\cdot)$ denotes Heaviside function, representing the fact that only non-conducting pores are destroyed.

However, this PDE has a few drawbacks. For example, it does not have an analytical solution and must be solved numerically. The presence of disparate scales on temporal and spatial terms makes the numerical solution hard to obtain.

3.1.1 An Asymptotic Model

A rigorous, asymptotic reduction of the Smoluchowski equation to an ordinary differential equation (ODE) was proposed by Neu and Krassowska [62], which describes the dynamics of pore density shown as given below:

$$N(t) \equiv \int_0^{\infty} n(r,t) dr , \quad (3.3)$$

This proposed asymptotic ODE below well represents most of key features of electroporation:

$$\frac{dN}{dt} = \alpha e^{\left(\frac{TMP}{V_{ep}}\right)^2} \left(1 - \frac{N}{N_0} e^{-q\left(\frac{TMP}{V_{ep}}\right)^2} \right) . \quad (3.4)$$

where N_0 is the membrane pore when there is no transmembrane potential (TMP), V_{ep} is characteristic voltage of electroporation, q is electroporation constant. Thus, N depends on the TMP in a dynamic fashion.

3.1.2 Current density through pore

The current density J_{ep} due to the movement of ions through the pores could be expressed as[63]:

$$J_{ep} = N\pi r_p^2 \sigma_p \frac{TMP}{h} \frac{e^{P^*} - 1}{\frac{w_0 e^{w_0 - nP^*} - nP^*}{w_0 - nP^*} e^{P^*} - \frac{w_0 e^{w_0 + nP^*} + nP^*}{w_0 + nP^*}}, \quad (3.5)$$

where σ_p is the inner conductivity of the aqueous solution that fills a single pore, h is the thickness of the membrane, n is the relative entrance length of pore, P^* is the dimensionless form of TMP, i.e., $P^* \equiv \frac{TMP}{(RT/F)}$, F is Faraday's constant, R is the universal gas constant, and T is the temperature. The expression takes account of the pore shape and the interactions between the pore wall and ions that pass through the pore, in a simplified manner. Furthermore, in the above equation, membrane conductivity due to electroporation can be expressed as: $\sigma_{ep} = \frac{J_{ep}}{E_m}$, where $E_m = \frac{TMP}{h}$ is the membrane electric field. The total membrane conductivity is the sum of passive membrane conductivity and contributions from the electroporated part.

3.1.3 Transmembrane Potential of Membranes

Transmembrane potential (TMP) is an important factor that determines cell survival. Through the process of electroporation, TMP is a time dependent variable, which reflects the dynamic of pore development from the perspective of ionic voltage. Also, pore creation rate is strongly dependent on the transmembrane potential through the energy term in the Smoluchowski equation.

Generally, the electric potential V can be calculated from the total current-continuity equation:

$$\nabla \cdot \left(- \left(\sigma + \varepsilon \frac{\partial}{\partial t} \right) \nabla V \right) = 0 \quad , \quad (3.6)$$

where σ is the conductivity, and ε is the permittivity.

After calculation of electric potential V on both sides of membrane, TMP can be obtained as the difference in potentials.

3.1.4 Simulation Analysis Method

A finite element model of a cell suspended in medium containing the nucleus and intracellular organelles such as liposome and mitochondria can be constructed using the COMSOL Multiphysics 4.3b software tool [64]. Calculations have been performed with a 2D axisymmetric model, which considerably reduces the calculation time and has the capability to recover to realistic 3D model.

One representative two-dimensional (2D) axisymmetric geometry used for the simulations is shown in Figure 5 with dimensions in micrometers. The rectangular (brown) 50 μm x 100 μm region represents the extracellular medium, in which the big yellow semicircle of radius 10 μm represents the cell under investigation. The smaller gray semicircle (gray) of 3 μm in Figure 5 represents the nucleus, while half of the mitochondrion is shown in blue. The irregular mitochondrion geometry though not apparent in the left part of Figure 5, has been shown via the close-up view in the right part. The boundary condition for the left side of the rectangle was set to have *axial symmetry*, the right side was modeled as electrically insulated, whereas the upper and the

lower sides of the rectangle were modeled as electrodes by assigning them an electric potential. In particular, the lower electrode was set to ground and the upper side was excited by a single nanosecond pulse.

A list of all parameters used in the present simulations is given in Table 1.

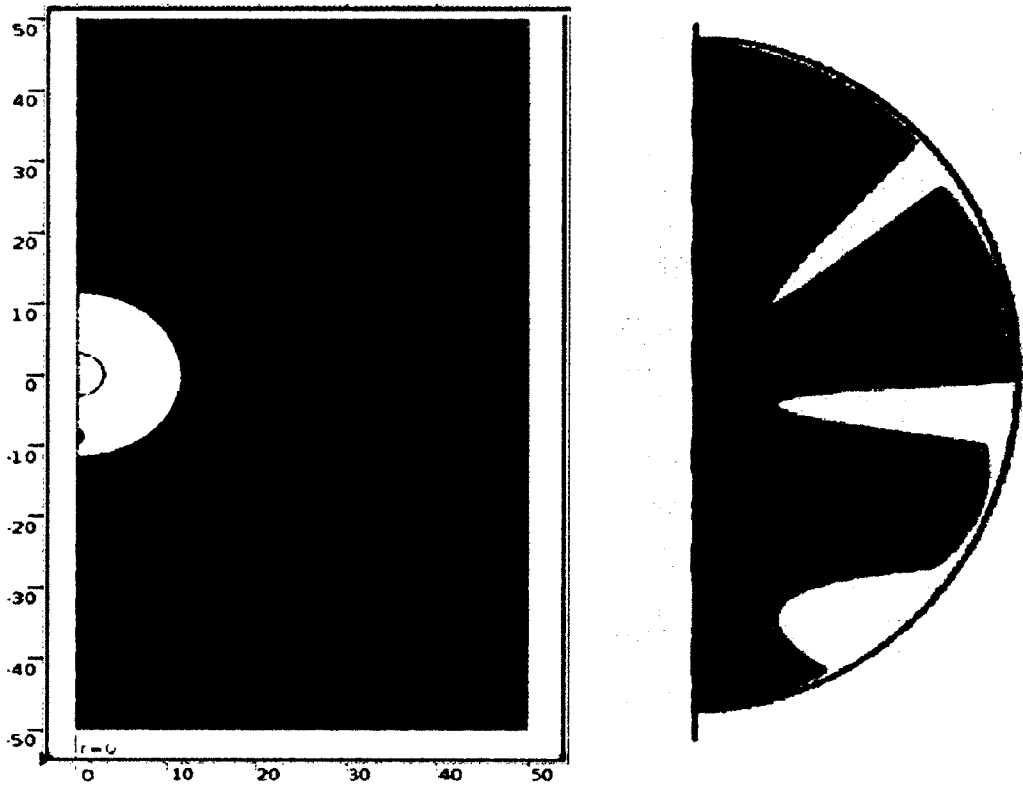


Figure 5. The 2D axisymmetric model used.

Table 1. Parameters used in the electroporation model.

Description/Symbol	Value
Cell radius	10[μm]
Nuclear radius	3[μm]
Mitochondrion size	1 [μm] x 0.7 [μm] x 0.7 [μm]
Plasma membrane thickness	5[nm]
Nuclear membrane thickness	10[nm]
Mitochondria membrane thickness	5[nm]
Extracellular permittivity	72.3 ϵ_0
Extracellular conductivity	1.2[S/m]
Cytoplasmic permittivity	72.3 ϵ_0
Cytoplasmic conductivity	0.5[S/m]
Nucleoplasmic permittivity	72.3 ϵ_0
Nucleoplasmic conductivity	1[S/m]
Mitochondria-plasmic permittivity	72.3 ϵ_0
Mitochondria-plasmic conductivity	0.5[S/m]
Plasma membrane permittivity	5 ϵ_0
Plasma membrane conductivity	$3 \cdot 10^{-7}$ [S/m]
Nuclear membrane permittivity	72.3 ϵ_0
Nuclear membrane conductivity	10^{-4} [S/m]
Mitochondria membrane (OMM)	5 ϵ_0

permittivity	
Mitochondria membrane (IMM) permittivity	$5 \epsilon_0$
Mitochondria membrane (OMM) conductivity	$10^{-4}[S/m]$
Mitochondria membrane (IMM) conductivity	$5 \times 10^{-6}[S/m]$
Electroporation parameter (α)	$10^9[1/(m^2 \cdot s)]$
Equilibrium pore density (N_0)	$1.5 \times 10^9[1/m^2]$
Characteristic voltage of electroporation (V_{ep})	$0.258[V]$
Electroporation constant (q)	2.46
Pore radius (r_p)	$0.76[nm]$
Energy barrier within pore (w_0)	$2.65eV$
Conductivity of aqueous solution in pores (σ_p)	$1.3[S/m]$
Relative entrance length of pores (n)	0.15
Temperature (T)	$295[K]$
Universal gas constant (R)	$8.314[J/K/mol]$
Faraday's constant (F)	$9.65 \times 10^4[C/mol]$

Electric Currents interface mode of the *AC/DC Module (Time Dependent Study)* is chosen for the equation of the electric potential on each calculation domain (i.e. extracellular medium, cell, intracellular organelles), which is expressed as in equation (3.6). TMP is then calculated as the difference between the electric potentials on each side of the membrane structure, and the boundary condition (*Distributed Impedance*) of either inner or outer side of membrane is:

$$n \cdot (J_1 - J_2) = \frac{1}{d_s} \left(\sigma_m + \varepsilon \frac{\partial}{\partial t} \right) (V - V_{ref}) \quad , \quad (3.7)$$

where n is the unit vector normal to the surface, V is the electric potential on the interior side of the boundary, J_1 , J_2 are the current densities through the membrane, d_s is the membrane thickness, σ_m is the conductivity of membrane, V_{ref} is the reference potential on the exterior side of the boundary.

Usually, for simplicity, TMP is taken to be a convenient physical quantity that is indicative of whether the significant electroporation occurs in a cell. The threshold value differs in different types of cell, though, typically, a $\sim 1V$ value is taken as being representative of the critical value for the onset of significant electroporation. Therefore, to save modeling and calculation time, numerical TMP values can be used to compare with experimental data as a simple verification for the accuracy of a model.

However, in order to quantify the pore development and dynamic of electroporation, calculation of pore density number should be included in the model. COMSOL provides three alternative PDE interfaces to add this asymptotic reduction of the Smoluchowski equation into all the membrane boundaries of the model. These are the: *Coefficient Form*

PDE, General Form PDE, and Weak Form PDE (see Appendix I for detailed derivation of Weak Formulation).

Suppose General Form PDE interface is chosen to include equation (3.4), the default governing equation form is:

$$e_a \frac{\partial^2 N}{\partial t^2} + d_a \frac{\partial N}{\partial t} + \nabla \cdot \Gamma = f, \quad (3.8)$$

where e_a, d_a are coefficients, f is source term, Γ is conservative flux.

While equation (3.4) can be transformed as $\frac{dN}{dt} = AA - \frac{AA}{BB}N$, where $AA = \alpha e^{\left(\frac{TMP}{V_{ep}}\right)^2}$, $BB = N_0 e^{q\left(\frac{TMP}{V_{ep}}\right)^2}$. Therefore, all the coefficients are determined as $f = AA - \frac{AA}{BB}N$, $d_a = 1, e_a = 0, \Gamma = \begin{pmatrix} 0 \\ 0 \end{pmatrix}$.

Similarly, membrane conductivity due to electroporation can be simplified as $\sigma_{ep} = N\pi r_p^2 \sigma_p CC / (DD - EE)$, where $CC = e^{P^*} - 1$, $DD = \frac{w_0 e^{w_0 - nP^*} - nP^*}{w_0 - nP^*} e^{P^*}$, $EE = \frac{w_0 e^{w_0 + nP^*} + nP^*}{w_0 + nP^*}$.

However, after careful analysis, when TMP is zero numerically, $CC / (DD - EE)$ has a value of 0/0, for which the solver would encounter a numerical error. Basically, there are two ways to solve this problem: 1) to add a relatively small value to TMP (e.g. 10^{-6}) in order to avoid numerical overflow, which would not affect the result; 2) to apply *L'Hôpital's* rule and obtain the particular expression LH , then use the expression $\sigma_{ep} = N\pi r_p^2 \sigma_p * (LH * (TMP == 0) + \frac{CC}{DD - EE} * (TMP! = 0))$.

3.2 PNP-NS Model

High-intensity, nanosecond electric pulses open nanopores in biological cell membranes which have been observed to display rectifying I - V behavior. Ions transport through nanopores has attracted great attention since it is ultimately related to drug delivery and transport, as well as ions movement through protein in the field of biomedical research.

A continuum model based on the Poisson-Nernst-Planck and Navier-Stokes (PNP-NS) equations has recently been developed and broadly employed to describe the ionic mass transport and hydrodynamic fluid fields phenomena in nanopores or nanochannels.

A remarkable agreement between the theoretical predictions obtained from the PNP-NS model and the existing experimental results suggests that the PNP-NS model is capable of capturing and elucidating the essential physics of the electrokinetic ion transport phenomena in nanopores.

More specifically, the Poisson equation is used to calculate the electric potential by an external electric field, the Nernst-Planck equations address the ionic concentration profiles, and the Navier-Stokes equations are to calculate ionic movement of electroosmosis of viscous drag, which is caused by the electrostatic interaction between the spatial electric field and ionic charge density within nanopores.

3.2.1 PNP-NS Equations

PNP-NS equations are a group of coupled equations including the Poisson Equation, the Nernst-Planck Equation and the Navier-Stokes Equation.

I. The Poisson Equation is a partial differential equation used to describe the spatial electrostatic field, as shown below:

$$-\varepsilon \nabla^2 V = \rho_e = F \sum_{i=1}^n z_i c_i, \quad (3.9)$$

where ε is the solvent permittivity, V the electric potential, ρ_e is space charge density, F the Faraday constant, n denotes total number of the ionic species, c_i denotes molar concentration of i_{th} ionic species, either cation or anion, and z_i denotes the corresponding valences of cations and anions.

II. The Nernst-Planck Equation is a conservation of mass equation used to describe the motion of ion species in a fluid medium. It describes the flux of ions under the influence of both an ionic concentration gradient and electric field.

The flux density N of each aqueous species including the diffusive, electromigrative and convective flux densities is written as:

$$\nabla \cdot N_i = 0, \quad (3.10)$$

$$N_i = u c_i - D_i \nabla c_i + z_i \frac{D_i}{RT} F c_i \nabla V, \quad (3.11)$$

where u denotes the fluid velocity vector, T the absolute temperature of the solution, D_i the diffusion coefficient for the i_{th} ionic species, R the universal gas constant, and equation (3.10) is a consequence of steady-state.

III. The Navier-Stokes Equation is to describe fluid motion in consideration of pressure, viscous force and electric field.

Since the Reynolds numbers of the electroosmotic flow in nanopores are extremely small, the inertial terms in the Navier-Stokes equations are neglected and model the fluid motion with the continuity equation, shown below:

$$\nabla \cdot \mathbf{u} = 0, \quad (3.12)$$

The fluid motion was taken to be governed by Stokes equations as given below:

$$-\nabla P + \mu \nabla^2 \mathbf{u} - \rho_e \nabla V = 0. \quad (3.13)$$

where P is the pressure, μ is the fluid viscosity.

3.2.2 Dimensionless Form of PNP-NS Model

The dimensionless form of the equations has been used to remove units from the equations involving physical quantities by a suitable substitution of variables. The most significant advantage is to avoid round-off due to manipulations with small numbers (or large differentials in values) in the case of nanopore. Meanwhile, the physical quantities can be recovered from the dimensionless form.

RT/F , is used as the electric potential scale, denoted by V_∞ ; solvent concentration is used as a scaled ionic concentration, denoted as C_∞ ; nanopore tip radius is used as length scale, denoted as L_∞ ; $U_\infty = \frac{\varepsilon}{\mu L_\infty} \cdot (V_\infty)^2$ is used as velocity scale; $P_\infty = \mu \frac{U_\infty}{L_\infty}$ is used as the pressure scale.

The dimensionless PNP-NS equations are given below (symbols with asterisk represent the variables of dimensionless form; see Appendix II for detailed derivation):

$$-\nabla^{*2}V^* = \rho_e^* = \frac{L_\infty^2 C_\infty}{\varepsilon V_\infty} F \sum_i^n z_i c_i^* , \quad (3.14)$$

$$\nabla^* \cdot N_i^* = 0 , \quad (3.15)$$

$$N_i^* = u^* c_i^* - D_i^* \nabla^* c_i^* - z_i D_i^* C_i^* \nabla^* V^* , \quad (3.16)$$

$$\nabla^* \cdot u^* = 0 , \quad (3.17)$$

$$-\nabla^* P^* + \nabla^{*2} u^* - \sum_i^n z_i c_i^* \nabla^* V^* F C_\infty \frac{V_\infty}{P_\infty} = 0 . \quad (3.18)$$

3.2.3 Simulation Analysis Method

A finite element model of a nanopore with reservoir on both ends was constructed in COMSOL Multiphysics 4.3b.

The simulation geometry of the bio-membrane nanopore with axial length L (~ 5 nm) and a conical cross-section with radii R_l and R_r is shown in the schematic of Figure 6. A cylindrical system with axial z and radial r coordinates with the origin fixed at the center of the nanopore has been used for this axisymmetric geometry. The simulation region is represented by the outer boundary ABCDEFGH, the line of symmetry by AH, while the line segments, AB, BC, FG, and GH, represent the regions in the reservoirs.

The various parameters, including those associated with the electrolytic medium such as the permeabilities of the ions, the fluid density ρ , dynamic viscosity μ , permittivity ε , etc. are given in Table 2.

Table 2. Parameters used in the transport simulations

Symbol	Value	Description
C_0	140[mol/m ³]	Bulk concentration
μ	0.001[Pa · s]	Viscosity
$D1$	2.0549x10 ⁻⁹ [m ² /s]	Diffusivity of Cs ⁺
$D2$	1.0881x10 ⁻⁹ [m ² /s]	Diffusivity of Acet ⁻
R	8.31[J/mol/K]	Universal gas constant
F	9.649x10 ⁴ [C/mol]	Faraday constant
T	295[K]	Temperature
ϵ	72.3 ϵ_0	Permittivity
L	5[nm]	Length of nanopore
ρ	1000[Kg/m ³]	Fluid density

The ends of the pore were assumed to be connected to two fluid reservoirs. The wall of the nanopore (segment DE in Figure 6) would bear a surface charge density, σ . No charge was assigned to the reservoir walls (segments CD and EF). The bulk ionic concentrations were maintained at a constant value as boundary conditions far away from the conical nanopore. An external electric potential was applied between the left (segment AB) and right (segment GH) reservoirs to generate the ionic current. For clarity,

charged spherical particles representing the mobile ions are also shown within the nanopore in Figure 6.

A nonslip boundary condition (i.e., $u = v = 0$) was specified on segments CD, DE, and EF of Figure 6. A normal flow with $p = 0$ was applied to the planes of AB and GH, which are far away from the nanopore. An axisymmetric boundary condition was imposed on AH. Slip boundary conditions were used on segments BC and FG since they are far away from the entrances of the nanopore. The normal ionic flux was taken to be zero at segments CD, DE, and EF which are the walls of the reservoirs and the nanopore on grounds that these solid surfaces are impervious to ion transport. Similarly, zero normal ionic flux condition was used along AH due to the axial symmetry, and also along segments BC and FG since they are in the bulk electrolyte reservoirs. Furthermore, the ionic concentrations were taken to equal those of the bulk experimental values at segments AB and GH. Finally, the potentials at the two boundaries AB and GH were taken to be V_{bias} and 0, respectively, with V_{bias} being the externally applied bias.

The walls of the reservoirs, CD and EF, are assumed to be uncharged, so that $n \cdot \nabla^* V^* = 0$ at these boundaries. Since the surfaces BC and FG are far away from the nanopore and are in the bulk electrolyte reservoirs, a no charge boundary condition was set at these surfaces for the potential. Finally, due to the possibility of a surface charge density σ lining the inner walls of the pore (segment DE), the condition of: $n \cdot (-\nabla^* V^*) = \sigma^* = \frac{FL\infty}{RT\epsilon} \sigma$ was applied.

The boundary conditions are summarized in Table 3.

Table 3. Boundary conditions used in the simulations

Poisson Equation	
A-H	Axial Symmetry
A-B	Electric Potential (V_{bias}^*)
H-G	Ground
D-E	Surface Charge (σ^*)
B-C; C-D; E-F; F-G	Zero Charge
Nernst-Planck Equation	
A-H	Axial Symmetry
A-B; H-G	Concentration (c_i/C_∞)
B-C; C-D; D-E; E-F; F-G	No Flux ($-n \cdot N_i^* = 0$)
Stokes Equation	
A-H	Axial Symmetry
A-B	Inlet ($P = 0$)
H-G	Outlet ($P = 0$)
D-E	Wall -> No Slip
B-C; C-D; E-F; F-G	Wall -> Slip

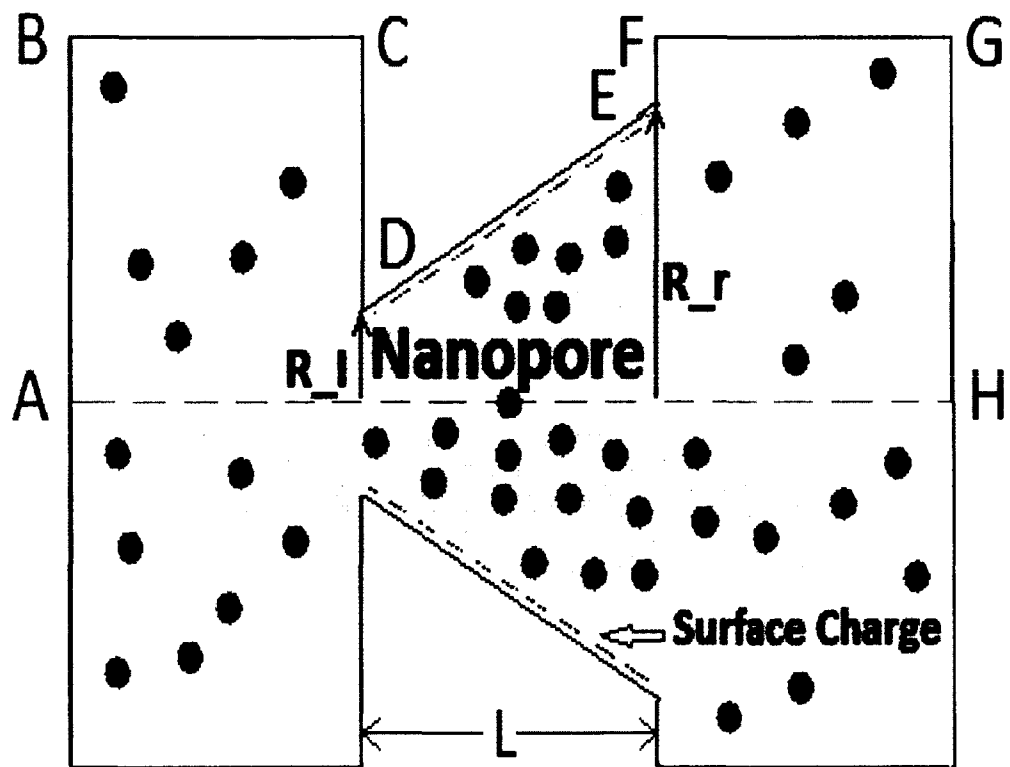


Figure 6. Schematic of a nanopore.

CHAPTER 4

SIMULATION RESULTS AND DISCUSSION

4.1 Simulation Results of Electroporation Model

The electroporation model discussed in Chapter 3 was used for evaluations of the transmembrane potential and pore densities through numerical simulations. Various membrane structures of intracellular organelles (e.g. irregular-shaped mitochondrion, spherical liposome etc.) were included to explore geometric impact on pore dynamics under pulses with different amplitude and duration.

4.1.1 Model Verification

First, numerical result of transmembrane potential by an electric field is compared with analytical solution to ensure the validity and accuracy of numerical model.

The analytical solution under time-dependent condition is given [65]:

$$TMP = f_s ER \cos\theta \left(1 - e^{-\frac{t}{\tau}}\right), \quad (4.1)$$

$$\text{and } f_s = \frac{3\sigma_e [3dR^2\sigma_i + (3d^2R - d^3)(\sigma_m - \sigma_i)]}{2R^3(\sigma_m + 2\sigma_e) \left(\sigma_m + \frac{1}{2}\sigma_i\right) - 2(R - d)^3(\sigma_e - \sigma_m)(\sigma_i - \sigma_m)}, \quad (4.2)$$

$$\tau = \frac{R \frac{\epsilon_m}{d}}{\frac{2\sigma_e\sigma_i}{2\sigma_e + \sigma_i} + \frac{R}{d}\sigma_m}. \quad (4.3)$$

where E is an electric field exerted on a spherical cell with outer radius R , θ is the angle between the direction of the electric field and line connecting point on the membrane and cell center, f_s is a function reflecting properties of the cell and medium, $\sigma_i, \sigma_e, \sigma_m$ are the

conductivities of cytoplasm, extracellular medium and membrane, respectively, and d is thickness of membrane. When $t = \infty$, the stationary solution can be obtained.

By applying simplifying assumption that the membrane is a pure insulator, $\sigma_m \cong 0$, and hence $f_s \cong \frac{3}{2}$.

The TMP on the plasma membrane obtained from numerical and analytical methods are compared as shown in Figure 7 under stationary study and Figure 8 under time-dependent study in the case of $\cos(\theta) = 0$ when the external electric field is 1 kV/cm . The model setup is the same as discussed previously in Chapter 3. The plasma membrane serves as a thin layer boundary condition (*Distributed Impedance*) in the simulation. Figure 7 indicates that the results between numerical and analytical methods are in a good agreement with each other under both stationary and time-dependent cases. Meanwhile, as is shown in Figure 8, the error between these two methods depends on the position, but is no more than 0.3% everywhere on the outer membrane, which is acceptable. If the mesh on the membrane is made finer, the error could decrease somewhat more.

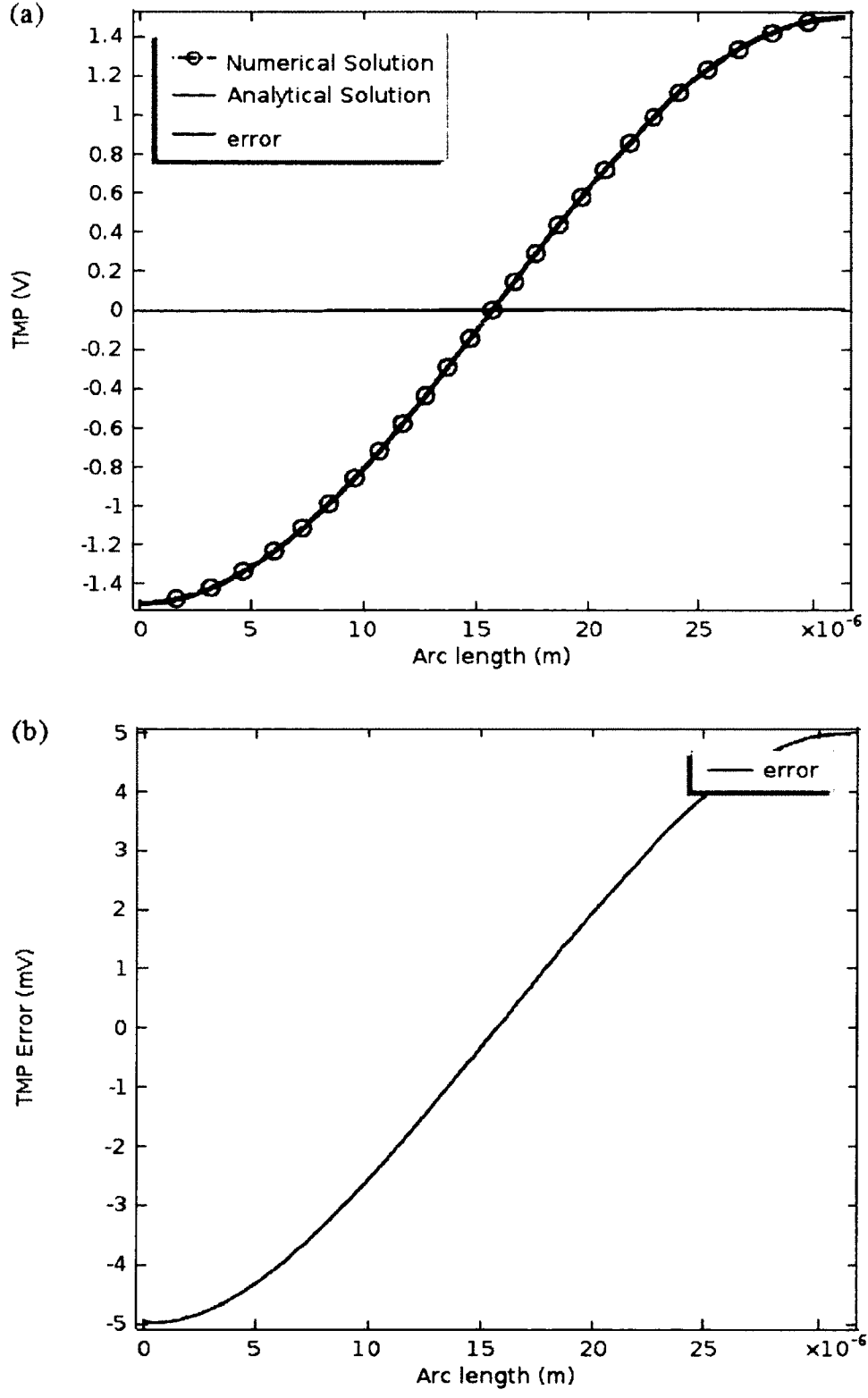


Figure 7. TMP comparison between numerical and analytical methods (stationary).

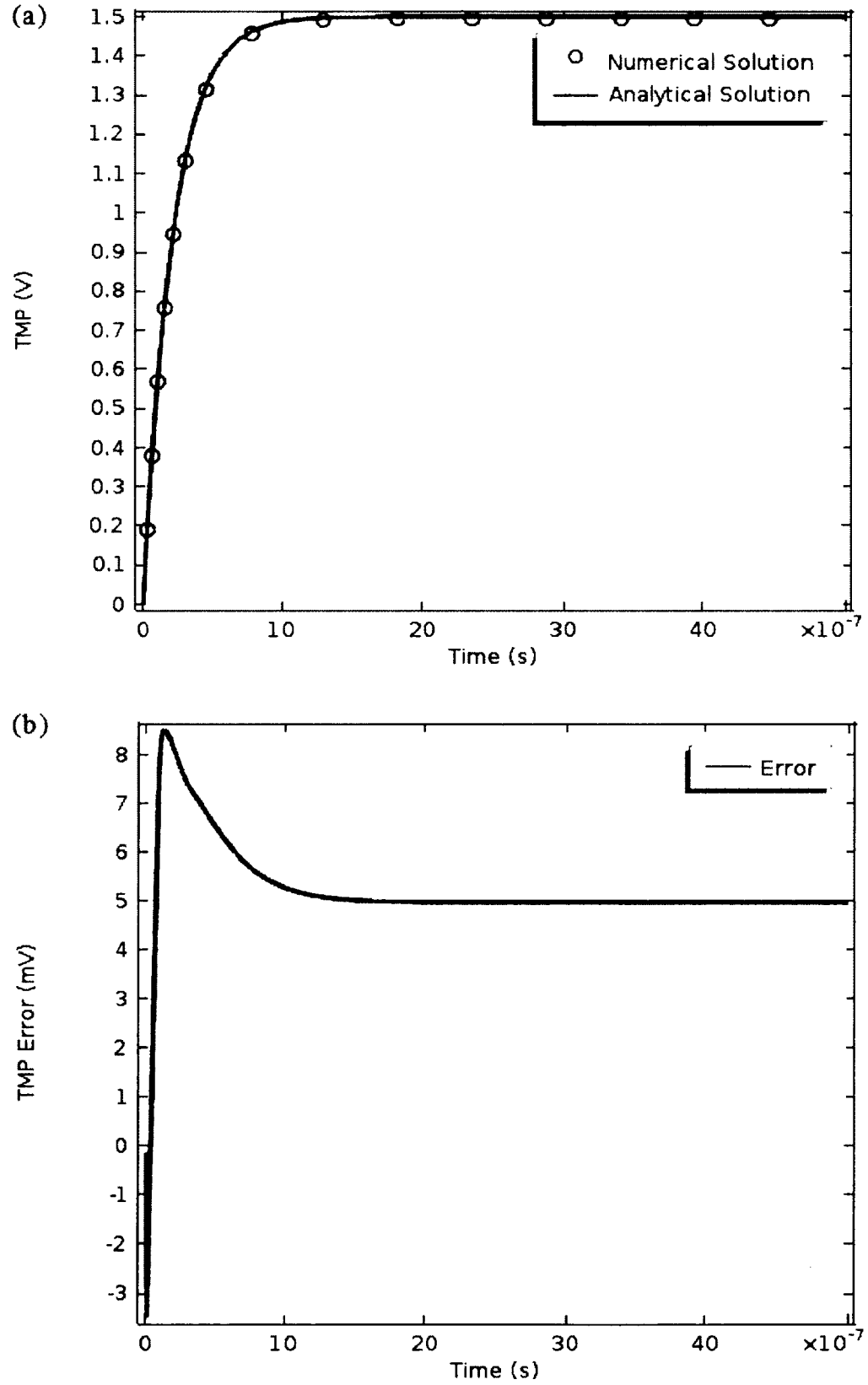


Figure 8. TMP comparison between numerical and analytical methods (time-dependent).

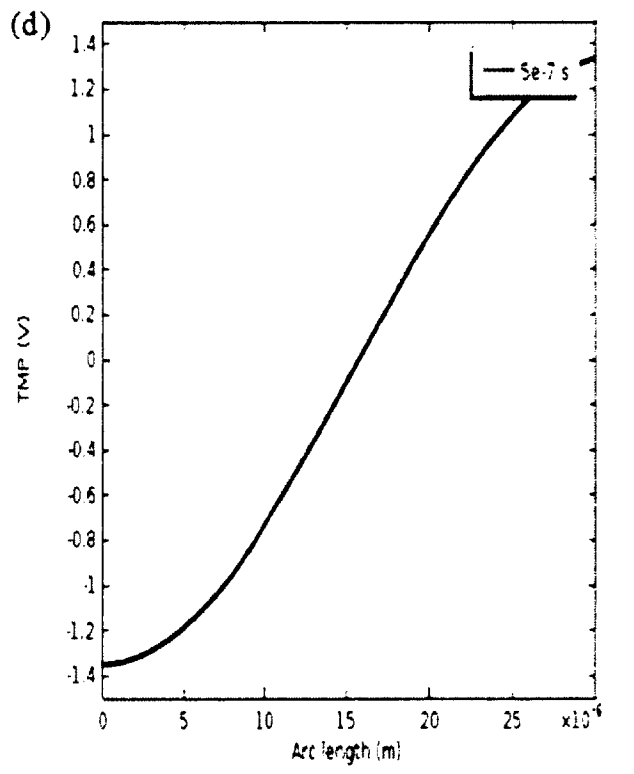
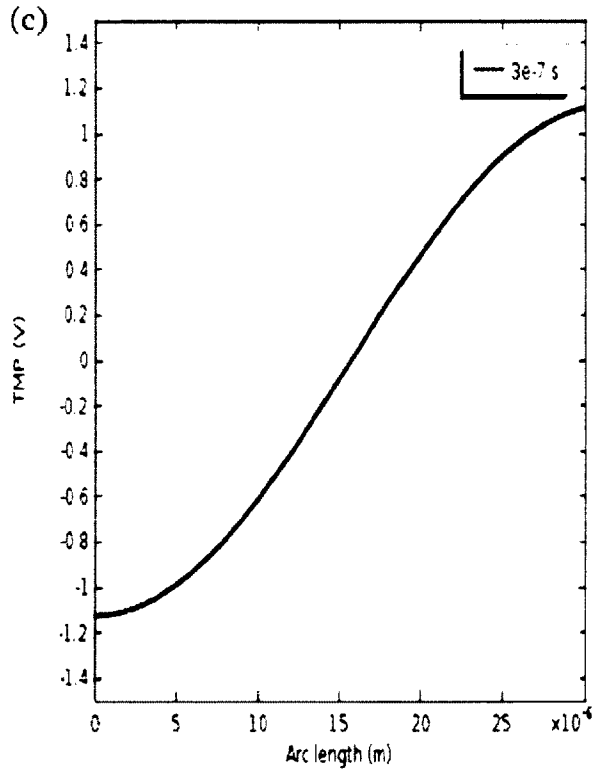
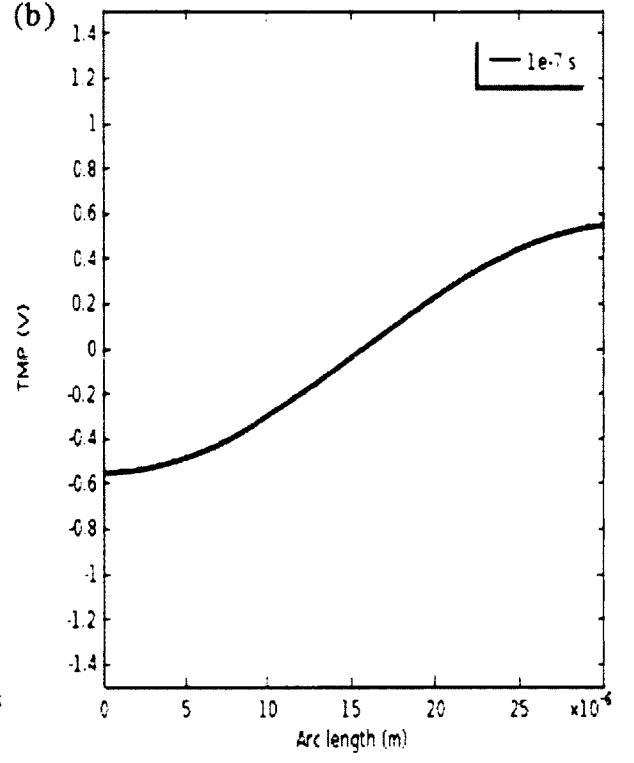
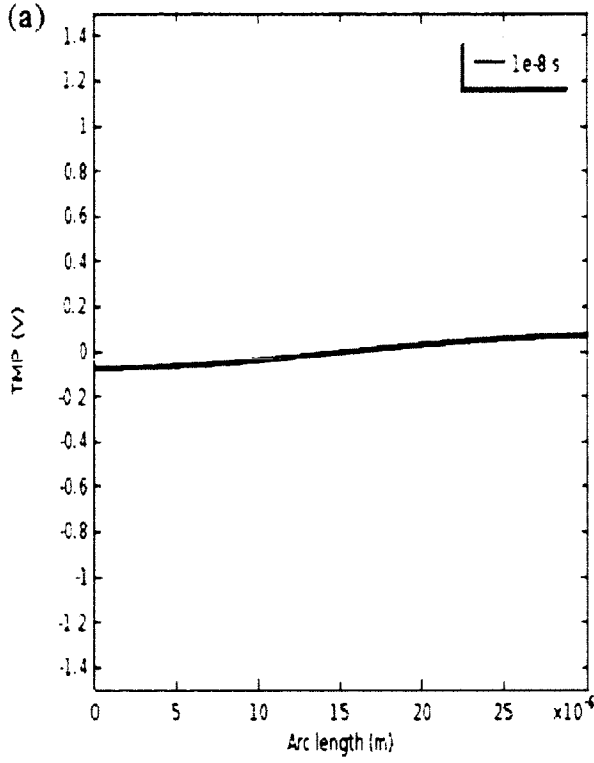
4.1.2 Simulation Results

The model is then used to explore the transmembrane potential and pore densities on the plasma membrane, nuclear membrane and the liposome membrane.

4.1.2.1. TMPs and Pore Density of Plasma Membrane

(A) Calculations of TMP Without Including Pores In The Model

The time course of transmembrane potential on plasma membrane is presented in Figure 9. The calculation does not include the pore development in the model, which simply shows the dynamic time course of transmembrane potential. The results show that after a step change of the electric field, TMP gradually forms and becomes greater on the plasma membrane. After a few microseconds, an almost steady-state value is shown. The amplitude depends on the position on the plasma membrane, which is shown by the arc length in the figures. In this particular case, due to the symmetry of the model, the highest absolute value is around 1.5 V after 1 microsecond.



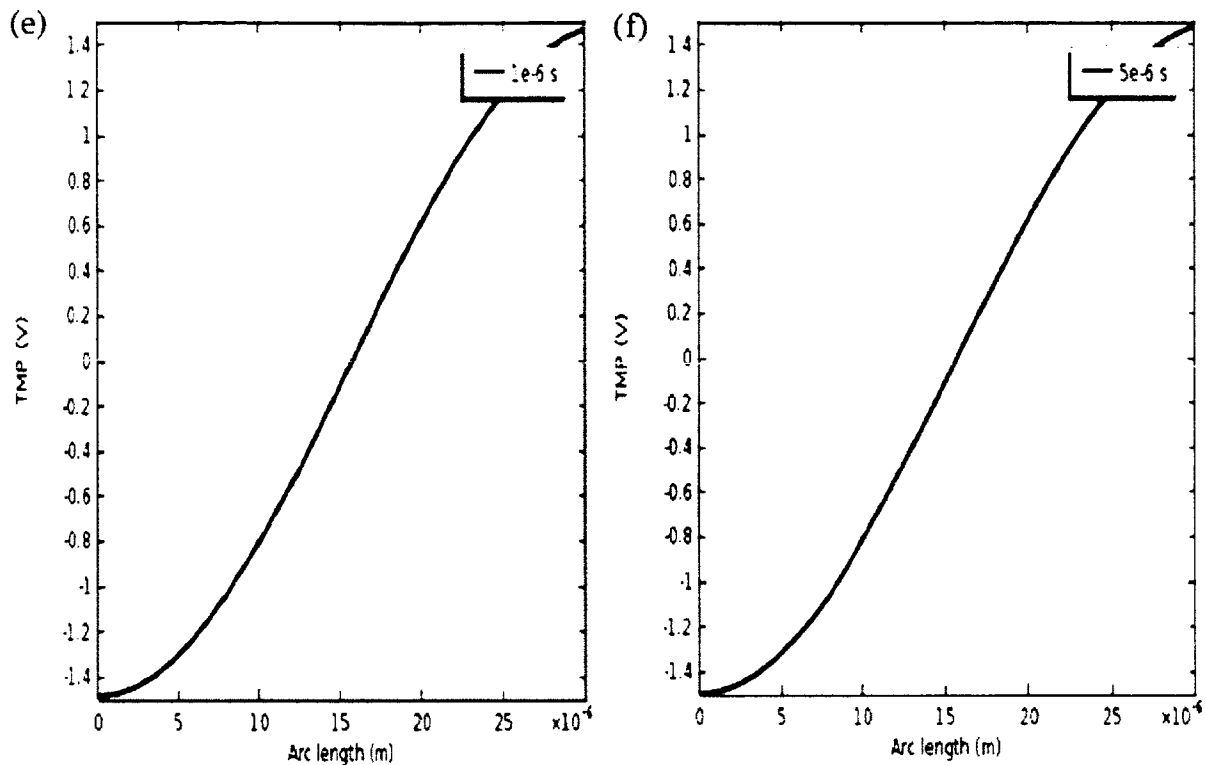
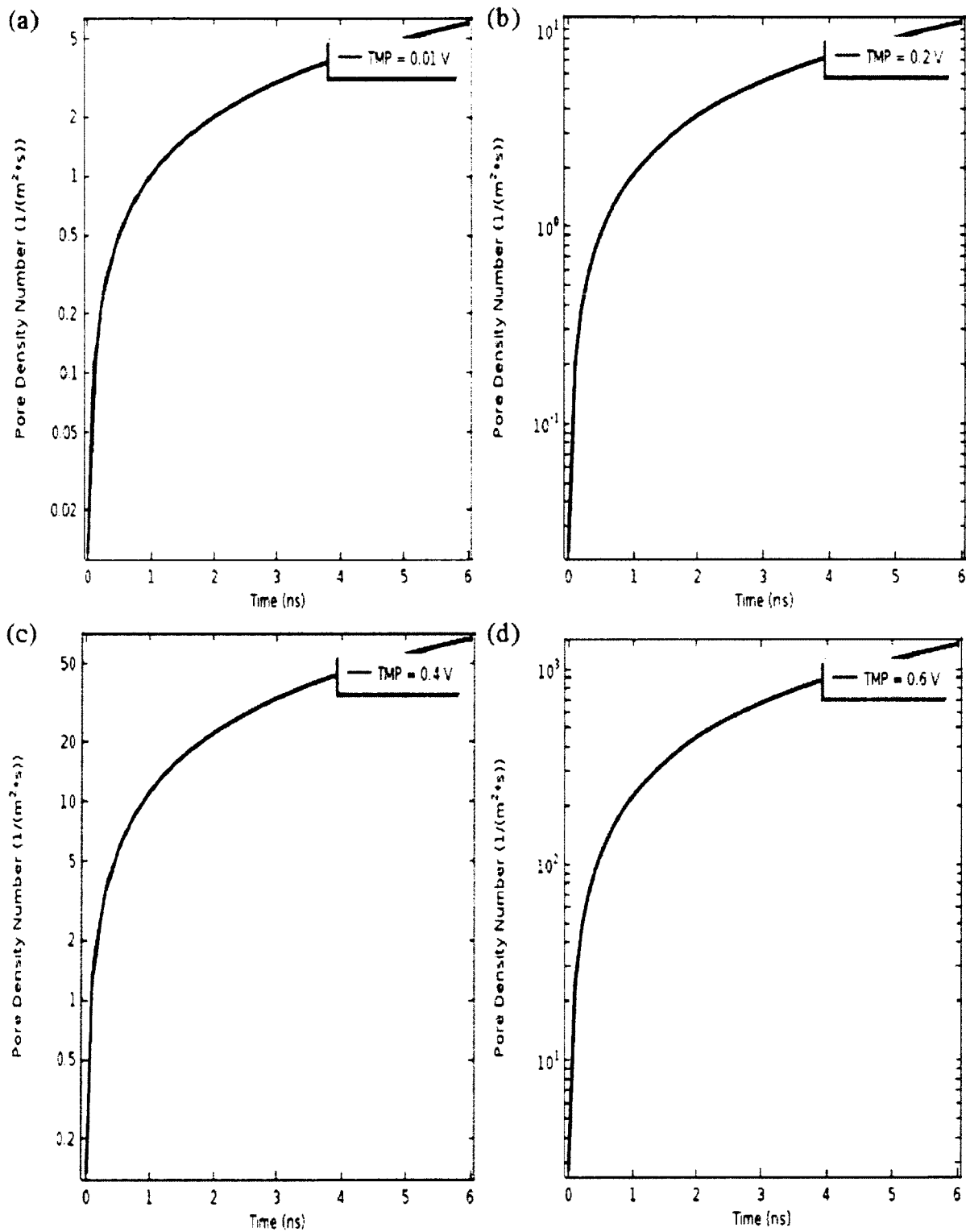


Figure 9. Time course of transmembrane potential on plasma membrane. The various snapshots were at time instants of: (a) 10 ns, (b) 100 ns, (c) 300 ns, (d) 500 ns, (e) 1 μ s, and (f) 10 μ s.

(B) Pore Densities at fixed TMPs

The pore density number at fixed transmembrane potential value is shown in Figure 10. The range of transmembrane potential varies from 0.01 V to 1.5 V. Usually, the pore density number and transmembrane potential are coupled together and have a mutual influence. Specifically, the ODE interface is used here to calculate the pore dynamics under specified TMP values. As is shown, a larger TMP value usually means greater pore number density. In Figure 10, as the TMP value is becoming greater, more pores are predicted to develop on the membrane. However, the relationship between

transmembrane potential and pore density does not always have to be positive. For instance, more pores would mean more conducting current through pores, which would decrease the electric potential across the membrane since the collectible membrane resistance would then decrease. In such cases, the transmembrane potential could decrease somewhat and lead to a lower pore density.



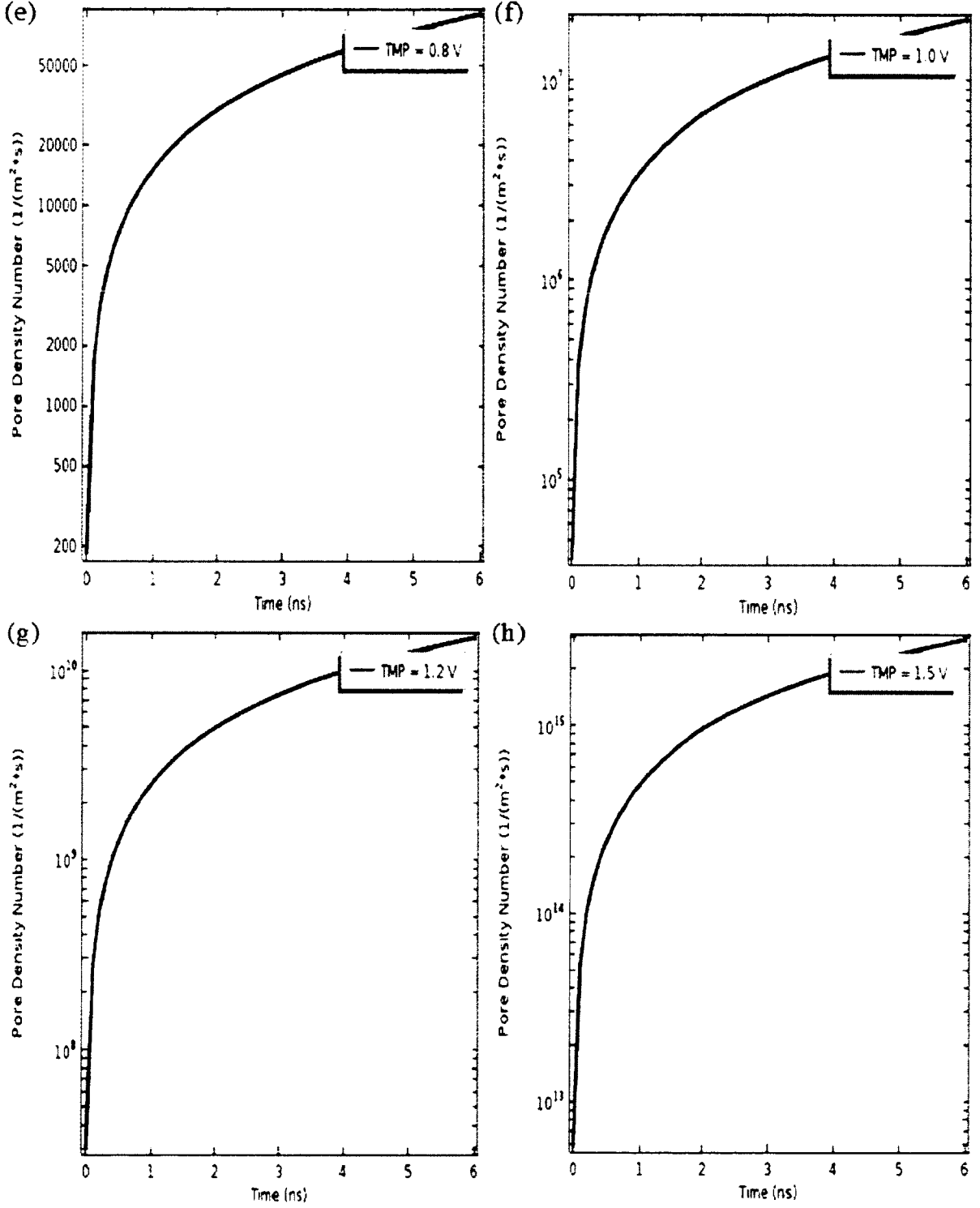


Figure 10. Time course of pore density on plasma membrane at different TMP values. The values were: (a) 0.1 V, (b) 0.2 V, (c) 0.4 V, (d) 0.6 V, (e) 0.8 V, (f) 1.0 V, (g) 1.2 V, and (h) 1.5 V.

4.1.2.2. Model with Liposome

(A) TMP and Pore Density of Liposome with Different Radii

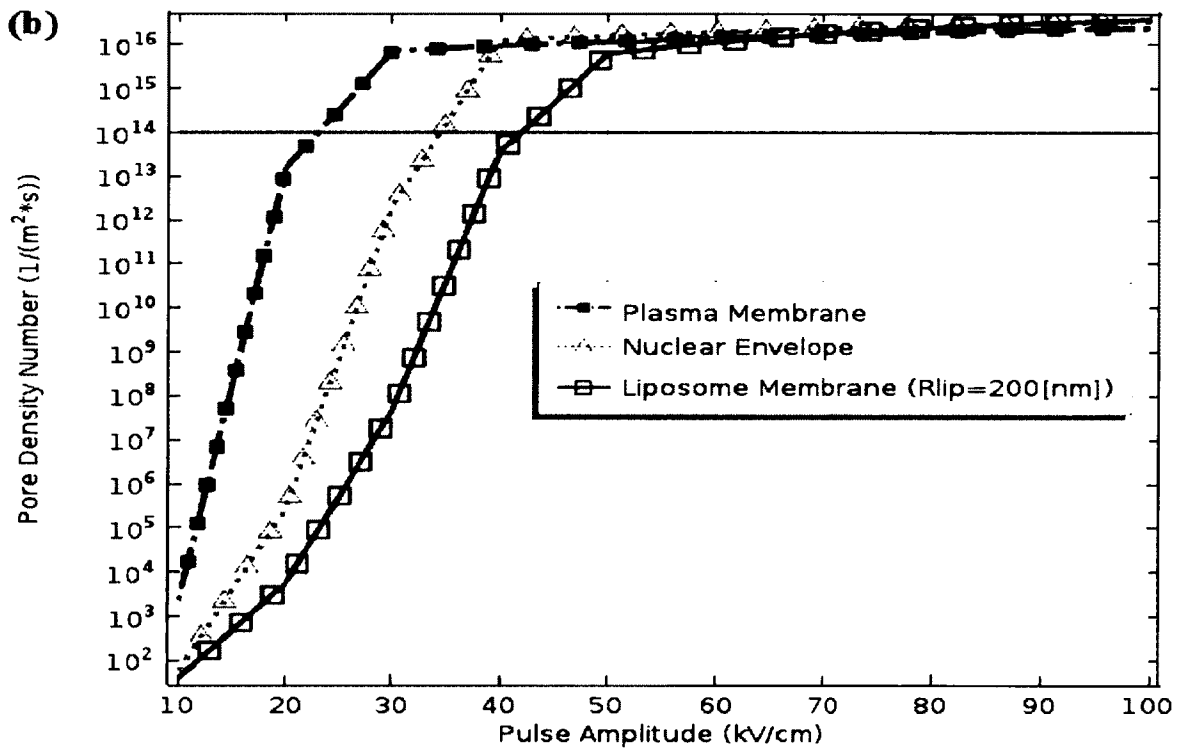
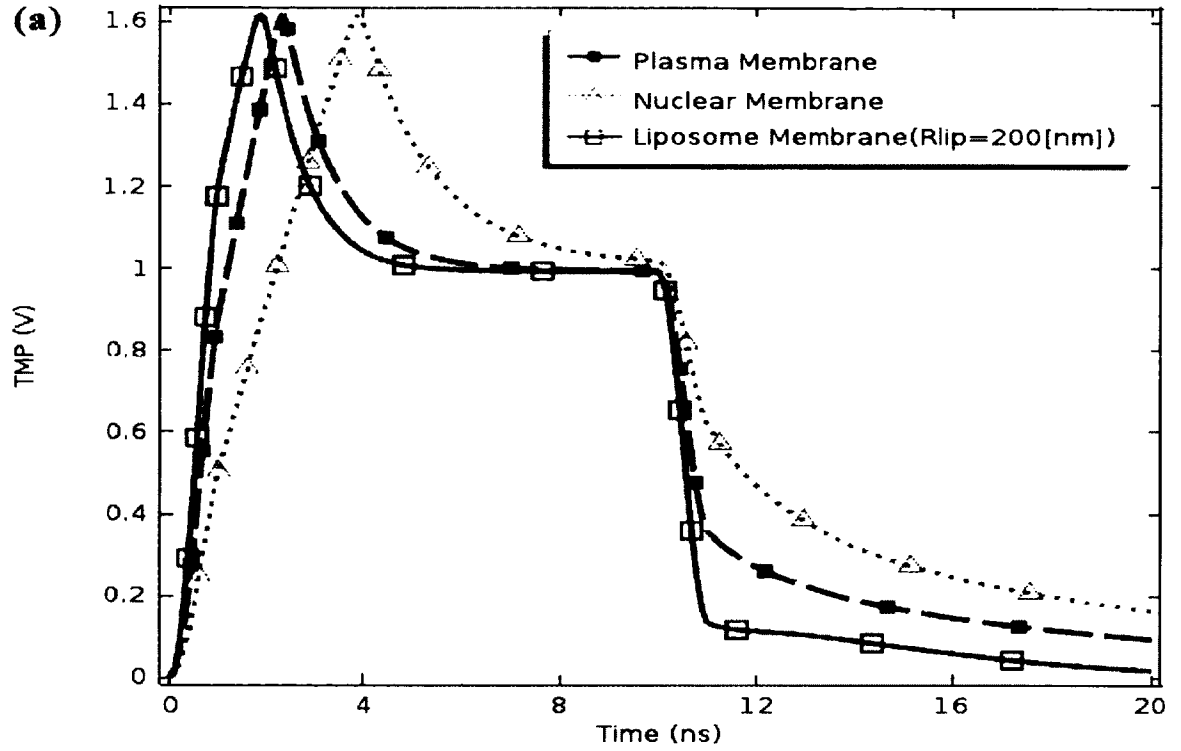
The model was employed to calculate the TMP and pore density on the plasma membrane, nuclear membrane and the membrane of liposome with different radii, as shown in Figure 11.

Figure 11a shows the time evolution of TMP on the plasma membrane, the nuclear membrane and a liposome with 200 nm radius after exposure to a typical pulse with 10 ns (rise/fall time is 1 ns) duration and a 80 kV/cm maximum electric field amplitude. As observed, in a few nanoseconds, the TMPs of the plasma, nuclear and the liposome membranes rise rapidly to above 1.6 V before falling back to approximately 1 V at 10 ns. The decrease in TMPs results from an increase in the pore density due to electroporation, which increases the membrane conductivity and consequently leads to an electric potential drop across the membranes.

Figure 11b indicates the pore density at the membrane poles at the pulse exposure time of 10 ns with pulse amplitude ranging from 10 to 100 kV/cm obtained under parametric simulation study. As observed, the plasma membrane, nuclear membrane and membrane of liposome with radius of 200 nm are significantly electroporated at 22 kV/cm, 34 kV/cm and 42 kV/cm, respectively. Thus, it is easier to porate the outer plasma membrane, though the inner organelle could be porated by such a short-duration pulse.

Figure 11c provides TMPs of liposome with radii of 80, 100, 200, 250, 400 and 500 nm as a function of time. The pulse characteristics are the same as the one for Figure 11a. As observed in Figure 11c, liposome radius size plays an important role on TMP

development. As the radius becomes larger, the TMP attains its maximum value quicker. Therefore, to electroporate smaller liposome, a higher amplitude of electric pulse is required, which is shown in Figure 11d. For a liposome with 500 nm radius, a pulse with an amplitude of 20 kV/cm is seen to be required to electroporate. However, for a smaller liposome, e.g., one with a radius of 80 nm, a pulse amplitude of 93 kV/cm is required for electroporation.



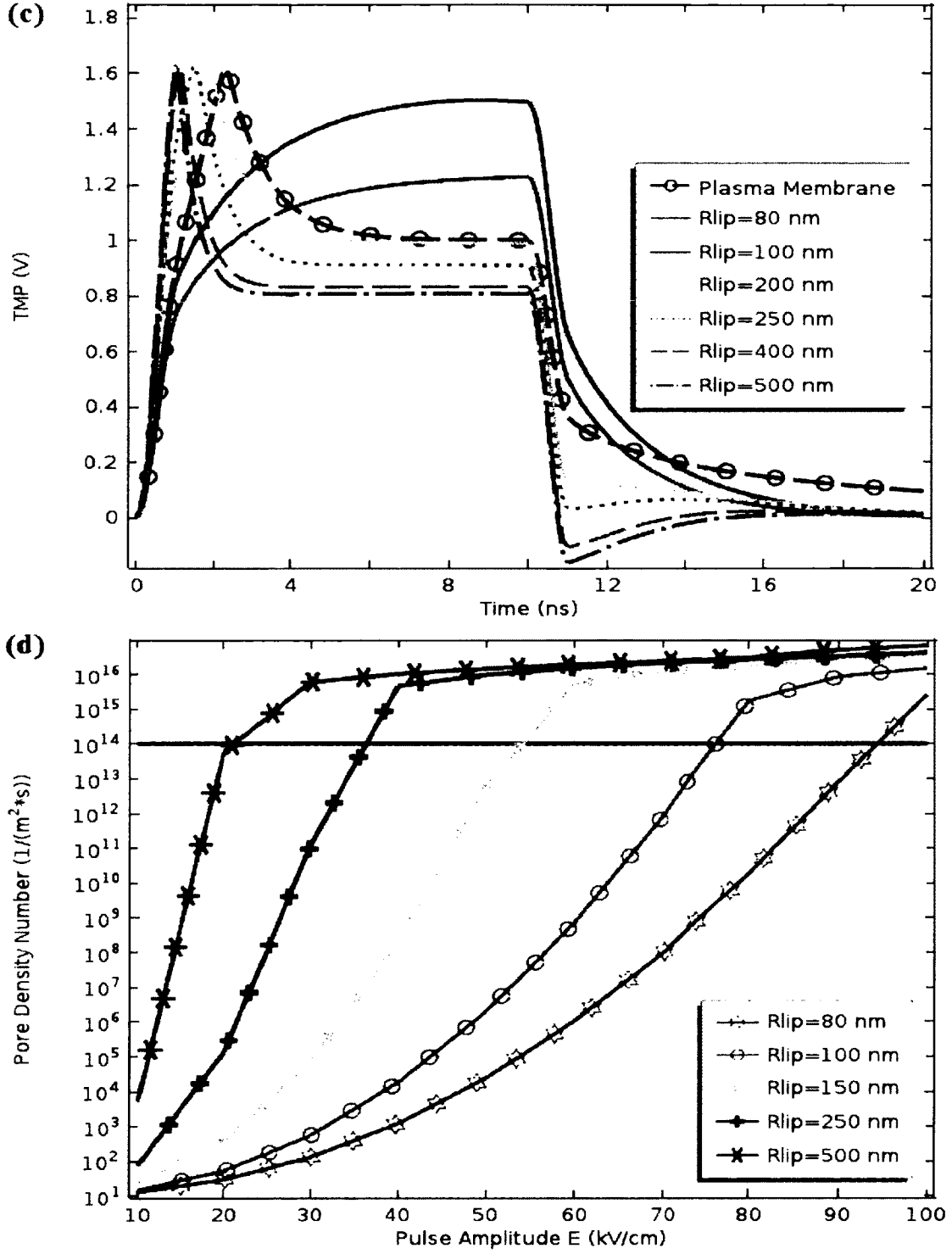


Figure 11. TMP and pore density number of membranes in cell. (a) Time evolution of TMP on plasma membrane, nuclear membrane and liposome membrane. (b) Pore density of membrane poles after 10 ns pulse. (c) Time evolution of TMP on plasma membrane and liposome membrane with different radii. (d) Pore density of liposome membrane poles with different radii after 10 ns pulse.

(B) Analysis of Pulse Parameters

In order to electroporate liposome while keeping the plasma membrane intact, a parametric analysis was performed using different pulsing parameters. The influence of pulse duration and the electric properties of the liposome and cell membrane were probed. Two typical different pulse durations of 4 ns and 10 ns were employed, and liposome with radii of 80 nm and 200 nm were included in the model for each parametric run.

Figures 12a-b show the influence of liposome membrane conductivity ranging from 0.01-- 2 S/m. Liposomes with higher conductive medium would be electroporated at a somewhat lower amplitude. Furthermore, this parameter has little influence on electroporation of plasma membrane.

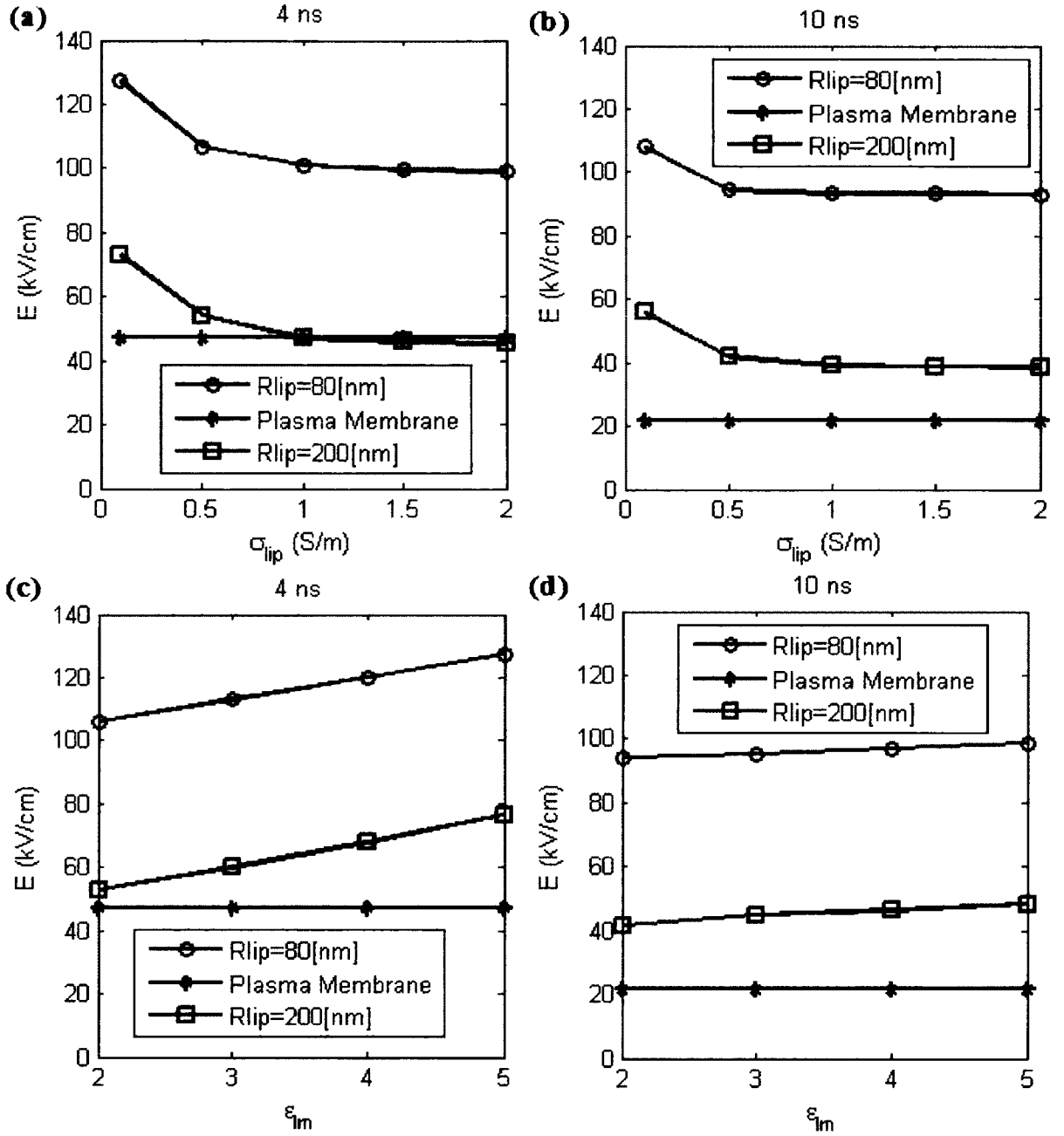
Figures 12c-d show the influence of liposome membrane relative permittivity ranging from 2 to 5. Liposomes with higher membrane permittivity need a pulse with a higher amplitude. However, as the pulse duration becomes longer, the impact fades away. Also, this parameter has no impact on plasma membrane poration.

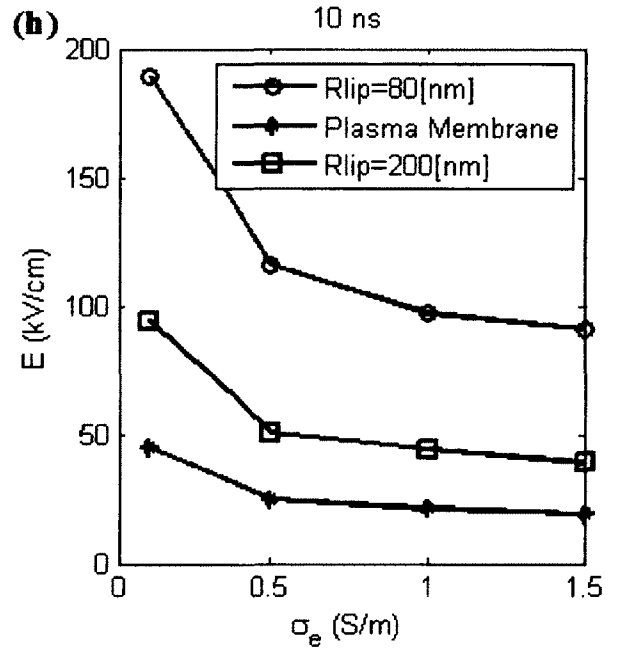
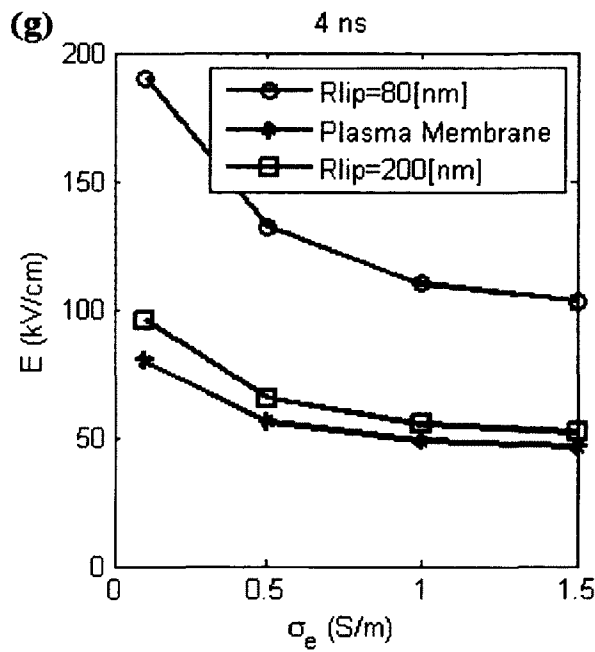
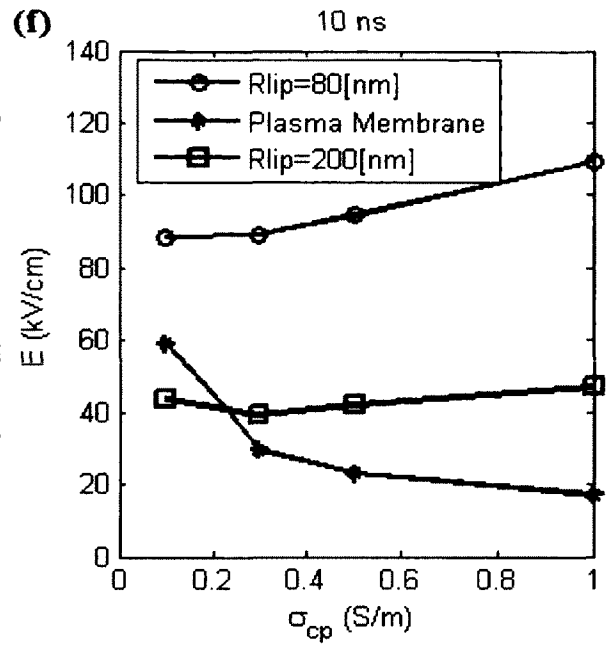
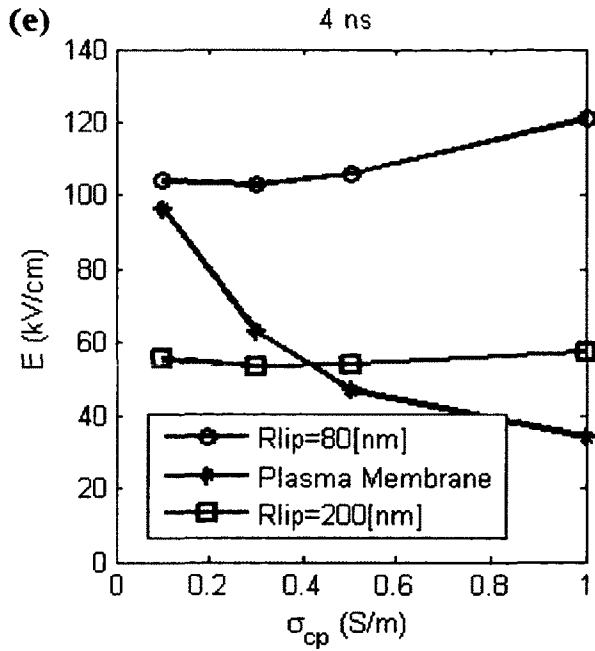
Figures 12e-f show the influence of cytoplasmic conductivity ranging from 0.1 to 1 S/m. As this value becomes lower, the amplitude required for electroporation of the plasma membrane is increased rapidly. This means that at certain value it is likely to selectively electroporate liposomes but keep plasma membrane intact. For example, when $\sigma_{cp} = 0.1 \text{ S/m}$, then with a 60kV/cm and 4 ns pulse, a liposome with radius of 200 nm could be electroporated, while the plasma membrane and a liposome with radius of 80 nm would remain intact.

Figures 12g-h show the influence of the extracellular medium conductivity ranging from 0.01 to 1.5 S/m. As this value becomes larger, the amplitude required for electroporation decreases. In the figures the calculations indicate that higher amplitudes are required for electroporation in low conductivity medium below 0.5 S/m.

Figures 12i-j show the influence of conductivity of the plasma membrane ranging from 10^{-10} to 10^{-4} S/m. This parameter has no impact on the electroporation of liposomes or plasma membrane. As is shown, for longer durations, lower amplitudes are required for electroporation. However, this trend is more obvious for the plasma membrane.

The presented parametric analysis shows that some parameters can be modified in order to selectively electroporate liposomes while keeping the plasma membrane intact. Hence, a combination of parameters that might lead to selective liposome electroporation was chosen to calculate the membrane electroporation. The updated parameters chosen were as: pulse duration 4 ns, $\sigma_{lip} = 2$ S/m, $\epsilon_{tm} = 2.1$ (unchanged), $\sigma_{cp} = 0.1$ S/m, $\sigma_e = 0.1$ S/m, $\sigma_{pm} = 3e - 7$ S/m (unchanged).





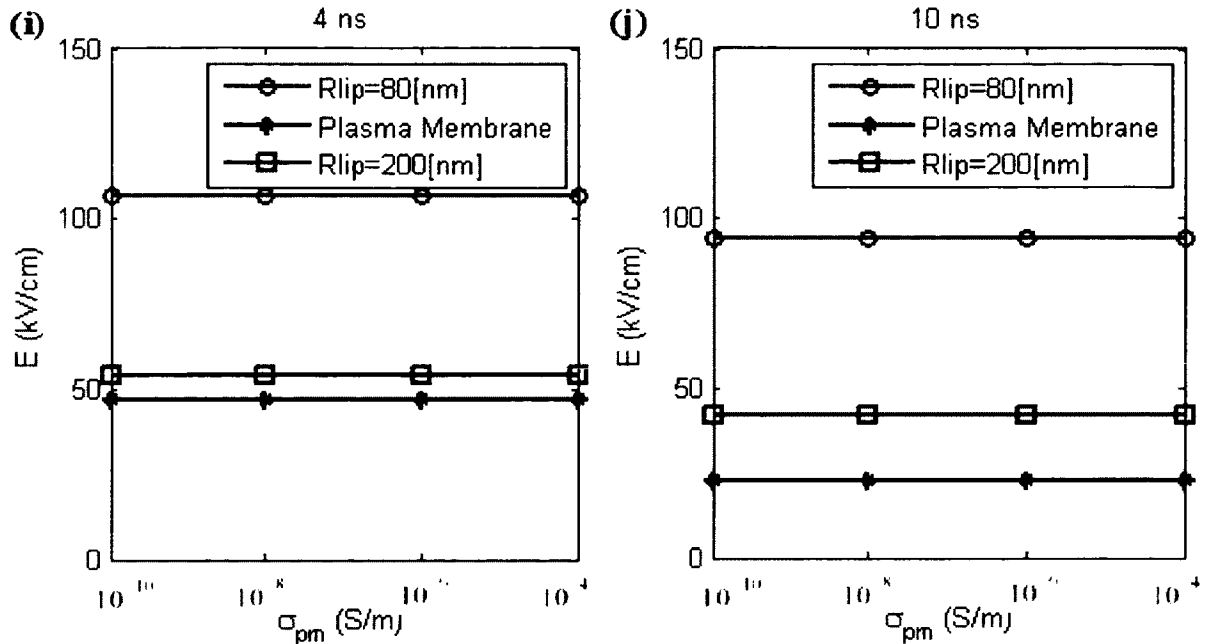


Figure 12. Amplitudes required to electroporate plasma membrane and liposome membranes with two different radii. The various parametric changes included in these figures are discussed in the text.

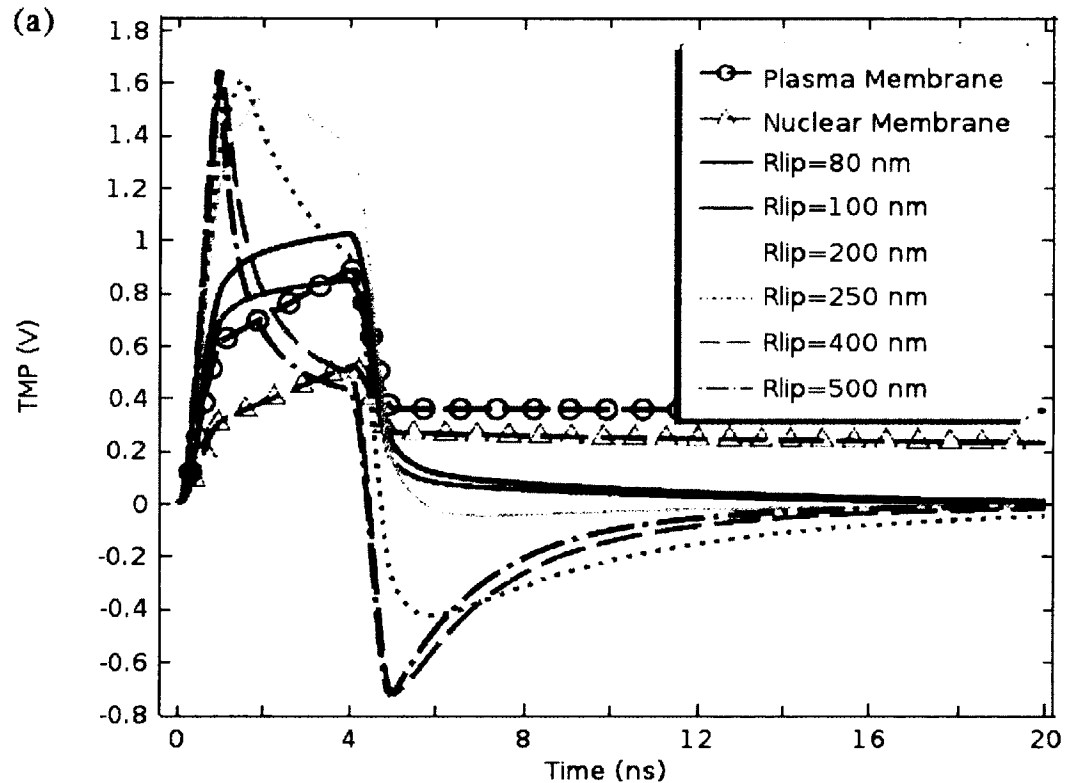
(C) TMP and Pore Density of Liposome after Optimization

By using the optimized parameters of pulse duration and electric property of cell, TMP and pore density obtained are demonstrated and discussed in Figure 13.

Figure 13a shows the time evolution of TMP on the plasma membrane, the nuclear membrane and a liposome with various radii after exposure to a typical pulse with 4 ns (rise/fall time is 1 ns) and 80 kV/cm electric field amplitude. As observed, TMPs of larger liposome rise rapidly to above 1.6 V at around 1 ns, while TMP values of the plasma membrane and nuclear membrane take 4 ns to achieve their maximum values, which both are less than 1 V. Also, smaller liposomes takes more time to reach the peak

value. Therefore, liposomes with a radius greater than 100 nm are electroporated before the plasma membrane or nuclear membranes.

Figure 13b shows the pore density at the membrane poles at the pulse exposure time of 4 ns with a pulse amplitude ranging from 10 to 250 kV/cm under a parametric simulation study. As observed, liposomes with radii greater than 100 nm are electroporated before the plasma membrane or nuclear membranes. Liposomes with radius 500 nm, 250 nm, 200 nm, 100 nm need only 30 kV/cm, 60 kV/cm, 70 kV/cm, 80 kV/cm and 120 kV/cm electric fields, respectively, for electroporation. On the other hand, the plasma membrane and nuclear membrane need electric fields around 130 kV/cm and 230 kV/cm, respectively, for electroporation.



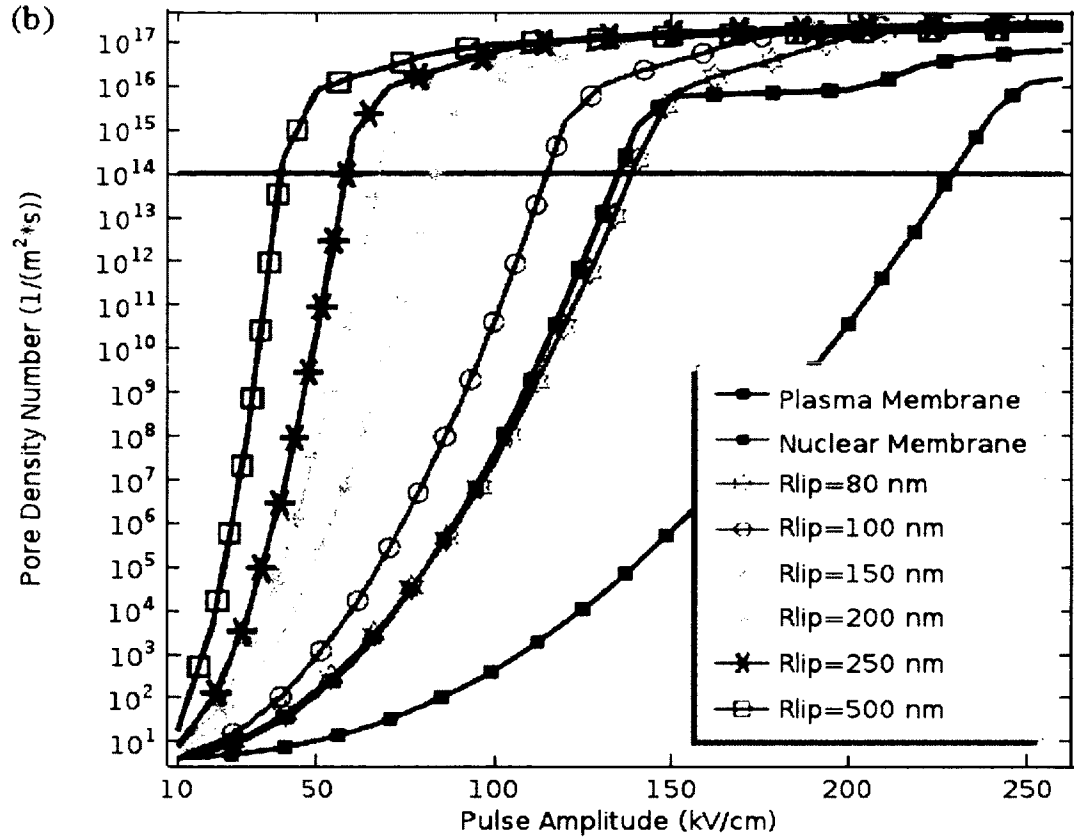


Figure 13. Optimized TMPs and pore density number of membranes in cell. (a) Time evolution of TMP on plasma membrane, nuclear membrane and liposome membranes. (b). Pore density of membrane poles after 4 ns pulse.

4.1.2.3. TMP and Pore Density of Intracellular Organelle (Mitochondrion)

In this part, the primary objectives are to probe differences in TMP generation with variations in pulse width and the rise/fall times in the model, including mitochondria. Additionally, comparisons of potential poration between mitochondrial membranes and the outer cell membrane were studied. As is shown in Figure 5b, mitochondrion has two irregular membranes: consisting of the inner and outer mitochondrial membranes.

Pulse generators can provide pulses with different rise/fall times, duration in the nanosecond range, and electric field amplitudes over tens of kV/cm. The transient

features of nanosecond pulses can be understood by considering the frequency spectrum which to a first order approximation can be defined in terms of two corner frequencies. The first corner frequency f_1 is determined by the pulse duration time τ_p as: $f_1 = 1/(\pi\tau_p)$, and the spectral response up to this frequency is roughly constant. Beyond this corner frequency, the spectrum decreases linearly with frequency on a Bode plot until the second corner frequency f_2 is reached, where $f_2 = 1/(\pi\tau_f)$ with τ_f being the fall time. For simplicity, here we consider the rise (τ_r) and fall (τ_f) times of the nanosecond pulses to be identical (i.e., $\tau_r = \tau_f$). Beyond the second corner frequency f_2 , the spectral response decreases with the square of the frequency. Reducing the rise and fall times, therefore, shifts the second corner frequency towards higher values, or alternatively adds to the high frequency components of the spectrum. The rise- and fall-time effects can be seen more clearly through the sample simulations shown in Figure 14. The figures show two assumed rectangular pulse shapes with $\tau_r = \tau_f = 15$ ns, and $\tau_r = \tau_f = 150$ ns, along with their corresponding Fourier components. Clearly, the shorter rise- and fall-time waveform retains larger magnitudes at the higher frequencies as compared to the corresponding components with the slower rise times.

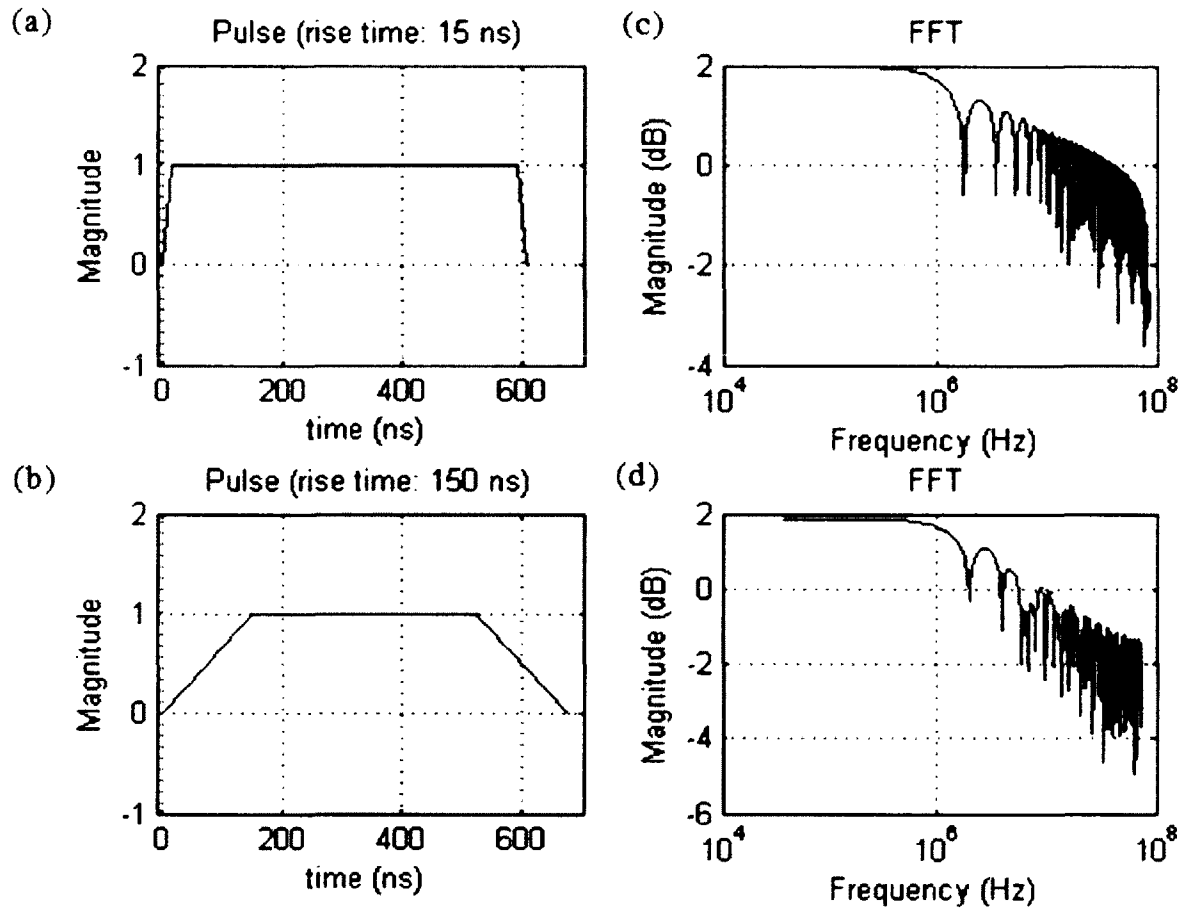


Figure 14. Two assumed rectangular pulses and corresponding Fourier spectra. (a) $\tau_r = \tau_f = 15$ ns, and (b) $\tau_r = \tau_f = 150$ ns; and the corresponding Fourier spectra for: (c) $\tau_r = \tau_f = 15$ ns, and (d) $\tau_r = \tau_f = 150$ ns cases.

(A) Differences Due to Rise/Fall-Times For Longer Pulses

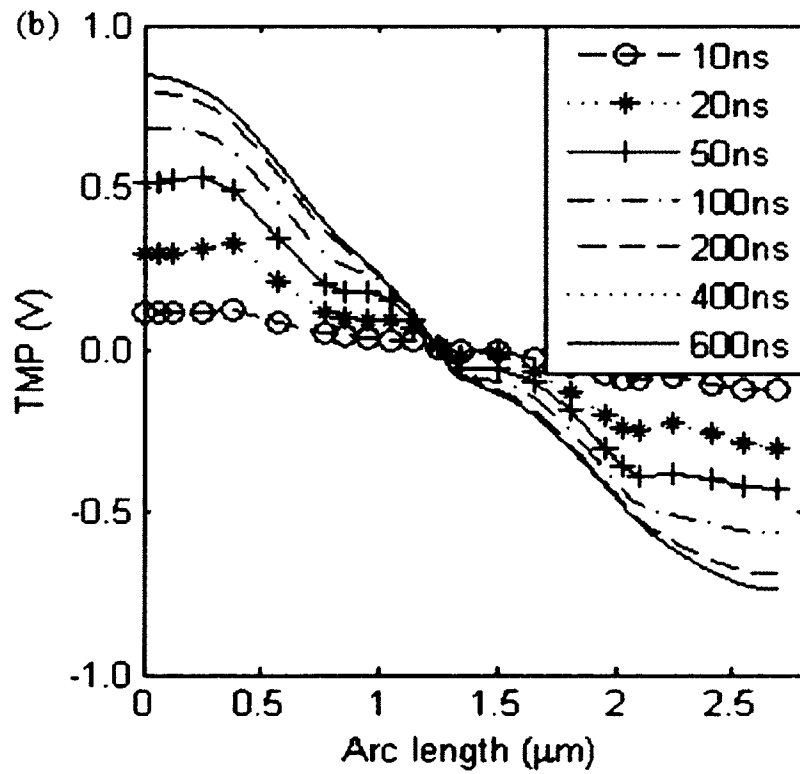
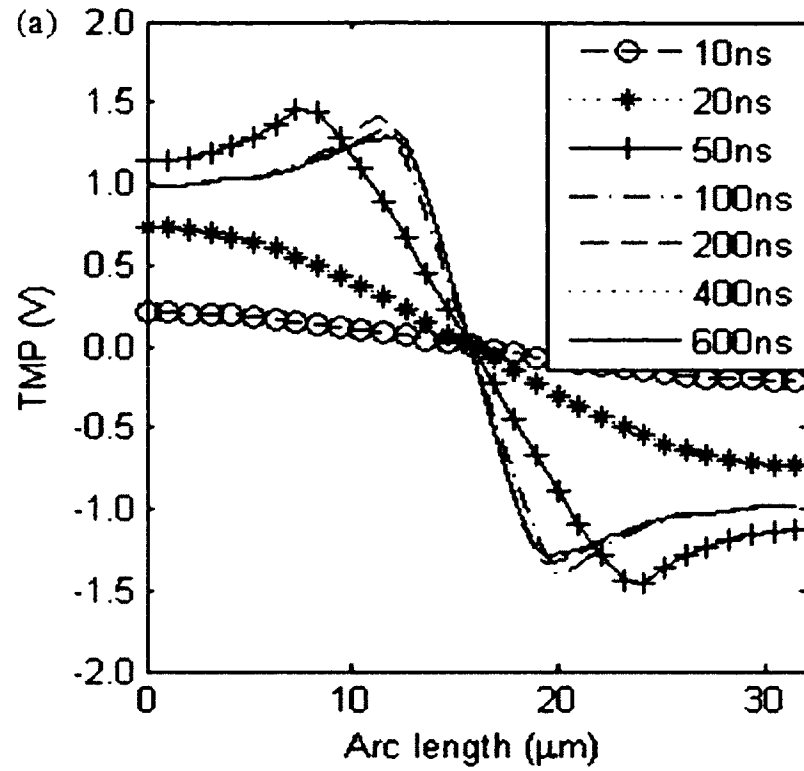
Snapshots of the TMP obtained for a 600 ns, 8 kV/cm pulse with short 15 ns rise/fall times are shown in Figure 15 for the plasma membrane, the outer mitochondrial membrane (OMM) and inner mitochondrial membrane (IMM), respectively, at different time instances. The highest values are predicted to be for the plasma membrane, with peak values in excess of 1 Volt, which is often taken as a convenient threshold for electroporation. In Figure 15a, the slight dip for small arc lengths (locations near the

polar cap) represents electroporation that has strongly increased the membrane conductance, thereby creating a relative “electrical short”. In Figure 15b, the TMP values are much lower for the OMM, and predicted to approach 1 V at the longest 600 ns instant at the poles. The arc length is also much lower than that of Figure 15a due to the smaller mitochondrial size. By contrast, the TMP values across the IMM in Figure 15c are significantly lower and exhibit undulations. These undulations can be understood by considering the mitochondrial geometry used here and shown in Figure 16. The points shown on the $t=600\text{ns}$ curve of Figure 15c correspond to the locations given in Figure 16.

While TMP values were obtained over numerous points on both the OMM and IMM, only some representative points have been marked in Figure 16, which shows the geometry chosen. The arc length for the IMM is much larger than that for the OMM due to the invaginations. Since the normal component of the applied electric field continually changes across the IMM surface, the TMP values generated display corresponding undulations.

Pore densities obtained from the above TMPs are given below in Figure 17. The highest values are for the plasma membrane as shown in Figure 17a. A gradual spread in the densities starting from the poles can be seen, and is expected since the highest normal electric fields occur in this region. The pore densities for the IMM (Figure 17c) are predicted to be 12-13 orders of magnitude smaller than that of the outer plasma membrane and hence, completely negligible. The sharp decrease arises from the exponential dependence of pore growth on the TMP values. Since the IMM has much lower membrane potentials as compared to that across the plasma membrane, the densities are expectedly much smaller.

Next for comparison, simulations for the same 600 ns pulse but with much longer rise/fall times of 150 ns were carried out. The values for most times were comparable to those obtained for the shorter 15ns rise/fall times. However, the only differences seen were for times between 50 ns and 200 ns. This is understandable, and associated with the slower 150 ns rise times. For example, Figure 18 shows the IMM pore densities for the 150 ns rise/fall time pulse at different times. Differences between the curves of Figure 18 and the corresponding plots of Figure 17c are mostly in the 50ns, 100ns and 200ns curves. At times much longer than 150 ns, the rise-time effects fade away.



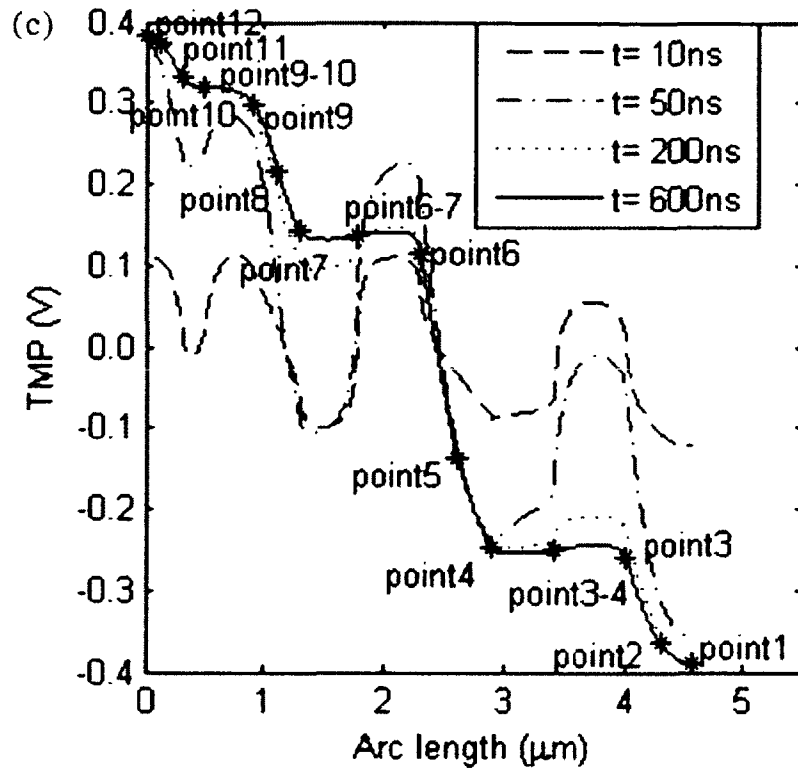


Figure 15. Simulation results obtained showing the TMP distribution over plasma membrane, OMM and IMM. (a) results obtained showing the TMP distribution over the semi-circular plasma membrane arc for a 600 ns, 8 kV/cm pulse with short rise/fall times of 15ns. (b) results showing the TMP over the OMM. (c) results showing the TMP over the IMM.

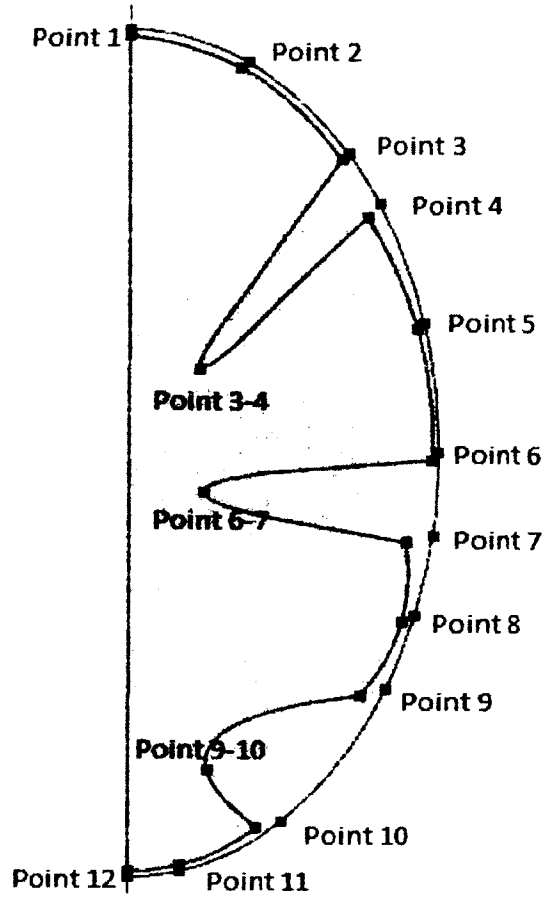
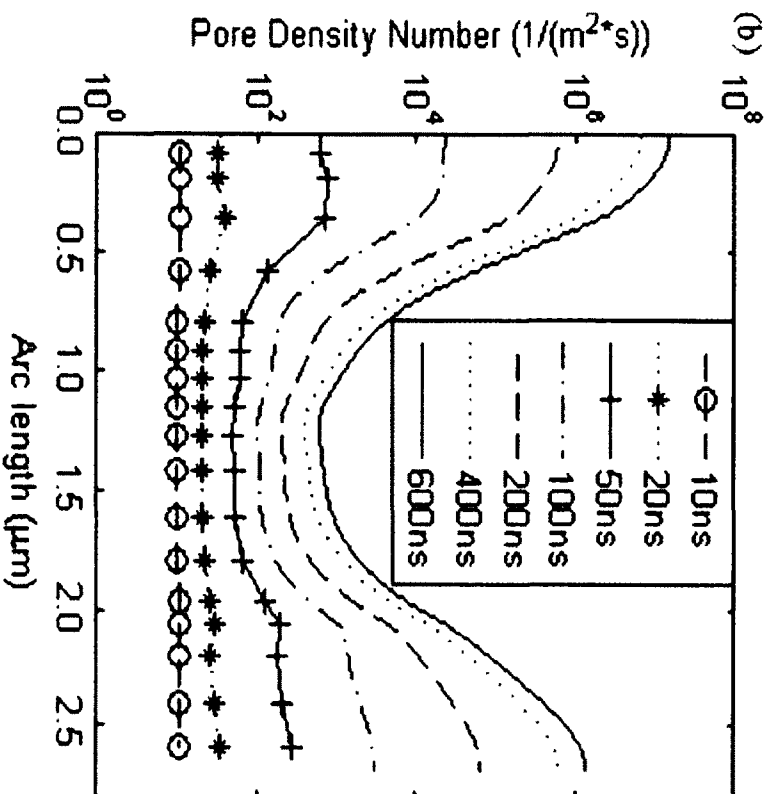
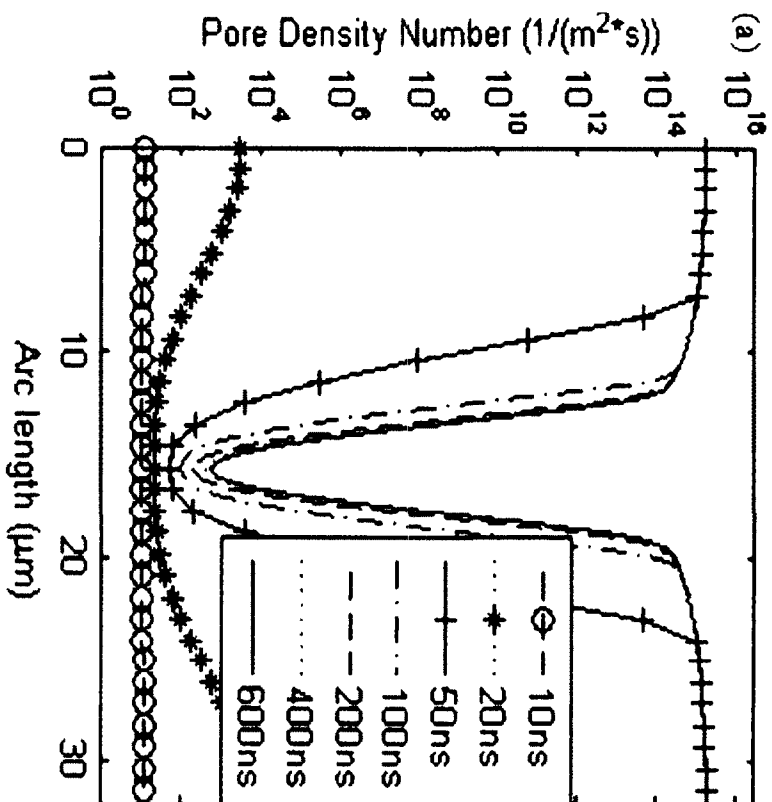


Figure 16. Geometry of the IMM and OMM chosen.



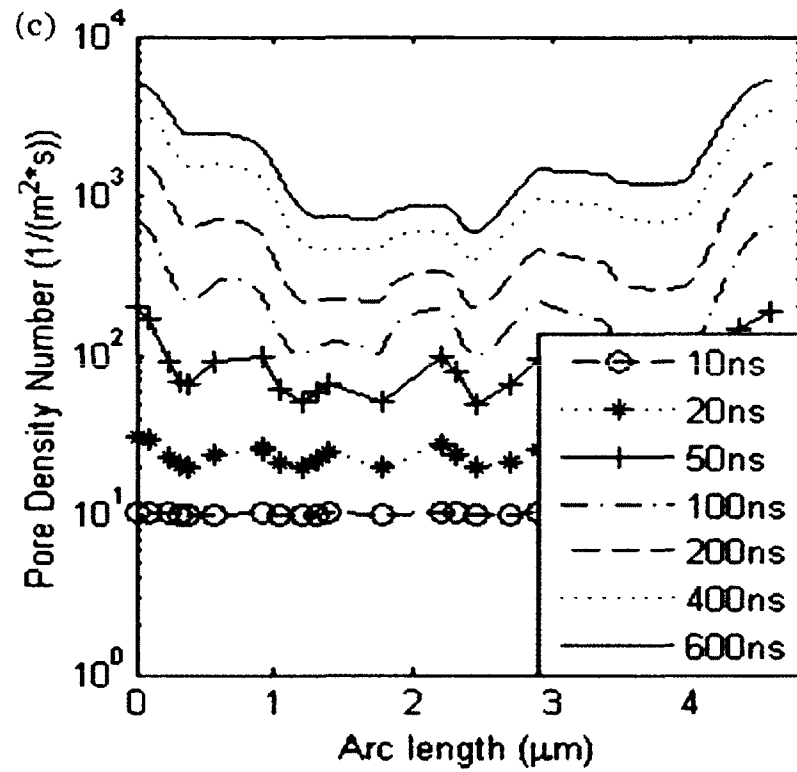


Figure 17. Simulation results obtained showing the pore density number over plasma membrane, OMM and IMM. (a) Results showing the plasma membrane pore density distribution. (b) Results showing the OMM pore density distribution. (c) Results showing the IMM pore density distribution.

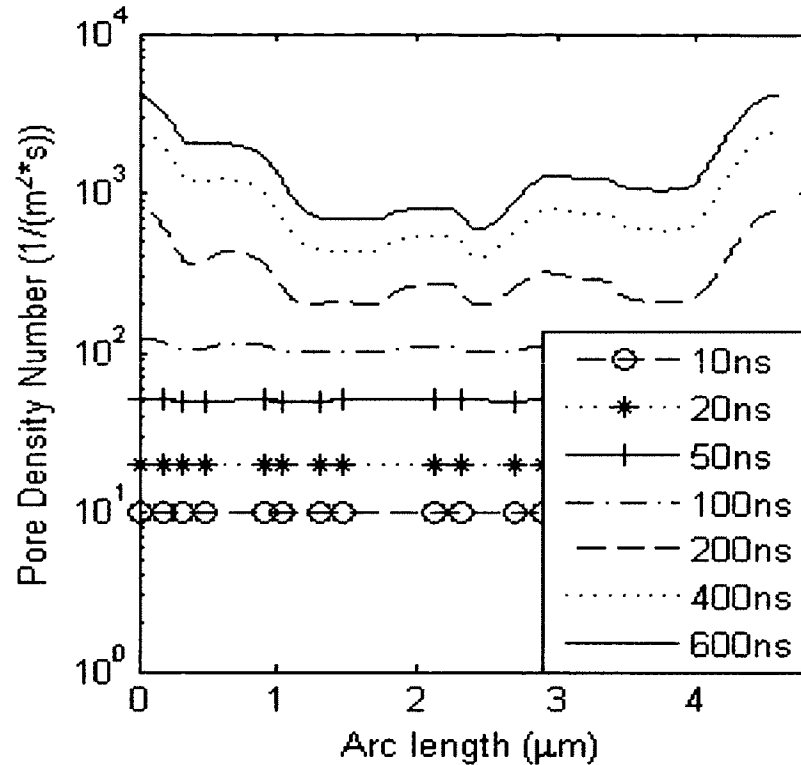


Figure 18. Predictions of the IMM pore density distribution with 150ns rise time.

(B) Differences Due to Electric Pulse Duration

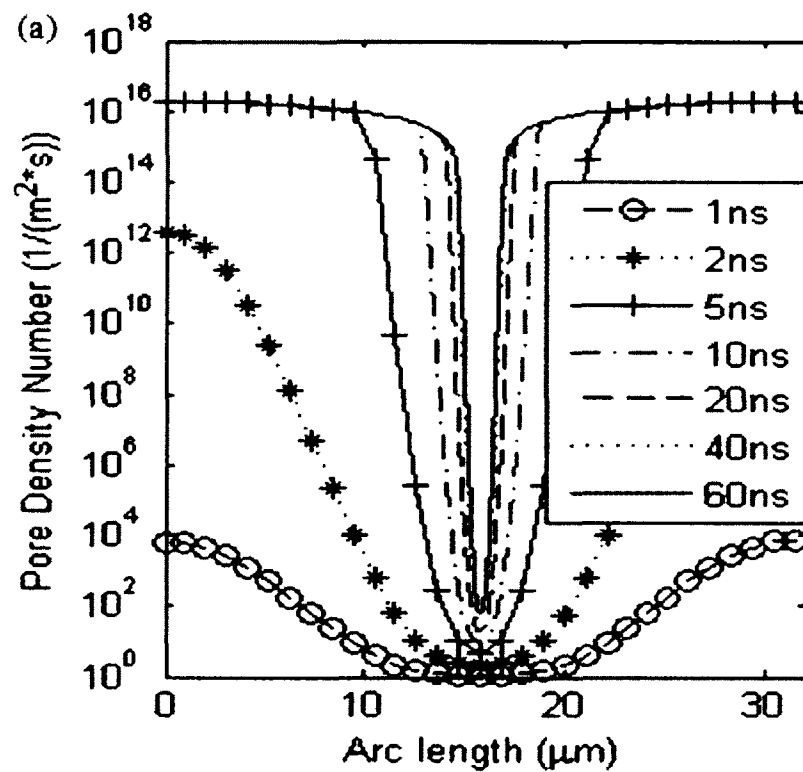
Next, simulations were carried out for a shorter 60 ns duration pulse with 1 ns rise/fall times. Since bio-effects are known to scale as the product of the field amplitude and the pulse duration[50], the peak electric field for these cases was adjusted to 80 kV/cm to maintain uniformity. Results of pore density distribution shown in Figure 19a reveal values and trends that are quite similar to that of Figure 17a for the longer pulse. The magnitudes were slightly larger though not by a significant amount. Pore densities for the mitochondrial membrane are shown in Figure 19b and Figure 19c. As compared to the longer 600 ns cases, the pore densities are predicted to be substantially higher. This clearly shows the ability of ultrashort pulses to penetrate the cells and affect the internal

organelles, though the results do show differences between the OMM and IMM responses. The profile for the OMM is similar to that of the plasma membrane, in that the largest pore densities occur at the two opposite poles, which develop the highest TMPs. Values at the equators are much lower, with a fairly smooth transition. This is expected given the spherical shapes of both structures. However, for the IMM, since the electric field component at the membrane fluctuates strongly with arc length, the TMP and hence the pore densities also fluctuate appreciably. In any case, the average number of pores and their sizes would be much smaller for the IMM than the OMM, at least over locations where the pore densities (and hence the TMP values) are low. As a rough estimate, the radii would be smaller than 0.5 nm, a value that had previously been predicted by our group for the outer plasma membrane [66].

The main tie-in of the present results is with a recent report [67] on potential mitochondrial effects from 600ns pulses. The following points emerge from the simulations: (i) for the longer 600ns pulses, the TMPs created across the mitochondrial membranes are quite small, and unlikely to lead to significant field-dependent poration effects: this appears to be true for both the longer and shorter rise/fall times. (ii) Poration at the plasma membrane are always much stronger than at the mitochondrial membranes. (iii) It is not as easy to porate the IMM as the OMM, and only some of the surface sites would develop a strong enough TMP. This is a geometric effect and hence a restrictive for strong field-dependent bio-effects.

Finally, since it has been shown that it is easier to porate the plasma membrane, it follows that inflow of calcium into cells is very likely, in keeping with the conjecture by Beebe et al. [67]. Such calcium influx can then conceivably affect calcium-dependent

mechanisms in the mitochondria, likely through the MPTP complex. Thus, cell-death or detrimental bio-effects may be possible even through longer pulse widths, even though the electrical pulse characteristics may not allow for efficient coupling to the mitochondria for strong poration. The calcium-mediated processes are then likely to be playing the role of second-messengers. There may also be other apoptotic-inducing pathways involving release of proteins at the mitochondria due to the TMP perturbations.



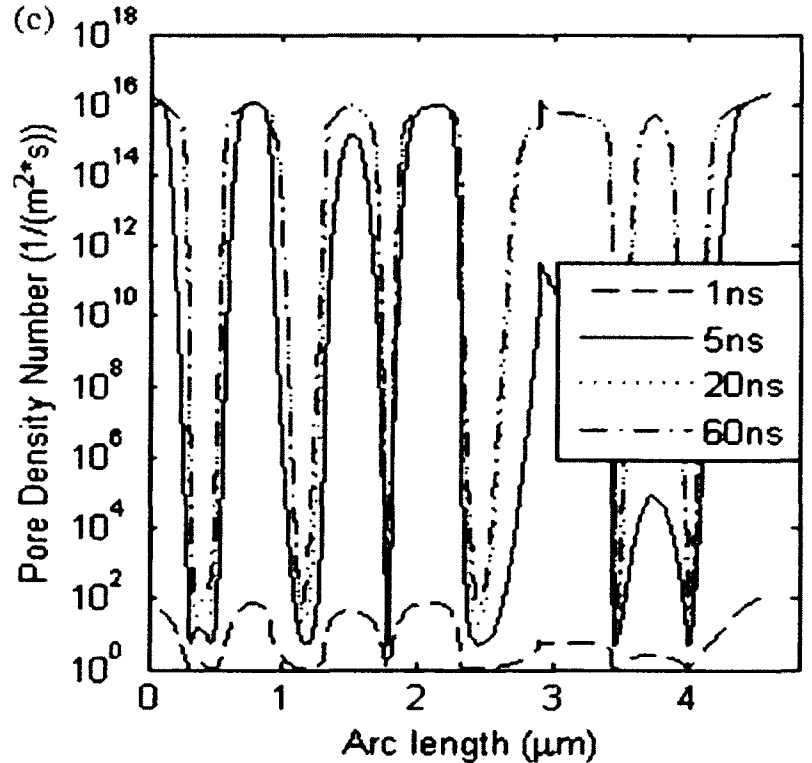
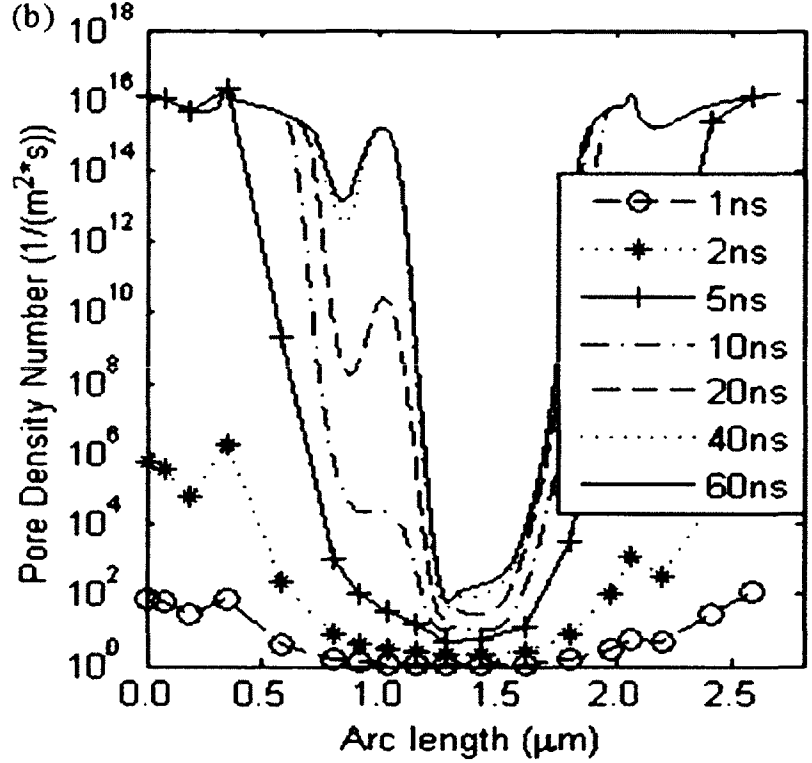


Figure 19. Predictions of pore density profile of plasma membrane, OMM and IMM for the 60ns pulse. (a) Plasma membrane pore density profile. (b) OMM pore density profile.(c) IMM pore density profile.

4.2 Simulation Results of PNP-NS Model

The PNP-NS model discussed in Chapter 3 was employed to calculate the ionic current through a pore with both a cylindrical and conical shape. Ion concentration profiles and ICR (ion current rectification) were particularly probed. Roles of the applied bias, the geometric asymmetry in the nanopore, as well as the charge distribution lining the membrane were also comprehensively studied and discussed through simulations.

4.2.1 Model Verification

Numerical results of electric potential by PNP and electroosmotic flow velocity by the PNS-NS model were compared with an analytical solution to ensure the validity and accuracy of numerical model.

The analytical method to calculate the electric potential along the axial direction (i.e., normal to charged surface) with ions in the medium was employed to validate the numerical method. The derivation is shown in Appendix III. In this particular case, common *KCl* electrolyte solution and a simplified one-dimensional problem is chosen. The analytical solution for the potential is shown below:

$$V(x) = \frac{4RT}{F} \operatorname{atanh} \left[\tanh \left(\frac{FV_s}{4RT} \right) \exp\left(-\frac{x}{L_D}\right) \right], \quad (4.4a)$$

$$c_i = C_{i0} \exp\left(-\frac{z_i F}{RT} V\right) \quad . \quad (4.4b)$$

where x is the distance from the charged surface, Debye length $L_D = \sqrt{\frac{\epsilon RT}{2F^2 C_0}}$, C_{i0} is solvent concentration, and V_s is the Zeta potential.

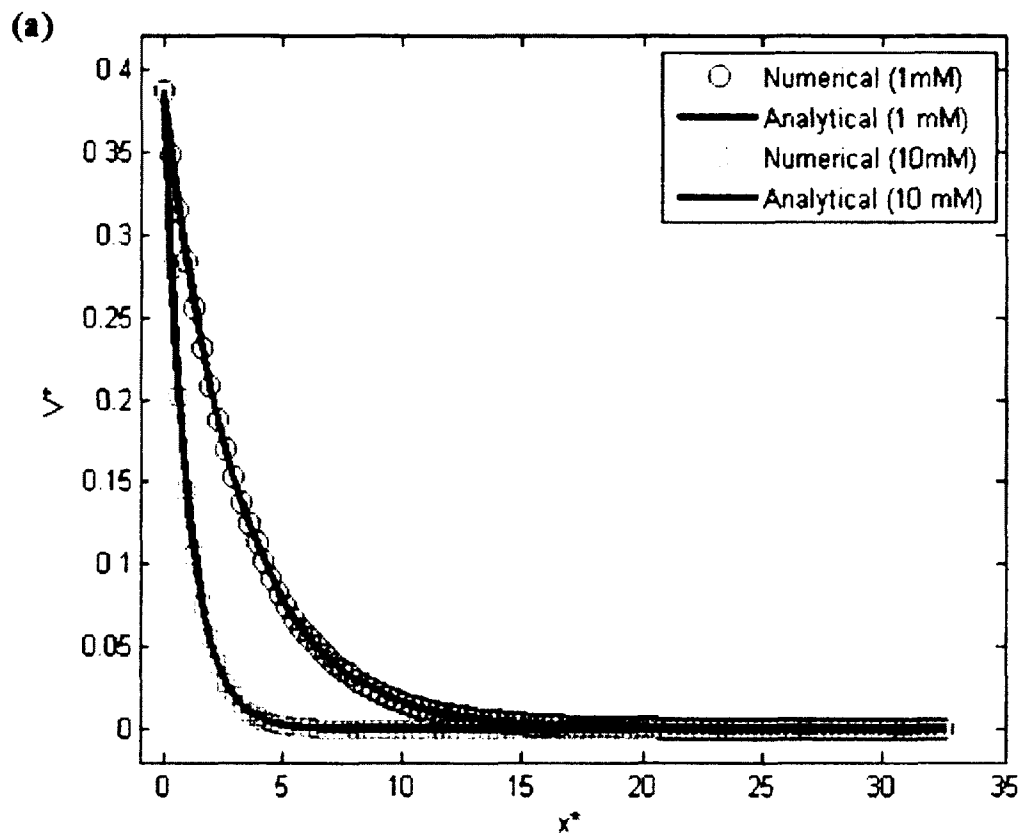
The parameters used in the model are shown in Table 4.

Table 4. Parameters used in the PNP model verification.

Symbol	Value	Description
z_1	1	Valence of K^+
z_2	-1	Valence of Cl^-
D_1	$1.957 \times 10^{-9} [m^2/s]$	Diffusivity of K^+
D_2	$2.032 \times 10^{-9} [m^2/s]$	Diffusivity of Cl^-
R	$8.31 [J/mol/K]$	Universal gas constant
F	$9.649 \times 10^4 [C/mol]$	Faraday constant
T	300[K]	Temperature
ϵ	$80\epsilon_0$	Permittivity
V_s	10[mV]	Zeta potential
C_0	$1 [mol/m^3]$ or $10 [mol/m^3]$	Bulk concentration

The common electrolyte *KCl* with bulk concentrations of 1 mM and 10 mM were used in the PNP model. As is shown in Figure 20, a good agreement between the numerical results and analytical solutions with regards to the electric potential is reached. Also, the ion concentration along the axial direction were compared between the numerical and analytical solutions, which also yield a mutually good agreement. Through the validation of electric potential and ion concentration, which are two variables in the set of governing

equations that the solver is dedicated to resolve, the accuracy of the PNP model was guaranteed.



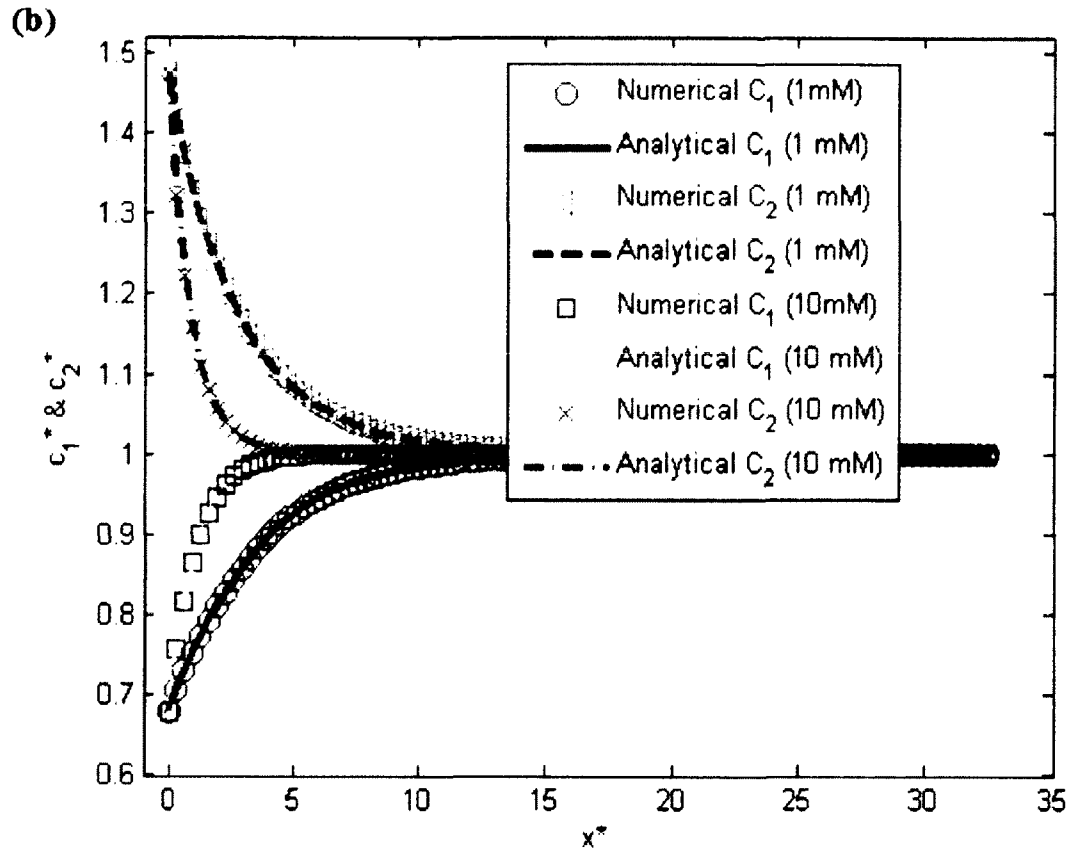


Figure 20. Distribution of electric potential and ionic concentration. (a) Distribution of electric potential near a charged planar surface under different bulk concentrations. (b) Distribution of ionic concentrations near a charged planar surface under different bulk concentrations.

The PNP-NS model was verified in a two-dimensional (2D) axially-symmetric cylindrical tube, as shown in Figure 21. The fluid velocity in Z direction was compared between the analytical method and the numerical model. The analytical expressions for the fluid velocity along the cylindrical tube in z direction is given as [68]:

$$v_z(r) = -\frac{L_D \sigma E}{\mu I_1\left(\frac{L_\infty}{L_D}\right)} \left[I_0\left(\frac{L_\infty}{L_D}\right) - I_0\left(\frac{r}{L_D}\right) \right] \quad (4.5)$$

where E is the electric field in Z direction, μ is viscosity, and I_i is the modified Bessel functions of the first kind of order i .

Table 5. Parameters used in the PNP-NS model verification.

Symbol	Value	Description
μ	0.001[Pa · s]	Viscosity
σ	-0.001[C/m ²]	Surface charge density
D_1	1.957x10 ⁻⁹ [m ² /s]	Diffusivity of K ⁺
D_2	2.032x10 ⁻⁹ [m ² /s]	Diffusivity of Cl ⁻
R	8.31[J/mol/K]	Universal gas constant
F	9.649x10 ⁴ [C/mol]	Faraday constant
T	300[K]	Temperature
ϵ	80 ϵ_0	Permittivity
E	50[kV/cm]	Electric field
C_0	10[mol/m ³]	Bulk concentration

The common electrolyte *KCl* with bulk concentration of 10 mM was used in the PNP-NS model. All the parameters of PNP-NS model are shown in Table 5. The results are shown in Figure 21. A good agreement between the numerical results and analytical

solutions on electroosmotic flow in Z -direction was indicated. The validation of fluid flow velocity in the nanotube ensured the accuracy of the PNP-NS model.

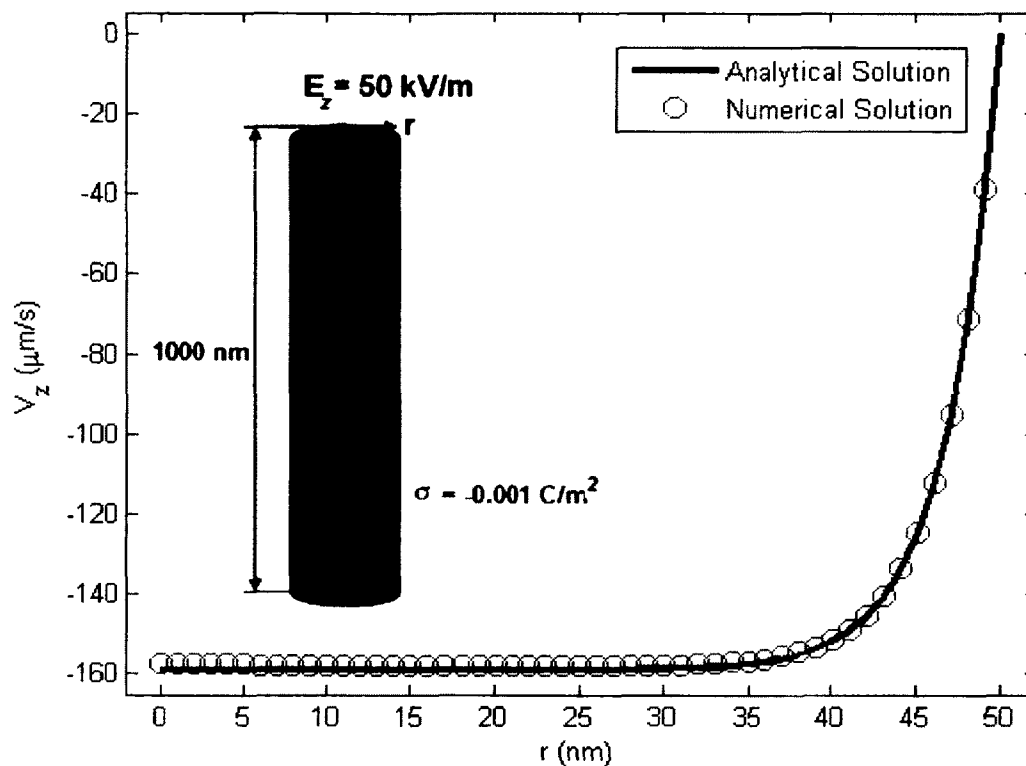


Figure 21. Electroosmotic flow velocity in a cylindrical nanotube.

4.2.2 Simulation Results

4.2.2.1. Ion Profile

Ion profiles (cation K^+ and anion Cl^-) were shown to better understand the ions distribution in the nanopore. The dimensionless concentration of both ions, shown in Figure 22, were examined near the tip of the conical nanopore (shown in Figure 6), under the conditions: an electric field 9.5 kV/cm with direction from the end of nanopore to the

tip, the surface charge density -0.05 C/m^2 , the bulk concentration 3.8 mol/m^3 , and Debye length equal to the tip radius.

Figure 22a reveals that the nanopore is predominantly filled with the cations, especially on the wall due to the negative charged surface, while the anions are significantly inhibited in the nanopore, as indicated in Figure 22b. The concentrations profiles for K^+ and Cl^- ions are shown in these figures. The applied voltage was -1 V applied to the upper surface of the figures, with the bottom surface at ground potential. As can be seen from the figures, the concentrations are not the same for the entire zone. The region around the tip attracts more K^+ ions and repels Cl^- ions resulting from the electric field and attractive/repulsive force between fixed surface charges and bulk ions.

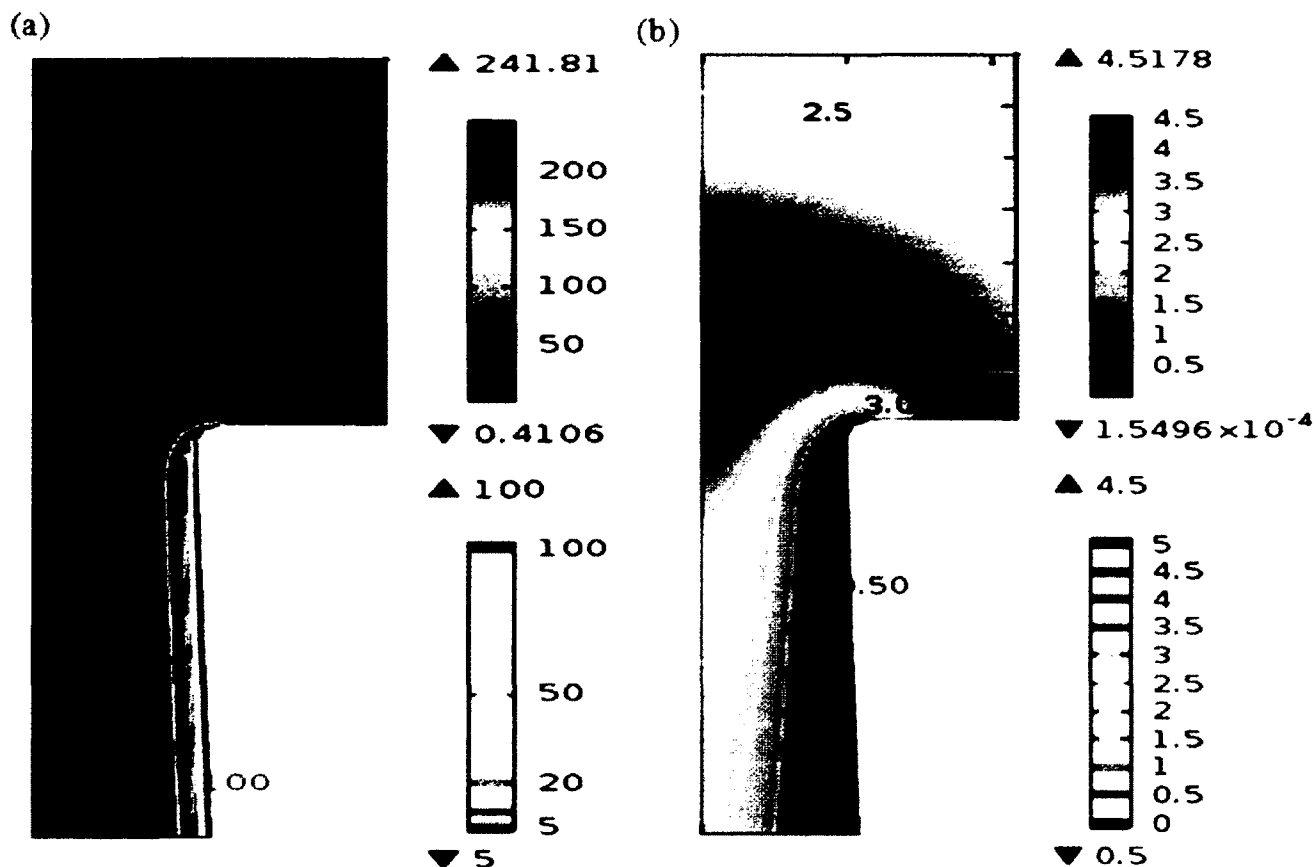


Figure 22. Distribution of dimensionless concentration of cation and anion near the tip of the conical nanopore. (a) K^+ distribution. (b) Cl^- distribution.

4.2.2.2. Current-Voltage Characteristics in a Nanopore

In this part, in keeping with actual experiments, an aqueous medium with a pH of 7.2, consisting of 140 mM of Cs-acetate, HEPES [(4-(2-hydroxyethyl)-1-piperazineethanesulfonic acid)] and ethylene glycol tetraacetic acid (EGTA), was used on either side of the bio-membrane. Of these, HEPES is an organic chemical buffering agent widely used in cell cultures because it is good at maintaining physiological pH of solutions despite changes in carbon dioxide concentration produced by cellular

respiration. EGTA is a chelating agent possible of calcium ions, and is useful for buffer solutions that resemble the environment in living cells. Both HEPES and EGTA played no role in the ionic flow and were not considered in the calculations.

Thus, both ions, Cs^+ and Acetate^- , were used in the present simulations. The various parameters are given in Table 2.

Table 6. Various values of the radii R_l and R_r chosen for I - V simulations.

R_l (nm)	R_r (nm)	Ratio $R = R_r/R_l$
0.78	0.78	1.0
0.78	1.17	1.5
0.78	1.56	2.0
0.78	1.95	2.5

(A) Role of the Radius Ratio

The first set of simulations for the I - V characteristics through the nanopore varied the radii R_l and R_r at the two ends. In electroporated cellular membranes, the pore radii are known to be small and typically less than 1 nm. Hence, the different combinations of values were chosen to lie in this range, while being at least as large as the Debye length, and are listed in Table 6. The simulation results obtained are shown in Figure 23 for different values of the ratio $R = R_l/R_r$. For all the four curves, the left radius was kept constant at 0.78 nm, while the radius of the opening on the right side was changed.

Arguably there are numerous other combinations for R_l and R_r , and these values represent a sample set. Not surprisingly, values of the current in Figure 23 are predicted to be higher for the larger R_r due to the larger pore opening. However, despite the conical nature of the nanopore (for $R = 1.5, 2.0, 2.5$), the $I-V$ characteristics all turn out to be almost linear. This result differs from the nonlinearity reported from pores in artificial membranes, but it should be realized that synthetic channels typically have thicknesses in the micron range. Due to the ultrashort longitudinal dimensions here, electric field perturbations and deviations due to geometry are minimized, and the voltage drop across the pore can essentially be linearized. Thus the influence of geometry alone on potential nonlinearities in the $I-V$ characteristics in biological membranes is seen to be relatively insignificant.

(B) Role of Surface Charge Density

The role of a uniform charge lining the pore walls was examined next, and the corresponding results are shown in Figure 24. Three different values of $+0.01 \text{ C/m}^2$, -0.01 C/m^2 and -0.02 C/m^2 were used for the surface charge density for a cylindrical nanopore with $R_l = R_r = 1.0 \text{ nm}$. The charge density values chosen lie in the range that has been reported in the literature [69]. The experimental data (some of which was reported in Ref. [36]) is also shown in Figure 24, though the nanopore radii in the experiments is unknown. Basically, the experimental data was obtained in the steady-state from patch clamp experiments [36].

In Figure 24, a slight asymmetry can be seen in the simulation results, though it is almost negligible. In addition, the highest currents were predicted to increase as the

surface charge became more negative. This is not surprising since a negative surface would tend to attract cations and promote their transport. Since the cations in this case (Cs^+) have a larger permeability than the acetate, the negative pore charge produced larger currents. More importantly, two other points emerge from a comparison with the experimental data curve: (i) First, the deviation between the prediction and the data seems to increase with the magnitude of the applied bias, and (ii) the curvature of the experimental points appears to be contrary to that of the simulation predictions. For example, while a saturating trend seems to be present in the numerical results, the experimental data is indicative of stronger nonlinear enhancements in current with increases in the applied voltage magnitude. Most of the I - V characteristics reported in the literature on synthetic membranes do not exhibit the nonlinear increases or the curvature seen in the present data.

Next, the role of spatial nonuniformity in the charge distribution lining the pore walls was investigated, based on a conical pore with $R_l = 0.78$ nm, $R_r = 1.5$ nm, and the right end taken to be grounded. Charges were assigned over the left and right portions of the pore over a distance of 1.5 nm each. The central 2 nm region of the 5 nm pore channel was left uncharged. A bias-dependent charge distribution was implemented based on the following argument. For a positive bias at the left end, negative mobile charges would tend to flow to the left side which is tapered and has a progressively smaller radius. Consequently, there would be crowding of negative charges in this region, and a greater probability of binding to the membrane molecules. Under the latter scenario, the net negative charge lining the tapered left region would be enhanced. Conversely with a negative bias applied to the left end, cations would flow to the left. These could then

similarly attach or screen the negative moieties; resulting in reductions in the negative charge density.

The bias dependent effect discussed above was implemented in the following manner. A constant charge density of -0.01 C/m^2 was assigned over the rightmost 1.5 nm region starting from the pore mouth. However, for the left side of the channel, the charge density was varied with bias. A value of -0.005 C/m^2 was used over a 1.5 nm distance starting from the left end of the pore for a negative bias, while a value of -0.015 C/m^2 was used over the same 1.5 nm distance starting from the left end for a positive bias. This distribution effectively amounted to a more negative charge above the average -0.01 C/m^2 value on the left side for a positive voltage at the left end, and a reduction in negative charge at the left end for a negative bias in the same region. The calculated $I-V$ response of the nanopore is shown in Figure 25 along with the experimental data. Though the predictions of Figure 25 seem to better track the experimental data, a widening discrepancy can be seen between the two curves of Figure 25 at higher voltage magnitudes.

(C) Pore Radius Dynamic Development

In order to better match the data, simulations were next carried out in which the left pore radius was taken as an adjustable parameter and allowed to change with the magnitude of the applied voltage. The basic notion behind such a bias-dependent radial change is that a higher incident ionic flux with increasing voltage magnitude could work to exert higher forces on the tapered walls of a nanopore, thereby causing reversible local expansion. In keeping with this, the radius of the pore opening on the left was increased

with the voltage magnitude from its initial value of 0.78 nm, while the larger pore on the right was maintained at the 1.5 nm size. With bias dependent adjustments made to the R_l value, the results obtained for fitting the data trend are shown in Table 7. A curve-fit to the voltage dependent pore-radius R_l shown in Figure 26, seems to roughly have a quadratic trend. The pore radius $R_l(V)$ in nanometers as a function of the applied bias (V) in volts was extracted to be: $R_l(V) = [32 V^2 - 2.9 V + 0.84]$ nm. This would qualitatively be in keeping with a hypothesis that deformations at the narrow tapered end depend on the amount of energy dissipated by the incident ionic flux. The latter is expected to scale as the square of the applied bias in the linear response regime. Thus, quite plausibly, the nonlinearity seen in the experiments on the nanoscale biological pores arises due to deformations in the elastic bio-membrane. From the standpoint of momentum transfer, a higher ion flux with increasing voltage would work to produce a higher force on the tapered walls of a nanopore as sketched in Figure 27. This figure shows incident cations could effectively broaden the narrow neck at the bottom of the pore. For the opposite polarity, the anions would have the same effect. This would tend to expand the local pore radius, a more significant prospect in biological membranes that typically have weaker elastic constants than artificial, inorganic membranes. From an alternative viewpoint, a larger ionic current at the higher voltages in bio-membranes would lead to higher dissipation at the tapered ends, leading to slight changes in the local temperature. Since the fluidity of biomembranes is very sensitive to temperature changes, the net effect can be expected to be local pore expansion. Moreover, the crowding of ions at the tapered end would in itself generate local perturbative electric fields that are known to be drivers for pore creation and expansion. Furthermore, it must be noted that the present results are

not meant to be definite in terms of a quantitative analyses, since other sets of values for the pore wall charge densities, its distribution, radii for the conical pore, and voltage-dependent pore dilations could also have compared well with the experimental data.

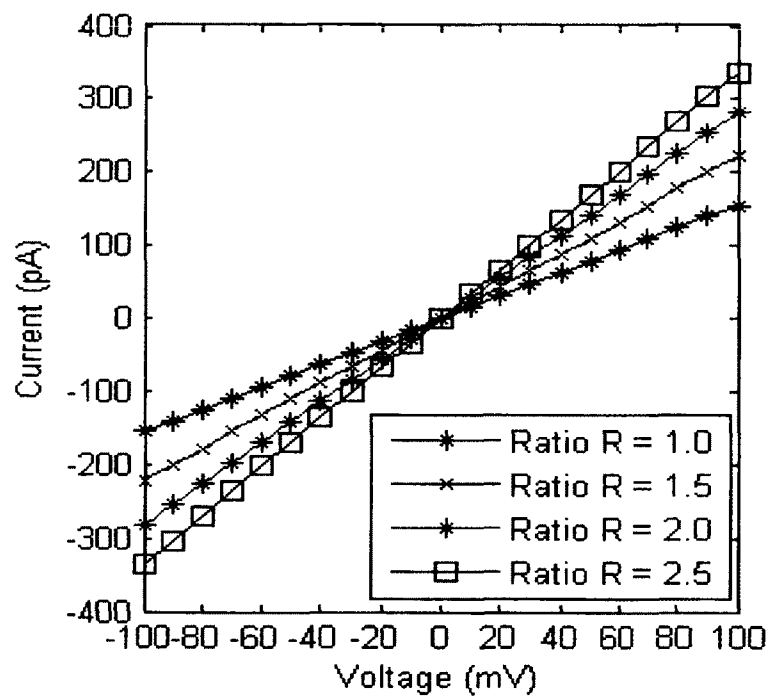


Figure 23. Simulation results showing the current-voltage characteristics for different aspect ratios R through a 5 nm uncharged nanopore.

Table 7. Values of left pore radius adjusted as a function of the magnitude of applied bias.

Voltage (mV)	R_l [nm]
-100	1.46
-90	1.39
-80	1.23
-70	1.16
-60	1.1
-50	1.0
-40	1.05
-30	1.09
-20	0.95
+90	0.818
+100	0.9

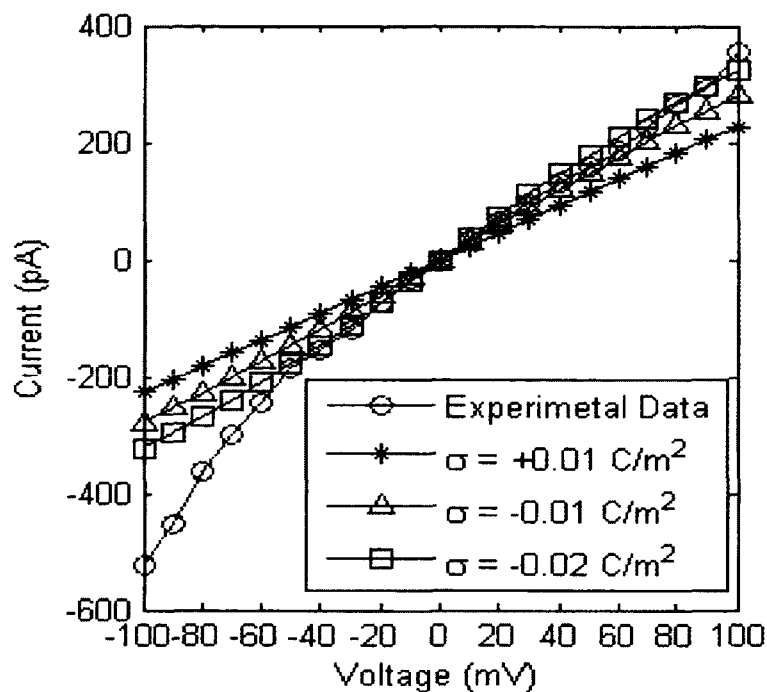


Figure 24. Simulation results showing the current-voltage characteristics for different surface charge densities of $+0.01 \text{ C/m}^2$, -0.01 C/m^2 and -0.02 C/m^2 through a 5 nm cylindrical nanopore with $R_l = R_r = 1.0 \text{ nm}$. The experimental data is also shown.

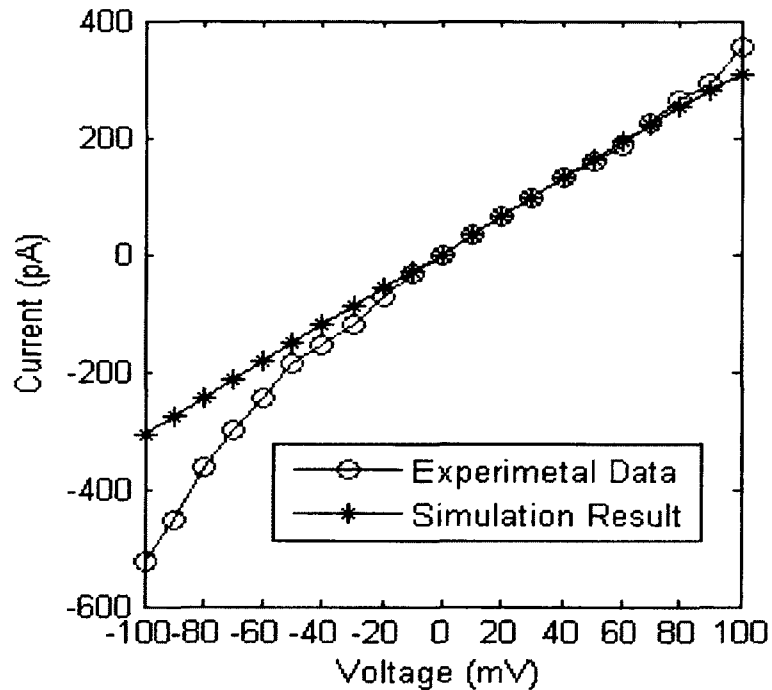


Figure 25. Results for the I - V response for a nonuniform pore surface charge distribution lining the pore walls. A conical pore was assumed with $R_l = 0.78 \text{ nm}$ and $R_r = 1.5 \text{ nm}$.

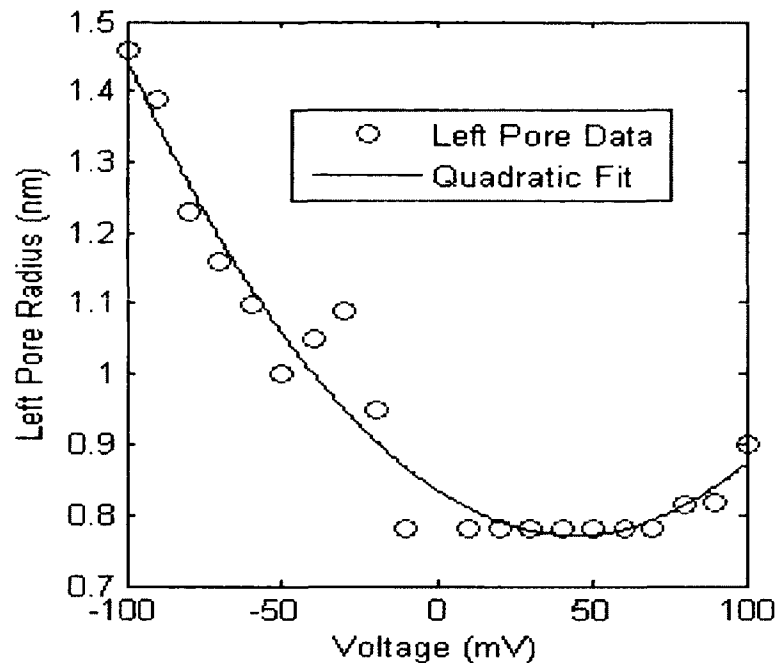


Figure 26. Voltage dependent values of the left pore radius R_l extracted from comparisons with experimental data.

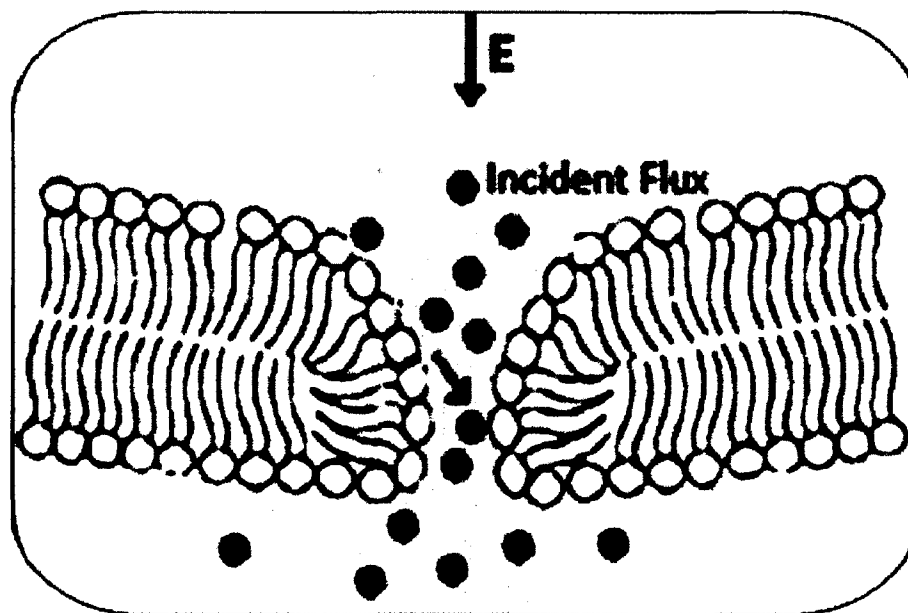


Figure 27. Hypothetical sketch of a conical nanopore. For clarity, water molecules, membrane proteins, and details of the phospholipid molecules are omitted. The incidence of either anions or cations (depending on the polarity) on the tapered end could work to enlarge the local radius at the narrow end. Here incident cations are shown to effectively broaden the narrow neck at the bottom of the pore.

CHAPTER 5

CONCLUSIONS AND FUTURE RESEARCH

5.1 Research Summary

The electroporation model in this work was quantitatively used to evaluate the possibility of drug release of liposomes, and to explore the bio-effects across mitochondrial membranes of irregular shape by high-amplitude electric field with nanosecond pulses. The electrical property of cells was probed through parametric analyses in order for optimized electroporation of liposomes. The results indicate that liposomes with a larger radius, higher conductivity and lower membrane permittivity could be favorably electroporated and have higher selectivity to shorter electric pulses with a smaller risk for damaging other intracellular organelles and the cell itself. Based on our calculations, we can conclude that with proper cell electrical property, nanosecond pulses have the potential to be used as a tool for controlled drug release from intracellular liposomes. Longer pulses with smaller electric fields could be used for conventional electroporation and transport, while the short-pulses at higher electric fields could cause rupture and internal drug release.

The results also demonstrate that short, high-intensity nanosecond pulses would indeed penetrate cellular organelles and have the capacity to create membrane potentials, while longer pulses are not as effective in generating TMPs at organelles. Also, the plasma membrane effects are always greater than those at the mitochondria, and that poration at the IMM is more difficult than at the OMM. Electric fields need to be high to create pores in mitochondrial membranes, though the pulse can be as short as a few nanoseconds. Also, in the shorter pulse range, the dependence of pore density on

geometry is very pronounced. That could mean short pulses could be more effective in some highly irregular shaped cells, such as neurons, with interesting results if extended to picosecond pulsed stimulation.

The PNP-NS model of this work was quantitatively employed to explain the ionic transport through biological nanopores. The coupled Nernst-Planck equations were for ionic concentrations, the Poisson equation for the electric potential, and the Navier-Stokes equations for fluid flow in the simulations. Roles of the applied bias, the geometric asymmetry in the nanopore, as well as the charge distribution lining the membrane were all examined. Effects of the various aspects were probed individually by obtaining the current-voltage characteristics, and comparing the results against experimental data obtained from patch-clamp measurements. The results are indicative of a bias-dependent expansion of local pore radius, possibly arising from the enhanced flux of incident ions on the membrane walls, along with other possible factors.

However, it must be pointed out that since nanopores are very small (of $\sim 1-2$ nm radius), they cannot be directly observed. Hence, only indirect effects and consequences can be seen experimentally, and include tangible effects such as current flow and increases in conductivity. Furthermore, some of these effects depend on events and processes that are initiated and set in motion by nanoporation. For example, changes in conductivity can only be measured only when fluids/ions begin to flow through membrane pores. So while pores themselves can be created quickly, the transport and flow that then needs to be recorded to experimental data is a delayed event. Thus, given this absence of direct experimental correlation with nanoporation, it is impossible to directly validate simulation results of electroporation times with observed data. At best,

one can only compare simulation results with other simulation results such as reports that are based on Molecular Dynamics (MD) simulation techniques [70, 71]. MD has the capability to explore the cell membrane in the perspective of molecules and ions, which can predict the complicated electropores formation in an alternative way with atomistic details taken into account. Here, our approach is roughly comparable with the MD predictions of electroporation with regards to the transmembrane potentials and pore formation times.

5.2 Future Work

More modeling and simulation work combined with experimentation can be carried out to explore the inherent biophysics in cells due to the application of the high-intensity electric pulses on the level of the nanosecond.

Based on the research work described in this dissertation, some of the other areas for future research are briefly described in the following, and could be:

(i) A three-dimensional (3D) model of cells with their internal organelles could be constructed. More realistic cell presentation with intracellular organelles (e.g. the complicated Endoplasmic Reticulum shape) could be included in the electroporation model.

(ii) Conduct Molecular Dynamic calculations of ionic transport in nanopores for a given set of molecular structures and arrangements in the presence of applied electric pulsing.

(iii) Include multiple-pulsing scenarios and temperature impacts in the model. Temperature changes might make a difference in the ion movement in the nanopore and ions release by intracellular organelles.

(iv) Simulate multiple (or at least two adjacent) pores to probe possible mutual coupling effects, and the role of induced electric fields in one neighborhood due to the presence of ions in a nearby neighborhood.

REFERENCES

- [1] R. Staempfli, "Reversible breakdown of the excitable membrane of a ranvier node," *An. Acad. Brasil. Ciens.*, vol. 30, pp. 57-63, 1958.
- [2] T. Y. Tsong, "Electroporation of cell membranes," *Biophysical Journal*, vol. 60, pp. 297-306, 1991.
- [3] J. C. Weaver and Y. A. Chizmadzhev, "Theory of electroporation: A review," *Bioelectrochemistry and Bioenergetics*, vol. 41, pp. 135-160, 1996.
- [4] I. G. Abidor, V. B. Arakelyan, L. V. Chernomordik, Y. A. Chizmadzhev, V. F. Pastushenko, and M. P. Tarasevich, "Electric breakdown of bilayer lipid membranes: I. The main experimental facts and their qualitative discussion," *Journal of Electroanalytical Chemistry and Interfacial Electrochemistry*, vol. 104, pp. 37-52, 1979.
- [5] R. P. Joshi and K. H. Schoenbach, "Bioelectric Effects of Intense, Ultrashort Electric Pulses," *Critical Reviews in Bio-Medical Engineering*, vol. 38, pp. 255-304, 2010.
- [6] R. P. Joshi and K. H. Schoenbach, "Electric Fields in Biological Cell and Membranes," in *Electromagnetic Fields in Biological Systems*, Boca Raton, FL: CRC Press, 2011.
- [7] G. A. Hofmann, S. B. Dev, S. Dimmer, and G. S. Nanda, "Electroporation therapy: a new approach for the treatment of head and neck cancer," *IEEE Transactions on Biomedical Engineering*, vol. 46, pp. 752-759, 1999.
- [8] D. C. Chang, B. M. Chassy, J. A. Saunders, and A. E. Sowers, "Guide to electroporation and electrofusion," *New York: Academic Press*, 1992.
- [9] E. Neumann, Arthur E. Sowers, and Carol A. Jordan, "Electroporation and electrofusion in cell biology," *Springer*, 1989.
- [10] S. Orłowski and L. M. Mir, "Cell eletro-permeabilization: a new tool for biochemical and pharmacological studies," *Biochim Biophys Acta*, vol. 1154, pp. 51-63, 1993.
- [11] J. C. Weaver, "Electroporation : a general phenomena for manipulating cells and tissues," *Journal of Cellular Biochemistry*, vol. 51, pp. 426-435, 1993.
- [12] K. H. Schoenbach, R. P. Joshi, J. F. Kolb, C. Nianyong, M. Stacey, P. F. Blackmore, *et al.*, "Ultrashort electrical pulses open a new gateway into biological cells," *Proceedings of the IEEE*, vol. 92, pp. 1122-1137, 2004.
- [13] K. C. Melikov, V. A. Frolov, A. Shcherbakov, A. V. Samsonov, Y. A. Chizmadzhev, and L. V. Chernomordik, "Voltage-induced nonconductive pre-pores and metastable single pores in unmodified planar lipid bilayer," *Biophys. J.*, vol. 80, pp. 1829-1836, 2001.
- [14] V. Zlatko, A. T. Esser, T. R. Gowrishankar, and J. C. Weaver, "Membrane electroporation: The absolute rate equation and nanosecond time scale pore creation," *Phys. Rev. E*, vol. 74, pp. 021904/1-12, 2006.
- [15] N. Chen, K. H. Schoenbach, J. F. Kolb, R. J. Swanson, A. L. Garner, J. Yang, *et al.*, "Leukemic cell intracellular responses to nanosecond electric fields," *Biochem. Biophys. Res. Comm.*, vol. 317, pp. 421-427, 2004.
- [16] P. T. Vernier, Y. Sun, L. Marcu, S. Salemi, C. M. Craft, and M. A. Gundersen, "Calcium bursts induced by nanosecond electric pulses," *Biochemical and Biophysical Research Communications*, vol. 310, pp. 286-295, 10/17/ 2003.

- [17] S. J. Beebe, P. F. Blackmore, J. White, R. P. Joshi, and K. H. Schoenbach, "Nanosecond pulsed electric fields modulate cell function through intracellular signal transduction mechanisms," *Physiol. Meas.*, vol. 25, p. 1077, 2004.
- [18] R. P. Joshi, A. Nguyen, V. Sridhara, Q. Hu, R. Nuccitelli, and K. Schoenbach, "Simulations of intra-cellular calcium release dynamics in response to a high-intensity, ultra-short electric pulse," *Phys. Rev. E*, vol. 75, pp. 041920/1-041920/10, 2007.
- [19] A. J. H. Sale and W. A. Hamilton, "Effects of high electric fields on microorganisms," *Biochimica et Biophysica Acta.*, vol. 148, pp. 781-800, 1967.
- [20] K. H. Schoenbach, R. P. Joshi, R. H. Stark, F. C. Dobbs, and S. J. Beebe, "Bacterial decontamination of liquids with pulsed electric fields " *IEEE Transactions on Dielectrics and Electrical Insulation*, vol. 7, pp. 637-645, 2000.
- [21] R. Nuccitelli, U. Pliquett, X. Chen, W. Ford, J. R. Swanson, S. J. Beebe, *et al.*, "Nanosecond pulsed electric fields cause melanomas to self-destruct," *Biochem. Biophys. Res. Commun.*, vol. 343, pp. 351-360, 2006.
- [22] M. Stacey, J. Stickley, P. Fox, V. Statler, K. Schoenbach, S. J. Beebe, *et al.*, "Differential effects in cells exposed to ultra-short, high intensity electric fields: cell survival, DNA damage, and cell cycle analysis," *Mutation Research/Genetic Toxicology and Environmental Mutagenesis*, vol. 542, pp. 65-75, 12/9/ 2003.
- [23] K. H. Schoenbach, B. Hargrave, R. P. Joshi, J. F. Kolb, R. Nuccitelli, C. Osgood, *et al.*, "Bioelectric effects of intense nanosecond pulses," *IEEE Trans. Dielectr. Electr. Insula.*, vol. 14, pp. 1088-1107, 2007.
- [24] J. C. Neu and W. Krassowska, " Modeling postshock evolution of large electropores," *Phys. Rev. E Stat. Nonlin. Soft Matter Phys.*, vol. 67, p. 021915, 2003.
- [25] R. P. Joshi, Q. Hu, and K. H. Schoenbach, "Dynamical modeling of cellular response to short-duration, high-intensity electric fields," *IEEE Trans. Dielectrics and Electrical Insulation*, vol. 10, pp. 778- 787, 2003.
- [26] Q. Hu, R. P. Joshi, and K. H. Schoenbach, "Simulations of nanopore formation and phosphatidylserine externalization in lipid membranes subjected to a high-intensity, ultrashort electric pulse," *Phys. Rev. E Stat. Nonlin. Soft Matter Phys.*, vol. 72, p. 031902, Sep 2005.
- [27] Q. Hu, S. Viswanadham, R. P. Joshi, K. H. Schoenbach, S. J. Beebe, and P. F. Blackmore, "Simulations of transient membrane behavior in cells subjected to a high-intensity ultrashort electric pulse," *Phys. Rev. E Stat. Nonlin. Soft Matter Phys.*, vol. 71, p. 031914, Mar 2005.
- [28] D. P. Tieleman, H. Leontiadou, A. E. Mark, and S. J. Marrink, "Simulation of pore formation in lipid bilayers by mechanical stress and electric fields," *J. Am. Chem. Soc.*, vol. 125, pp. 6382-6383, 2003.
- [29] Y. E. Korchev, C. L. Bashford, G. M. Alder, P. Y. Apel, D. T. Edmonds, A. A. Lev, *et al.*, " A novel explanation for fluctuations of ion current through narrow pores," *Faseb J.* , vol. 11, p. 600, 1997.
- [30] L. Cheng and L. J. Guo, "Nanofluidic diodes," *Chemical Society Reviews*, vol. 39, pp. 923-938, 2010.

- [31] J. Cervera, B. Schiedt, R. Neumann, S. Mafé, and P. Ramírez, "Ionic conduction, rectification, and selectivity in single conical nanopores," *The Journal of Chemical Physics*, vol. 124, p. 104706, 2006.
- [32] D. Constantin and Z. S. Siwy, "Poisson-Nernst-Planck model of ion current rectification through a nanofluidic diode," *Physical Review E*, vol. 76, p. 041202, 10/15/2007.
- [33] M. Ali, P. Ramirez, S. Mafé, R. Neumann, and W. Ensinger, "A pH-Tunable Nanofluidic Diode with a Broad Range of Rectifying Properties," *ACS Nano*, vol. 3, pp. 603-608, 03/24/2009.
- [34] M. L. Kovarik, K. Zhou, and S. C. Jacobson, "Effect of Conical Nanopore Diameter on Ion Current Rectification," *The Journal of Physical Chemistry B*, vol. 113, pp. 15960-15966, 2009.
- [35] I. Vlassiouk, S. Smirnov, and Z. Siwy, "Nanofluidic Ionic Diodes. Comparison of Analytical and Numerical Solutions," *ACS Nano*, vol. 2, pp. 1589-1602, 08/01/2008.
- [36] A. G. Pakhomov, A. M. Bowman, B. L. Ibey, F. M. Andre, O. N. Pakhomova, and K. H. Schoenbach, "Lipid nanopores can form a stable, ion channel-like conduction pathway in cell membrane," *Biochemical & Biophysical Research Communications*, vol. 385, pp. 181-186, 2009.
- [37] A. G. Pakhomov, R. Shevin, J. A. White, J. F. Kolb, O. N. Pakhomova, R. P. Joshi, *et al.*, "Membrane permeabilization and cell damage by ultrashort electric field shocks," *Archives of Biochemistry and Biophysics*, vol. 465, pp. 109-118, 9/1/2007.
- [38] B. L. Ibey, S. Xiao, K. H. Schoenbach, M. R. Murphy, and A. G. Pakhomov, "Plasma membrane permeabilization by 60-and 600-ns electric pulses is determined by the absorbed dose," *Bioelectromagnetics*, vol. 30, pp. 92-99, 2009.
- [39] R. P. Joshi and Q. Hu, "Analysis of cell membrane permeabilization mechanics and pore shape due to ultrashort electrical pulsing," *Medical & Biological Engineering & Computing*, vol. 48, pp. 837-844, 2010.
- [40] L. V. Chernomordik, S. I. Sukharev, I. G. Abidor, and Y. A. Chizmadzhev, "Breakdown of lipid bilayer membranes in an electric field," *Biochimica et Biophysica Acta (BBA) - Biomembranes*, vol. 736, pp. 203-213, 1983.
- [41] J. Teissié and M. P. Rols, "An experimental evaluation of the critical potential difference inducing cell membrane electropermeabilization," *Biophysical Journal*, vol. 65, pp. 409-413, 1993.
- [42] T. Kotnik, P. Kramar, G. Pucihar, D. Miklavcic, and M. Tarek, "Cell membrane electroporation- Part I: The phenomenon," *IEEE Electrical Insulation Magazine*, vol. 28, pp. 14-23, 2012.
- [43] K. H. Schoenbach, S. J. Beebe, and E. S. Buescher, "Intracellular effect of ultrashort electrical pulses," *Bioelectromagnetics*, vol. 22, pp. 440-448, 2001.
- [44] E. Tekle, H. Oubrahim, S. M. Dzekunov, J. F. Kolb, K. H. Schoenbach, and P. Chock, "Selective field effects on intracellular vacuoles and vesicle membranes with nanosecond electric pulses," *Biophysical journal*, vol. 89, pp. 274-284, 2005.
- [45] T. B. Napotnik, Y. H. Wu, M. A. Gundersen, D. Miklavčič, and P. T. Vernier, "Nanosecond electric pulses cause mitochondrial membrane permeabilization in Jurkat cells," *Bioelectromagnetics*, vol. 33, pp. 257-264, 2012.

- [46] S. J. Beebe, J. White, P. F. Blackmore, Y. Deng, K. Somers, and K. H. Schoenbach, "Diverse effects of nanosecond pulsed electric fields on cells and tissues," *DNA and cell biology*, vol. 22, pp. 785-796, 2003.
- [47] S. S. Scarlett, J. A. White, P. F. Blackmore, K. H. Schoenbach, and J. F. Kolb, "Regulation of intracellular calcium concentration by nanosecond pulsed electric fields," *Biochimica et Biophysica Acta (BBA)-Biomembranes*, vol. 1788, pp. 1168-1175, 2009.
- [48] E. S. Buescher and K. H. Schoenbach, "Effects of submicrosecond, high intensity pulsed electric fields on living cells-intracellular electromanipulation," *IEEE Transactions on Dielectrics & Electrical Insulation*, vol. 10, p. 788, 2003.
- [49] E. S. Buescher, R. R. Smith, and K. H. Schoenbach, "Submicrosecond Intense Pulsed Electric Field Effects on Intracellular Free Calcium: Mechanisms and Effects," *IEEE Transactions on Plasma Science*, vol. 32, pp. 1563-1572, 2004.
- [50] K. H. Schoenbach, R. P. Joshi, S. J. Beebe, and C. E. Baum, "A Scaling Law for Membrane Permeabilization with Nanopulses," *IEEE Transactions on Dielectrics & Electrical Insulation*, vol. 16, pp. 1224-1235, 2009.
- [51] R. Nuccitelli, X. Chen, A. G. Pakhomov, W. H. Baldwin, S. Sheikh, J. L. Pomicter, *et al.*, "A new pulsed electric field therapy for melanoma disrupts the tumor's blood supply and causes complete remission without recurrence," *International Journal of Cancer*, vol. 125, pp. 438-445, 2009.
- [52] V. P. Skulatchev, "Membrane Bioenergetics," *Berlin: Springer-Verlag*, 1988.
- [53] M. J. Berridge, M. D. Bootman, and P. Lipp, "Calcium--a life and death signal," *Nature*, vol. 395, pp. 645-648, 1998.
- [54] S. A. Susin, N. Zamzami, and G. Kroemer, "Mitochondria as regulators of apoptosis: doubt no more," *Biochimica et Biophysica Acta (BBA)-Bioenergetics*, vol. 1366, pp. 151-165, 1998.
- [55] A. P. Halestrap and C. Brenner, "The adenine nucleotide translocase: a central component of the mitochondrial permeability transition pore and key player in cell death," *Current medicinal chemistry*, vol. 10, pp. 1507-1525, 2003.
- [56] A. P. Halestrap, G. P. McStay, and S. J. Clarke, "The permeability transition pore complex: another view," *Biochimie*, vol. 84, pp. 153-166, 2002.
- [57] M. Crompton, "The mitochondrial permeability transition pore and its role in cell death," *Biochem. J.*, vol. 341, pp. 233-249, 1999.
- [58] G. Kroemer and J. C. Reed, "Mitochondrial control of cell death," *Nature medicine*, vol. 6, 2000.
- [59] S. J. Beebe, P. M. Fox, L. J. Rec, E. L. K. Willis, and K. H. Schoenbach, "Nanosecond, high-intensity pulsed electric fields induce apoptosis in human cells," *FASEB Journal: Official Publication Of The Federation Of American Societies For Experimental Biology*, vol. 17, pp. 1493-1495, 2003.
- [60] J. C. Weaver, "Electroporation of Biological Membranes from Multicellular to Nano Scales," *IEEE Transactions on Dielectrics & Electrical Insulation*, vol. 10, p. 754, 2003.
- [61] R. P. Joshi, H. Qin, and K. H. Schoenbach, "Modeling studies of cell response to ultrashort, high-intensity electric fields-implications for intracellular manipulation," *IEEE Transactions on Plasma Science*, vol. 32, pp. 1677-1686, 2004.

- [62] J. C. Neu and W. Krassowska, "Asymptotic model of electroporation," *Physical Review E*, vol. 59, pp. 3471-3482, 1999.
- [63] K. DeBruin and W. Krassowska, "Electroporation and Shock-Induced Transmembrane Potential in a Cardiac Fiber During Defibrillation Strength Shocks," *Annals of Biomedical Engineering*, vol. 26, pp. 584-596, 1998.
- [64] <http://www.comsol.com>.
- [65] E. Neumann, "Electric field-induced structural rearrangements in biomembranes," *Electrochimica Acta*, vol. 34, pp. 1905-1907, 1989.
- [66] R. Joshi, J. Song, K. Schoenbach, and V. Sridhara, "Aspects of lipid membrane bio-responses to subnanosecond, ultrahigh voltage pulsing," *IEEE Transactions on Dielectrics and Electrical Insulation*, vol. 16, pp. 1243-1250, 2009.
- [67] S. J. Beebe, Y.-J. Chen, N. M. Sain, K. H. Schoenbach, and S. Xiao, "Transient features in nanosecond pulsed electric fields differentially modulate mitochondria and viability," *PloS one*, vol. 7, p. 51349, 2012.
- [68] J. Newman, K. E. and Thomas-Alyea, "Electrochemical Systems," *Hoboken, NJ: John Wiley & Sons*, 2004.
- [69] P. Y. Apel, I. V. Blonskaya, N. V. Levkovich, and O. L. Orelovich, "Asymmetric track membranes: Relationship between nanopore geometry and ionic conductivity," *Petroleum Chemistry* vol. 51, pp. 555-567, 2011.
- [70] Q. Hu, Z. Zhang, H. Qiu, M. Kong, and R. Joshi, "Physics of nanoporation and water entry driven by a high-intensity, ultrashort electrical pulse in the presence of membrane hydrophobic interactions," *Physical Review E*, vol. 87, p. 032704, 2013.
- [71] R. A. Böckmann, B. L. De Groot, S. Kakorin, E. Neumann, and H. Grubmüller, "Kinetics, statistics, and energetics of lipid membrane electroporation studied by molecular dynamics simulations," *Biophysical Journal*, vol. 95, pp. 1837-1850, 2008.

APPENDICES

APPENDIX I

WEAK FORMULATION

COMSOL Multiphysics uses the weak form as a particular way of specifying a model, which could solve strongly nonlinear and nonlocal models and use the test operator to conveniently work with problems in variational calculus. Usually, weak formulation is employed to build models with PDEs on boundaries, edges and points. Particularly, the Weak Form, Boundary application modes are of great use when to define a PDE on a boundary and couple the equation to an equation in a subdomain.

As discussed in Chapter III, equation (3.4) can be transformed as $\frac{dN}{dt} = AA - \frac{AA}{BB}N$, where $AA = \alpha e^{\left(\frac{TMP}{v_{ep}}\right)^2}$, $BB = N_0 e^{q\left(\frac{TMP}{v_{ep}}\right)^2}$.

The derivation is as:

$$\frac{dN}{dt} = AA - \frac{AA}{BB}N$$

Now suppose the boundary is denoted as: Ω , ds is the area element, and let v be an arbitrary function on Ω , which is called test function.

$$\Rightarrow \int_{\Omega} v \frac{dN}{dt} \cdot ds = \int_{\Omega} v AA \cdot ds - \int_{\Omega} v \frac{AA}{BB} N \cdot ds$$

$$\Rightarrow 0 = \int_{\Omega} v AA \cdot ds - \int_{\Omega} v \frac{AA}{BB} N \cdot ds - \int_{\Omega} v \frac{dN}{dt} \cdot ds$$

Thus, the weak form expression is: $(N) * (AA - \frac{AA}{BB} - N_t)$, where $N_t \equiv \frac{dN}{dt}$ in COMSOL.

APPENDIX II

DIMENSIONLESS FORM OF PNP-NS MODEL

Dimensionless form of equations is to make equations unitless and physical quantities are turned into merely representative numbers. There are several advantages: 1) to facilitate the scale-up of obtained results; 2) to avoid round-off due to manipulations with large or small numbers; 3) to assess the relative importance of terms in the model equations.

Back to Nernst-Planck equation (3.11) shown below:

$$N_i = uc_i - D_i \nabla c_i + z_i \frac{D_i}{RT} F c_i \nabla V \quad . \quad (3.11)$$

From this equation, dimensionless form should satisfy:

$$\left\{ \begin{array}{l} U_\infty = \frac{D_{i\infty}}{L_\infty} \quad , \\ U_\infty = D_{i\infty} \frac{F}{RT} \frac{V_\infty}{L_\infty} \quad . \end{array} \right.$$

and then, $V_\infty = \frac{RT}{F}$ can be obtained.

Similarly, from equation (3.13) below:

$$-\nabla P + \mu \nabla^2 u - \rho_e \nabla V = 0 \quad . \quad (3.13)$$

dimensionless form should satisfy:

$$\left\{ \begin{array}{l} P_\infty = \mu \frac{U_\infty}{L_\infty} \quad , \\ \mu \frac{U_\infty}{L_\infty^2} = \varepsilon \frac{V_\infty}{L_\infty^2} \frac{V_\infty}{L_\infty} \quad . \end{array} \right.$$

Then $U_\infty = \frac{\varepsilon}{\mu L_\infty} \cdot (V_\infty)^2$, $P_\infty = \mu \frac{U_\infty}{L_\infty}$ can be obtained.

The dimensionless form of Poisson equation (3.9) can be derived:

$$\Rightarrow -\varepsilon \frac{V_\infty}{L_\infty^2} \nabla^{*2} V^* = \rho_e \quad ,$$

$$\Rightarrow -\nabla^{*2} V^* = \rho_e^* = \frac{L_\infty^2 C_\infty}{\varepsilon V_\infty} F \sum_i^n z_i c_i^* \quad .$$

The dimensionless form of Nernst-Planck equation (3.11) can be derived:

$$\Rightarrow N_\infty N_i^* = U_\infty C_\infty u^* c_i^* - \frac{D_i C_\infty}{L_\infty} \nabla^* c_i^* - z_i \frac{D_i}{RT} F C_\infty C_i^* \frac{V_\infty}{L_\infty} \nabla^* V^* \quad ,$$

$$\Rightarrow \left\{ \begin{array}{l} N_\infty = U_\infty C_\infty \quad , \\ N_i^* = u^* c_i^* - \frac{D_i C_\infty}{L_\infty N_\infty} \nabla^* c_i^* - z_i \frac{D_i}{RT} F C_i^* \nabla^* V^* \frac{C_\infty V_\infty}{L_\infty N_\infty} \quad , \end{array} \right.$$

$$\Rightarrow \left\{ \begin{array}{l} D_i^* = D_i \frac{C_\infty}{L_\infty N_\infty} = D_i \frac{1}{L_\infty U_\infty} \quad , \\ N_i^* = u^* c_i^* - D_i^* \nabla^* c_i^* - z_i D_i^* C_i^* \nabla^* V^* \quad . \end{array} \right.$$

The dimensionless form of Navier Stokes equation (3.13) can be derived:

$$\Rightarrow -\frac{P_\infty}{L_\infty} \nabla^* P^* + \mu \frac{U_\infty}{L_\infty^2} \nabla^{*2} u^* - \rho_e \nabla^* V^* \frac{V_\infty}{L_\infty} = 0 \quad ,$$

$$\Rightarrow -\nabla^* P^* + \nabla^{*2} u^* - F C_\infty \sum_i^n z_i c_i^* \frac{V_\infty}{P_\infty} \nabla^* V^* = 0 \quad .$$

APPENDIX III

PNP MODEL ANALYTICAL SOLUTION

The electric potential from PNP model is analytically calculated in the case of two ions and one-dimension problem due to symmetry.

Poisson equation is written as:

$$-\varepsilon \frac{d^2V}{dx^2} = F(z_1c_1 + z_2c_2) \quad ,$$

where V is the electric potential, x is the distance to the stern layer, z_i and c_i is valence and concentration of ion, respectively.

Nernst-Planck equation is shown below as:

$$\begin{cases} \frac{\partial c_i}{\partial t} + \nabla \cdot N_i = 0 \quad , \\ N_i = uc_i - D_i \nabla c_i - z_i \frac{D_i}{RT_i} F c_i \nabla V \quad . \end{cases}$$

where $u = 0$ is fluid motion velocity, $\frac{\partial c_i}{\partial t} = 0$.

Consider 1-D problem:

$$\Rightarrow \frac{dN_i}{dx} = 0 \quad ,$$

$$\text{and } x \rightarrow \infty \Rightarrow \begin{cases} c_i \rightarrow c_{i0} \text{ (bulk concentration)} \quad , \\ \frac{dV}{dx} = 0 \quad , \end{cases}$$

$$\Rightarrow -D_i \frac{dc_i}{dx} - z_i \frac{D_i}{RT_i} F c_i \frac{dV}{dx} = N_i$$

then integrating from initial to ∞ :

$$\Rightarrow \ln c_i + \frac{z_i F}{RT} V = \text{constant}$$

$$\Rightarrow \ln \frac{c_i}{c_{i0}} = -\frac{z_i F}{RT} V$$

$$\Rightarrow c_i = c_{i0} \exp\left(-\frac{z_i F}{RT} V\right)$$

The dimensionless form of Poisson equation is:

$$-\varepsilon \frac{RT}{FL_D^2} \frac{d^2 V^*}{dx^{*2}} = F \sum_{i=1}^2 z_i c_{i0} e^{-z_i V^*}$$

where $L_D = \sqrt{\frac{RT\varepsilon}{\sum_{i=1}^2 F^2 z_i c_{i0}}}$ is Debye length, $V^* = \frac{F}{RT} V$, $x^* = \frac{x}{L_D}$.

Take $z_1 = -z_2 = 1$:

$$\Rightarrow -\frac{d^2 V^*}{dx^{*2}} = \frac{e^{-V^*} - e^{V^*}}{2} ,$$

$$\text{and } \begin{cases} x^* = 0 \Rightarrow V^* = V_s^* \text{ (zeta potential)} \\ x^* \rightarrow \infty \Rightarrow V^* = 0 \end{cases} ,$$

I. When $|V^*| \ll 1$, using $e^x \approx 1 + x$:

$$\Rightarrow -\frac{d^2 V^*}{dx^{*2}} = V^* ,$$

$$\Rightarrow V^* = V_s^* e^{-x^*} \text{ (Debye - Huckel Approximation)}$$

II. When $|V^*| \gg 1$:

$$\Rightarrow -\frac{d}{dx^*} \left[\frac{d^2 V^*}{dx^{*2}} \right] = \frac{d}{dx^*} (e^{-V^*} + e^{V^*})$$

$$\Rightarrow \left(\frac{dV^*}{dx^*} \right)^2 = 2(\cosh V^* - 1)$$

$$\Rightarrow \frac{dV^*}{dx^*} = \sqrt{2(\cosh V^* - 1)} = \sqrt{(2\sinh(\frac{V^*}{2}))^2} = -2\sinh(\frac{V^*}{2})$$

$$\Rightarrow \int_{V_s^*}^{V^*} \frac{dV^*}{2\sinh(\frac{V^*}{2})} = \int_0^{x^*} -dx^* = -x^*$$

$$\Rightarrow \ln \tanh\left(\frac{V^*}{4}\right) \Big|_{V_s^*}^{V^*} = -x^*$$

$$\Rightarrow \tanh\left(\frac{V^*}{4}\right) = \tanh\left(\frac{V_s^*}{4}\right) e^{-x^*}$$

$$\Rightarrow V^* = 4 \operatorname{atanh} \left[\tanh\left(\frac{V_s^*}{4}\right) \exp(-x^*) \right]$$

The dimensional form is:

$$\Rightarrow V =$$


$$\frac{4RT}{F} \operatorname{atanh} \left[\tanh\left(\frac{FV_s}{4RT}\right) \exp\left(-\frac{x}{L_D}\right) \right] \quad (\text{Gouy - Chapman Solution})$$

APPENDIX IV

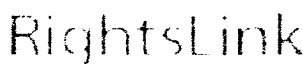
REUSE LICENSES

Figure 28: Reuse License for Figure 1


7/20/14 RightsLink by Copyright Clearance Center



Copyright
Clearance
Center



Home
Account
Info
Help



IEEE
Requesting
permission
to reuse
content from
an IEEE
publication

Title: Cell membrane electroporation-
Part 1: The phenomenon

Author: Kotnik, T.; Kramar, P.; Pucihar,
G.; Miklavcic, D.; Tarek, M.

Publication: IEEE Electrical Insulation
Magazine

Publisher: IEEE

Date: September-October 2012
Copyright © 2012, IEEE

Logged in as:
Hao Qiu

Account #:
3000813132

Logout

Thesis / Dissertation Reuse

The IEEE does not require individuals working on a thesis to obtain a formal reuse license, however, you may print out this statement to be used as a permission grant:

Requirements to be followed when using any portion (e.g., figure, graph, table, or textual material) of an IEEE copyrighted paper in a thesis:

- 1) In the case of textual material (e.g., using short quotes or referring to the work within these papers) users must give full credit to the original source (author, paper, publication) followed by the IEEE copyright line © 2011 IEEE.
- 2) In the case of illustrations or tabular material, we require that the copyright line ©: [Year of original publication] IEEE appear prominently with each reprinted figure and/or table.
- 3) If a substantial portion of the original paper is to be used, and if you are not the senior author, also obtain the senior author's approval.

Requirements to be followed when using an entire IEEE copyrighted paper in a thesis:

- 1) The following IEEE copyright/ credit notice should be placed prominently in the references: ©: [year of original publication] IEEE. Reprinted, with permission, from [author names, paper title, IEEE publication title, and month/year of publication]
- 2) Only the accepted version of an IEEE copyrighted paper can be used when posting the paper or your thesis on-line.
- 3) In placing the thesis on the author's university website, please display the following message in a prominent place on the website: In reference to IEEE copyrighted material which is used with permission in this thesis, the IEEE does not endorse any of [university/educational entity's name goes here]'s products or services. Internal or personal use of this material is permitted. If interested in reprinting/republishing IEEE copyrighted material for advertising or promotional purposes or for creating new collective works for resale or redistribution, please go to http://www.ieee.org/publications_standards/publications/rights/rights_link.htm to learn how to obtain a License from RightsLink.

If applicable, University Microfilms and/or ProQuest Library, or the Archives of Canada may supply single copies of the dissertation.

BACK
CLOSE WINDOW

Copyright © 2014 Copyright Clearance Center, Inc. All Rights Reserved. [Privacy statement](#).
Comments? We would like to hear from you. E-mail us at customerservice@copyright.com.

Figure 29: Reuse License for Figure 3

Hao Qiu <qiuha0809@gmail.com>
To: Permissions <permissions@iop.org>

Thu, Jul 24, 2014 at 8:09 AM

Hello Laura Sharples

Thanks!

The cited paper in my dissertation is : *S. J. Beebe, P. F. Blackmore, J. White, R. P. Joshi, and K. H. Schoenbach, "Nanosecond pulsed electric fields modulate cell function through intracellular signal transduction mechanisms." *Physiol. Meas.*, vol. 25, p. 1077, 2004.

doi:10.1088/0967-3334/25/4/023

I used one figure in my dissertation.. The figure number is Figure.8.

Re: Fw: Reuse License for Disseration

Permissions <permissions@iop.org>
To: Hao Qiu <qiuha0809@gmail.com>

Thu, Jul 24, 2014 at 8:42 AM

Dear Hao,

Thank you for your swift response.

We are happy to grant permission for the use you request on the terms set out below.

If you have any questions, please feel free to contact our Permissions team at permissions@iop.org.

I should be grateful if you would acknowledge receipt of this email.

Kind regards,

Laura
Laura Sharples
Rights & Permissions Officer
IOP Publishing Ltd
Temple Circus, Temple Way, Bristol BS1 0HG

T: +44 (0)117 930 1001

F: +44 (0)117 920 0967

[What do scientific publishers do?](#)

Conditions

Non-exclusive, non-transferrable, revocable, worldwide, permission to use the material in print and electronic form will be granted subject to the following conditions:

- Permission will be cancelled without notice if you fail to fulfil any of the conditions of this letter.
- You will make reasonable efforts to contact the author(s) to seek consent for your intended use. Contacting one author acting expressly as authorised agent for their co-authors is acceptable.
- You will reproduce the following prominently alongside the material:
 - o the source of the material, including author, article title, title of journal, volume number, issue number (if relevant), page range (or first page if this is the only information available) and date of first publication. This information can be contained in a footnote or reference note; or
 - o a link back to the article (via DOI); and
 - o if practical and IN ALL CASES for works published under any of the Creative Commons licences the words "© IOP Publishing. Reproduced with permission. All rights reserved"
- The material will not, without the express permission of the author(s), be used in any way which, in the opinion of IOP Publishing, could distort or alter the author(s)' original intention(s) and meaning, be prejudicial to the honour or reputation of the author(s) and/or imply endorsement by the author(s) and/or IOP Publishing.

<https://mail.google.com/mail/u/0/?ui=2&ui=657e8f974&view=pt&search=Inbox&msg=1475864f3926dbef&siml=1475864f3926dbef>

1/2

7/24/14

Gmail - Re: Fw: Reuse License for Disseration

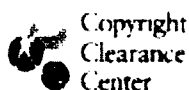
- Payment of £0 is received in full by IOP Publishing prior to use.

Please note: We do not usually provide signed permission forms as a separate attachment. Please print this email and provide it to your publisher as proof of permission.

Figure 30: Reuse License for Figure 4

7/21/14

RightsLink® by Copyright Clearance Center



RightsLink

Home

Account
Info

Help



Title: Modeling studies of cell response to ultrashort, high-intensity electric fields-implications for intracellular manipulation

Author: Joshi, R.P.; Qin Hu; Schoenbach, K.H.

Publication: Plasma Science, IEEE Transactions on

Publisher: IEEE

Date: Aug. 2004

Copyright © 2004, IEEE

Logged in as:
Hao Qiu
Account #:
3000813132

Logout

Thesis / Dissertation Reuse

The IEEE does not require individuals working on a thesis to obtain a formal reuse license, however, you may print out this statement to be used as a permission grant:

Requirements to be followed when using any portion (e.g., figure, graph, table, or textual material) of an IEEE copyrighted paper in a thesis:

- 1) In the case of textual material (e.g., using short quotes or referring to the work within these papers) users must give full credit to the original source (author, paper, publication) followed by the IEEE copyright line © 2011 IEEE.
- 2) In the case of illustrations or tabular material, we require that the copyright line © [Year of original publication] IEEE appear prominently with each reprinted figure and/or table.
- 3) If a substantial portion of the original paper is to be used, and if you are not the senior author, also obtain the senior author's approval.

Requirements to be followed when using an entire IEEE copyrighted paper in a thesis:

- 1) The following IEEE copyright/ credit notice should be placed prominently in the references: © [year of original publication] IEEE. Reprinted, with permission, from [author names, paper title, IEEE publication title, and month/year of publication]
- 2) Only the accepted version of an IEEE copyrighted paper can be used when posting the paper or your thesis on-line.
- 3) In placing the thesis on the author's university website, please display the following message in a prominent place on the website: In reference to IEEE copyrighted material which is used with permission in this thesis, the IEEE does not endorse any of [university/educational entity's name goes here]'s products or services. Internal or personal use of this material is permitted. If interested in reprinting/republishing IEEE copyrighted material for advertising or promotional purposes or for creating new collective works for resale or redistribution, please go to http://www.ieee.org/publications_standards/publications/rights/rights_link.html to learn how to obtain a License from RightsLink.

If applicable, University Microfilms and/or ProQuest Library, or the Archives of Canada may supply single copies of the dissertation.

BACK

CLOSE WINDOW

VITA

for

Hao Qiu

EDUCATION

PhD. Electrical and Computer Engineering, Old Dominion University, Norfolk, VA

B.S. Electronics Engineering, Northwest University, China

PAPERS PUBLISHED

R. P. Joshi, **H. Qiu**, and R. K. Tripathi, "Evaluation of a combined electrostatic and magnetostatic configuration for active space-radiation shielding," **Advances in Space Research**, vol. 51, pp. 1784-1791, 5/1/2013.

R. P. Joshi, **H. Qiu**, and R. K. Tripathi, "Configuration studies for active electrostatic space radiation shielding," **Acta Astronautica**, vol. 88, pp. 138-145, 7/2013.

Q. Hu, Z. Zhang, **H. Qiu**, M. G. Kong, and R. P. Joshi, "Physics of nanoporation and water entry driven by a high-intensity, ultrashort electrical pulse in the presence of membrane hydrophobic interactions," **Physical Review E**, vol. 87, p. 032704, 03/07/2013

H. Qiu, S. Xiao, R.P. Joshi, "Simulations of Voltage Transients Across Intracellular Mitochondrial Membranes Due to Nanosecond Electrical Pulsing", **IEEE Trans. Plasma Science**. [Accepted]

Hao Qiu, S. Prasad, L. Ludeking, R.P.Joshi, and E.Schamiloglu, "Assessing the Role of Secondary Electron Emission on the Characteristics of 6-Cavity Magnetrons With Transparent Cathode Through Particle-in-Cell Simulations", **Journal of Applied Physics**, vol. 115, issue 19, p. 193303, 5/2014.

CONFERENCE PRESENTATION

"Evaluation of Secondary Electron Emission effects in the A6 Magnetron with transparent cathodes using MAGIC", ICOPS/BEAMS 2014 (The 41st IEEE International Conference on Plasma Science and the 20th International Conference on High-Power Particle Beams), May25-29, 2014, Washington DC.

AWARD

Outstanding PhD Researcher, Department of Electrical and Computer Engineering, ODU (2013-2014)